Emission Spectroscopy for the Study of Electric Propulsion Plasmas

by

Taylor Scott Matlock

Submitted to the Department of Aeronautics and Astronautics
in partial fulfillment of the requirements for the degree of

Master of Science in Aeronautics and Astronautics

at the

MASSACHUSETTS INSTITUTE OF TECHNOLOGY

June 2009

Author .....
Department of Aeronautics and Astronautics
May 22, 2009

Certified by .....
Oleg Batishchev
Principal Research Scientist
Thesis Supervisor

Accepted by .....
Prof. David L. Darmofal
Associate Depatrment Head
Chair, Department Committee on Graduate Theses

Emission Spectroscopy for the Study of Electric Propulsion Plasmas

by

Taylor Scott Matlock

Submitted to the Department of Aeronautics and Astronautics
on May 22, 2009, in partial fulfillment of the
requirements for the degree of
Master of Science in Aeronautics and Astronautics

Abstract

Typical electric propulsion devices rely on the acceleration of highly ionized plasmas to produce thrust at specific impulses unattainable with state-of-the-art chemical systems. This thesis examines the use of a miniaturized Helicon plasma source for an open-ended, electrode-less, cathode-less thruster through emission spectroscopy. The use of non-invasive diagnostics allows the measurement of important plasma parameters near the ionization region, where the plasma densities and temperatures are prohibitively high for typical electrostatic probes, while avoiding the inherent perturbations caused by invasive techniques. A spectral study of the Helicon antenna region, yielding axially resolved information on the electron temperature and degree of ionization, is discussed. A similar study in the near-field plume is presented, along with Doppler shift measurements, which clearly demonstrate continued acceleration upstream of the thruster exit. The Doppler shift measurements are validated by extending the study to a Hall effect thruster plasma, well characterized in the literature. Ion flux estimates from the downstream portion of the spectroscopic survey are compared with Faraday probe measurements. Possible mechanisms for thrust are presented along with their implications on Helicon thruster design.

Thesis Supervisor: Oleg Batishchev
Title: Principal Research Scientist

Acknowledgments

I'd like to thank my research advisor, Oleg Batishchev, for all his help in the lab and invaluable daily discussions. I'm grateful to Dan Courtney for keeping the Space Propulsion Lab running, and for all his help along the way. I'm also indebted to Nareg Sinenian for teaching me the quirks of running our thruster and to Murat Celik for teaching me the even more frustrating procedures for running our spectroscopic system. I'd also like to thank Steve Gildea, Greg O'Neill and B.J. White for lending a hand in and out of the lab whenever I needed. Most of all, I'd like to thank my family and of course Andrea for their constant support.

Contents

List of Figures

List of Tables

Chapter 1

Introduction

Electric propulsion devices can offer significant mass savings over chemical rockets, in the form of less on-board propellant, when short duration impulses are not required. Increasing the ionization efficiency of a typical plasma propelled rocket is essential to improving performance, as thrust is almost exclusively produced by ion acceleration. To this end, Helicon plasma sources are currently under investigation for application to in-space propulsion.

The goal of the investigations herewithin are to characterize a miniaturized, open-ended Helicon plasma source as a thruster concept, using minimally obtrusive techniques. The remainder of this chapter will review the relevant physical processes of electric thruster operation, Helicon plasma sources, and associated diagnostics. The results of the investigation are contained in the chapters to follow.

1.1 Role of Electric Propulsion

The main drawback of chemical propulsion is the inherent limit of propellant energy to the amount released by reaction. Electric propulsion systems may deliver substantially more energy, but require the inclusion of a separate power supply and its incumbent mass. Electric systems are also typically far less constrained by materials due to substantially lower power losses to thruster surfaces.

While electrically powered systems can achieve one to two orders of magnitude

higher exhaust velocities than their chemical counterparts, they typically operate at many more orders of magnitude lower propellant mass flow rates. The sub-Newton thrusts typically provided relegate electric propulsion systems to in-space use, where the work against gravity is negligible. The thrust afforded by an electrical propulsion device, F, can then be examined by Equation 1.1 where there is a negligible pressure thrust from the propellant at exit. Here u_e is the velocity of exhausted propellant relative to the spacecraft, which has an instantaneous mass m and velocity u and is losing mass (in the form of propellant) at a rate $\dot{m}$.

$$F = m\frac{d(u)}{dt} = \dot{m}u_e \tag{1.1}$$

Propulsive requirements for an orbit altering maneuver are typically given in terms of the total change in velocity required, Δu. Putting Equation 1.1 in terms of Δu is simple and results in Equations 1.2 and 1.3.

$$\Delta u = u_e ln\frac{m_i}{m_f} \tag{1.2}$$

$$m_{prop} = m_0[1 - e^{-\Delta u/u_e}] \tag{1.3}$$

It is clear from Equation 1.3 that higher exhaust velocities result in lower propellant mass, m_{prop}, requirements to achieve a given velocity incrementation. The high mass savings possible with high exhaust velocities are what motivates the use of electric propulsion systems.

More generally the u_e term in the equations is replaced by gI_{sp}, where g is the standard acceleration due to gravity at sea-level and gI_{sp} is the ratio of thrust to propellant usage rate. The specific impulse, I_{sp}, is an oft quoted measure of the efficiency of propellant usage, which is simply the mass weighted average exhaust velocity over a constant.

For many electric propulsion concepts thrust is obtained by the acceleration of a stream of ions out of the device. The ions must be neutralized some time after

exiting the device in order to prevent them from returning to the spacecraft and negating their initial thrust. Several efficiencies can be defined which describe the effective conversion of input power or propellant input to creating and accelerating ions towards a collimated exhaust beam.

Gas utilization efficiency is a measure of the degree to which the incoming neutral gas flow is converted to ions. The flux of particles through a given area is given by,

$$\Gamma = nv \tag{1.4}$$

where n and v are the number density and velocity of the species of interest respectively.

The relation between mass flow rate and particle flux is given by,

$$\dot{m} = \rho v A = m \Gamma A \tag{1.5}$$

where ρ is the mass density and A is the cross-sectional area through which the mass is flowing. A relationship between ion current through a given area and ion flux is prescribed by,

$$I_i = q \Gamma_i A \tag{1.6}$$

where q is the effective charge on the species. The effective charge is often taken as the charge of a single electron during analysis of electrostatic probe data, but it should be noted that most plasmas contain a significant portion of both doubly and triply charged ions as well. The effect of assuming an entirely singly charged population is an overestimation of the ion flux for a measured ion current.

Equation 1.7, which defines the gas utilization efficiency, η_u, is shown in terms of measurable quantities.

$$\eta_u = \frac{\dot{m}_i}{\dot{m}} = \frac{m_i I_i}{q \dot{m}} \tag{1.7}$$

In this equation, $\dot{m}$ is the mass flow rate of the input neutral gas while $\dot{m}_i$ is the mass flow rate of ions at the location being measured.

The ion cost, α_c, is defined by,

$$\alpha_c = \frac{P_{in}}{e\Gamma_i A} = \frac{P_{in}}{I_i} \tag{1.8}$$

where P_{in} is the input power and e is the charge of an electron, which is used to put the measurement in terms of electron volts per created ion. The average energy used to create an ion is always more than the ionization potential, χ_i, due to the collisional dynamics and inefficiencies in power conversion.

1.2 Helicon Thruster Concepts

The Helicon has emerged in the past twenty years as an intriguing plasma source, using radio-frequency driven coaxial antennas around a gas confinement tube to nearly completely ionize the contained gas when an axial magnetic field is applied.

Several thruster concepts make use of the high efficiencies of Helicons as a plasma source. Typical use of Helicons is as the ionization and sometimes plasma heating stage, with subsequent stages used to accelerate the produced ions in an exhaust beam.

The simplest incarnations, such as the one studied here, rely on electron heating by the antenna being transferred to ion momentum by an ambipolar field [55, 44, 51]. Further conversion of plasma thermal energy to the desired axial ion kinetic energy has been achieved using simple magnetic nozzles [54, 18].

The double layer thruster concept of Charles and Boswell involves a thin layer of non-neutrality, created by suprathermal electrons, which accelerates an ion beam to around 3 times the bulk electron temperature [14, 52]. Though the double layer has been measured experimentally, analysis by Ahedo shows no propulsion gain resulting from the current-free double layer over the analogous thermodynamic system where no double layer is formed [1] which is expected simply by conservation of energy.

Several of the more complex concepts use the Helicon solely as a plasma source. The VASIMR engine creates a dense Helicon plasma which is subsequently heated by

an ion cyclotron resonant heating stage and accelerated through a magnetic nozzle [13, 3]. Another concept utilizes an annular Helicon plasma source as the ionization stage of a Hall Effect thruster, and thus allowing higher thrust-to-power to be obtained without a decrease in thrust efficiency [43].

Helicons have also found wide use in the field of plasma processing and space plasma physics experiments [35, 50, 33, 23, 19]. The majority of the Helicon experiments mentioned involve Pyrex gas confinement tubes at least 60 cm long with diameters ranging from 5-20 cm the exit of which inlets into a larger vacuum chamber with typical pressures on the order of 50 mPa.

The miniature Helicon Experiment at MIT, by contrast, has a confinement tube inner diameter of 18 mm at most and is less than 20 cm long. An electromagnet is only used on the exit side of the antenna and the entire device is immersed in a large vacuum chamber which maintains pressures below 7 mPa. Miniaturization is predicted to improve performance by both the inverse relation between plasma density and tube radius in the dispersion relation derived in the following section and the existence of a gas burn-out regime found in Helicons that lead to a jump in electron temperature. This gas burn-out effect has been predicted experimentally and later supported by experimental evidence [5, 6, 7, 8, 9].

Unlike Ion Engines and Hall Thrusters the Helicon does not require a cathode for plasma neutralization or an anode submerged in the plasma. Radial ion confinement by the magnetic field is used to limit wall losses and as yet no significant erosion of the gas confinement tube has been measured.

The lack of the lifetime limiting components found in similar plasma thrusters suggests the viability of Helicon thruster concepts for interplanetary missions where high I_{sp} is essential, and thus long burn times necessary. The ability to achieve both high exhaust velocities and long life times are predicted for Helicon-based thermal rockets.

1.2.1 Helicon Dispersion Relation

The dispersion relation for a Helicon plasma can be derived in the normal way using Maxwell's Equations and conservation of linear momentum. The momentum equation for species j follows as

$$m_j n_j \frac{d\vec{v_j}}{dt} = q_j n_j (\vec{E} + \vec{v_j} \times \vec{B}) - m_j n_j (\vec{v_j} - \vec{v_k}) \nu_{jk} - \nabla P_j \tag{1.9}$$

where ν_{jk} is the collision frequency of species j in species k. The typical configuration of a Helicon source consists of a non-conducting gas confinement tube in line with an axial applied magnetic field. This configuration suggests the use of cylindrical coordinates when applying perturbation techniques, in the form

$$\vec{Q}(\vec{r}, t) = \vec{Q_0} + \vec{Q_1}(\vec{r}, t) \tag{1.10}$$

$$\vec{Q_1} = \hat{Q}_1 e^{i(m\theta + kz - \omega t)} \tag{1.11}$$

where Q_0 is the equilibrium state, m is the azimuthal mode, ω is the perturbation frequency and k is the axial wavenumber.

Applying the above perturbation techniques to the momentum equation, Maxwell's equations and defining the perturbation current as $\mathbf{j} = -en_e\mathbf{v_e}$ leads to the dispersion relation [47],

$$\beta_{H,TG} = (\frac{k\omega_{ce}}{2\gamma\omega}) \left[1 \mp \sqrt{1 - 4\gamma(\frac{\omega_{pe}\omega}{\omega_{ce}kc})^2}\right] \tag{1.12}$$

where β is the total wavenumber, $\gamma = 1 + i\frac{\nu_{eH}}{\omega}$ accounts for electron collisions with heavy particles, $\omega_{pe}^2 = \frac{n_e e^2}{m_e \epsilon_0}$ is the electron plasma frequency and $\omega_{ce} = \frac{eB_0}{m_e}$ is the electron gyrofrequency. The minus and positive signs correspond to the Helicon (H) wave and an electrostatic electron cyclotron mode called the Trivelpiece-Gould (TG) wave respectively.

The complete derivation can be found in a multitude of sources [15, 16, 48, 45].

Initial work neglected electron inertia, which leads only to the H wave, but it has since been suggested that the TG mode plays a prominent role in the anomalously high ionization rates found in Helicon plasmas and is essential to closing the problem at a non-conducting boundary [16, 47].

Considering only H mode propagation with negligible electron-ion collisions, application of an insulation boundary condition ($j_r(a) = 0$) at the tube radius, a, leads to the expression,

$$\frac{\omega}{k} = \frac{3.83 B_0}{e \mu_0 n_0 a} \tag{1.13}$$

for the m=0 mode, where the 3.83 is the first zero of the J_1 Bessel function. A factor of $\omega a/3.83^2$ is added to the left hand side of Equation 1.13 for the m=1 mode [15]. The relation shows the linear increase of density, n_0, with applied field, B_0, when the RF power is sufficient for ionization.

1.2.2 Ambipolar Field in the Expanding Plasma Plume

As mentioned above, the Helicon plasma source can provide thrust with no external mechanisms due to the strong electric field created by large electron pressure gradients. The effect of the electron pressure can be seen in the electron momentum equation below, where electron inertia is negligible.

$$\nabla P_e = -e n_e E_z - m_e n_e \nu_{ei}(v_e - v_i) - m_e n_e \nu_{en}(v_e - v_n) \tag{1.14}$$

Looking only at the axial velocities of ions flowing along the thruster axis, the magnetic field terms disappear and the ion momentum balance is shown by Equation 1.15 where the ion pressure is neglected assuming $T_i << T_e$.

$$m_i n_e v_i \nabla v_i = e n_e E_z - m_e n_e \nu_{ei}(v_i - v_e) - \frac{m_i}{2} n_e (\nu_{in} + 2\nu_{CEX})(v_i - v_n) \tag{1.15}$$

Adding Equation 1.14 to the ion momentum equation, where the electron-neutral

collisions can be discarded with little effect, adding the definition of the ion-neutral collision frequency, $\nu_{in} = (0.5\sigma_{in} + \sigma_{CEX})n_n(v_i - v_n)$, and assuming $\frac{\nabla T_e}{T_e} << \frac{\nabla n_e}{n_e}$ we obtain,

$$m_i v_i \partial v_i = kT_e \frac{\partial n_e}{n_e} - m_i n_n \sigma_{in} v_i (z)^2 \partial l \tag{1.16}$$

where l is the vector along which the gradient is taken.

Integrating Equation 1.16 yields,

$$v^2 - v_0^2 = 2c_{s_i}^2 ln\frac{n}{n_0} - 2\int_0^z n_n \sigma_{in} v(z)^2 dl \tag{1.17}$$

where the subscripts i and e are dropped for simplicity, the subscript 0 indicates quantities at the exit of the thruster and c_{s_i} is the ion acoustic speed given by Equation 1.18.

$$c_{s_i} = \sqrt{\frac{kT_e}{m_i}} \tag{1.18}$$

The expansion of the plasma plume as it exits the thruster can be accounted for in a simple manner by considering the ion flux to remain within a cone of some divergence angle, θ_{div}, as shown in Figure 1-1. The continuity equation shown for ions in Equation 1.19 can be expressed in terms of the Figure 1-1 geometry by Equation 1.20, where the ion source/sink term, S_i, is neglected in near plume, a is the tube radius and $z_0(\theta_{div}, a)$ is the distance from the origin of the expanding cone to the exit plane.

$$\frac{\partial n_i}{\partial t} + \nabla \cdot (n_i \vec{v_i}) = S_i \tag{1.19}$$

$$nv(z_0 + z)^2 = n_0 v_0 z_0^2 \tag{1.20}$$

Equations 1.17 and 1.20 can be simplified by introducing dimensionless variables, $\widetilde{n} = n/n_0$, $\widetilde{z} = z/z_0$, $\widetilde{v} = v/c_{s_i}$ and $\widetilde{v_0} = \gamma$. The neutral density can be non-dimensionalized by noting that the collision cross section is roughly constant ($\nabla T_e \sim 0$) at around 0.5x10^{-18} m^2 so that $2\sigma_{in} n_n \simeq N$ (m^{-1}), where N is neutral density in 10^{18}

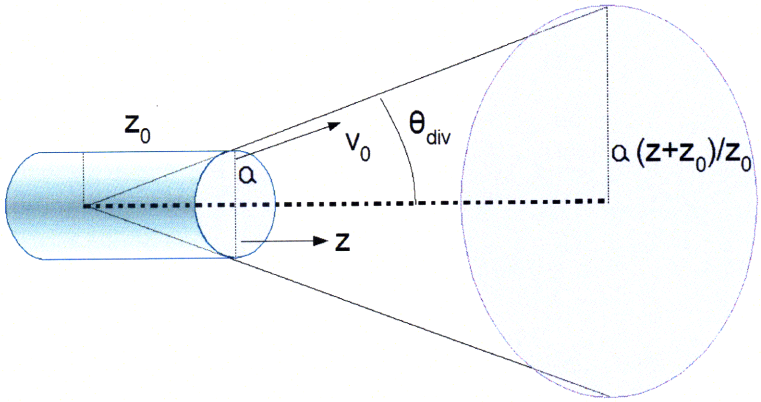

Figure 1-1: Diagram of the simple 2D geometry considered in the expansion model, a is the tube radius, $z_0 = a/tan\theta_{div}$ is distance from exit to origin

m^{-3}. The resulting relations are given as Equations 1.21 and 1.22, where $N^* = Nz_0$.

$$\tilde{n}\tilde{v}(1+\tilde{z})^2 = \gamma \tag{1.21}$$

$$\tilde{v}^2 = \gamma^2 - 2ln(\tilde{n}) - \int_0^{\tilde{z}} N^*\tilde{v}^2 dl \tag{1.22}$$

The logarithm in Equation 1.22 is never greater than zero, in the absence of neutrals, and represents the acceleration due to expansion. The integral term represents deceleration due mainly to charge transfer collisions.

The neutral density profile is unknown, but can be solved for the limiting case of no acceleration, i.e. $\tilde{v}(z) \equiv \gamma$. Taking the derivative of Equation 1.22 and using the plasma density from Equation 1.21 gives a neutral density threshold of,

$$N^*_{max} = \frac{4}{\gamma^2(1+\tilde{z})} \tag{1.23}$$

above which no acceleration occurs in the plume. For a 15^o divergence, z_0=34 mm, and sonic exit velocity the neutral density at the exit must be below 1.2x10^{20} m^{-3}. At the maximum flow rate used here the chamber pressure equilibrates at 6.7

mPa, corresponding to a neutral density of 1.6x10^{18} m^{-3} using the perfect gas law ($P = nkT$). At this background density the plume continues to accelerate up to 2.5 m from the exit, but over this distance the temperature gradient is no longer negligible and the simple analysis breaks down.

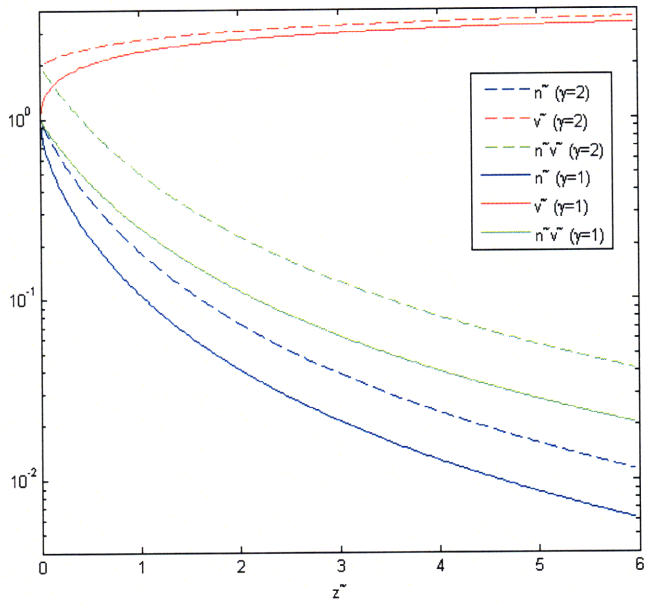

Figure 1-2: 2-D Expansion Model Neglecting Collisions with $\theta_{div} = 15^o$

Neglecting collisions allows for the solution of the velocity and density profiles with any numerical root finding method. The results for two values of γ and $\theta_{div} = 15^o$ (z_0=34mm) are shown in Figure 1-2. The shape of the resulting normalized curves is not dependent on θ_{div}. The divergence angle is only important when mapping the results to physical z values through z_0.

1.3 Plasma Diagnostics

The most widely used methods to measure the conditions within a plasma utilize bare electrodes biased relative to the plasma with simplified models to analyze the resulting current collection. Such probes are typically classified as electrostatic due to their use of simple DC biasing and are described in more detailed in section 1.3.2.

The extreme temperatures and relatively large densities achieved in the plasma sources under consideration make the use of invasive diagnostics difficult. Perturbations due to the high RF voltages created by the antenna of the Helicon further complicate the use of submerged electrodes. In light of the difficulties posed by insertion of probes into Helicon plasmas the use of non-invasive techniques is highly attractive.

There are varying degrees of complexity and invasiveness in the different electrodeless techniques used to characterize laboratory plasmas. Laser-induced fluorescence techniques perturb the plasma to some degree and the systems are complex and costly, but they allow accurate measurements of ion velocities with good spatial resolution [29, 51, 20, 12, 18].

Microwave interferometry uses the phase shift, caused by the intervening plasma, of two or more coherent waves to measure the refractive index and thus the density of a plasma. The measurements are essentially along an entire chord and therefore prior information about the density profile along that chord is necessary if any spatial resolution is to be obtained. Interferometric techniques have found wide use in Helicon plasmas, providing reliable density measurements in regions where Langmuir probe use is problematic [19, 34].

Optical emission spectroscopy models have been used to evaluate spatial trends in density and sometimes electron temperature by a number of sources, using a mixture of coronal equilibrium, partial local thermodynamic equilibrium and less frequently collisional radiative modeling [20, 19, 11, 22, 23, 50]. Similar studies have been made with higher spectral resolution using Fabry-Pérot interferometry [26, 37].

The absolute accuracy of optical emission methods is poor, but overall trends, both parametric and spatial, are readily observed with minimal complication and cost. Emission spectroscopy is also the only technique mentioned here that can be used as a remote diagnostics, which is particularly valuable for space applications, as well as the only technique which can provide a qualitative measure of the plasma composition.

1.3.1 Emission Spectroscopy

Photons are emitted, with energy $h\nu$, from an atom when an excited orbiting electron decays to a lower energy level. The wavelength of the emitted photon, $\lambda = \frac{c}{\nu}$, is directly related to the change in electron energy resulting from decay by $\lambda_{pq} = \frac{hc}{E_p - E_q}$, where p is the excited electron energy level which decays to level q, and h and c are Planck's constant and the speed of light, respectively.

The rates at which the different atomic energy levels are populated and depopulated depend on the electron temperature and the total atomic and electron densities. Thus, measurement of the relative intensities of emission over a large range of wavelengths yields a signature of the main plasma properties. This is the basis of emission spectroscopy, where the photons emitted by the plasma are collected through a dispersive element, allowing the radiation to be viewed as a function of its wavelength.

The photons emitted by a particular transition are seen as a line in the collected spectrum, whose shape is determined by different broadening effects and whose total integrated intensity is determined by the radiant flux, Φ in W, as given by,

$$\Phi = N(p)A_{pq}(E_p - E_q)\frac{d\Omega}{4\pi} \tag{1.24}$$

where $N(p)$ is the number of electrons in level p in the observed region, $d\Omega$ is the solid angle subtended by the collection optics and, the Einstein coefficient, A_{pq} is the spontaneous emission probability per unit time for transition from p to q.

Equation 1.24 is applicable when the plasma is sparse enough to allow all emitted radiation to be collected by the optics without any reabsorption, i.e. the plasma is optically thin, and when the emission can be considered isotropic. The optically thin assumption is a good one due to the low density of the plasmas considered and the optical range of the experiments is 300nm-1000nm ($\Delta E_{pq} \leq 3eV$) which does not contain resonant lines for Ar or Xe.

The spectroscopic characterization of a broad spectrum of plasmas has taken place for years due to inherent benefits of such a non-contact measurement. Concurrently,

the field has developed a wide variety of methods of reducing spectral emission data based on different underlying assumptions on the behavior of the plasma in question.

Analysis of plasma emissions is in its most simplified state when the emitting ion (or atom) is in local thermodynamic equilibrium, brought about by high collisionality. Under the assumption of local thermodynamic equilibrium (LTE), the relative population density of two excited states are related by the Boltzmann equation to the electron temperature.

The criterion for complete LTE places a stringent requirement on the plasma density, which can be relaxed for emission from excited states near the ionization potential. Several authors have proposed criterion for both partial and complete LTE, which call for electron densities higher than observed in the Helicon plasma studied herewithin [31, 2, 36]. Partial LTE is considered applicable when the energy of the transition from level p to q, E_{pq}, is low enough that:

$$n_e >> 10^{19} T_e^{1/2} E_{pq}^3, \, m^{-3} \tag{1.25}$$

where both T_e and E_{pq} are given in eV [36]. For the expected densities of around 10^{19} m^{-3} this condition is met at wavelengths greater than 1.6 μm, which lies outside the range of our equipment and into the near infrared spectrum. LTE at visible wavelengths is approached with plasma densities greater than 10^{20} m^{-3}.

A similar simplification can be made for low density plasmas, where collisional depopulation effects can be neglected. The resulting Coronal Equilibrium model considers collisional excitation from, and radiative decay to, the ground state as the dominant contributors to emission spectra. Typically, plasma densities of less than $10^{16} m^{-3}$ are required for Coronal Equilibrium models to accurately predict emission, a criterion which may be met in the far plume [24].

A middle ground approximation is often utilized for plasmas in the density ranges normal to thruster applications. Collisional-Radiative Models (CRM) account for both methods of excitation and de-excitation, but require complex analysis which depends heavily on accurate cross section data.

Simplified Optical Emission Analysis

Collisional radiative modeling requires accounting for the many important processes leading to the equilibrium population of a given energy level. The main processes which populate p are summarized below along with their associated rate coefficients. Here the collisional processes are considered with electrons as the colliding body, but studies in Xenon have shown the importance of ion collisions as well, for high velocity ions in the cold plume region [17, 32]. Accounting for other collisional bodies does not effect the simplified model considered here, as shown later.

$$\begin{aligned}
Ar^{z-1}(q) + e^- &\xrightarrow{<\sigma_{qp}(v)v>} Ar^{z-1}(p) + e^- \\
Ar^{z-1}(q) + e^- &\xrightarrow{F_{qp}} Ar^{z-1}(p) + e^- + h\nu \\
Ar^{z} + e^- + e^- &\xrightarrow{\alpha_p} Ar^{z-1}(p) + e^- \\
Ar^{z} + e^- + h\nu &\xrightarrow{\beta_p} Ar^{z-1}(p) \\
Ar^{z-1} + e^- &\xrightarrow{S_p} Ar^{z}(p) + e^- + e^-
\end{aligned}$$

Here σ_{qp} is the cross section for collisional excitation, $<>$ denotes the ensemble average, F_{qp} is the collisional de-excitation rate coefficient for transitions from q to p, $\alpha(p)$ and $\beta(p)$ are the three-body and radiative recombination rates from ions of charge state z to $z-1$ and $S(p)$ is the ionization rate when the resulting ion is excited to level p. The rate at which level p, in ionization stage $z-1$, is populated by the above reactions is then given by Equation 1.26 [24].

$$\begin{aligned}
\frac{d}{dt}n_{z-1}(p) &= \sum_{q<p} < \sigma_{qp}(v)v > n_e n_{z-1}(q) \\
&\quad + \sum_{q>p}[F_{qp}n_e + A_{qp}]n_{z-1}(q) + [\alpha(p)n_e + \beta(p)]n_z n_e \\
&\quad - [\sum_{q<p} A_{pq} + n_e(\sum_{q<p} F_{pq} + \sum_{q>p} < \sigma_{pq}(v)v > \\
&\quad + S(p))]n_{z-1}(p)
\end{aligned} \tag{1.26}$$

In the state of quasi-static equilibrium, with a stationary plasma, the left hand side of the equation goes to zero for all excited states and Equation 1.26 can be recast as a

matrix of equations with excited state populations on the left hand side and $n_{z-1}(1)$ and n_z on the right. The solution for each state can then be expressed by,

$$n_{z-1}(p) = R_0(p)n_e n_z + R_1(p)n_e n_{z-1}(1) \tag{1.27}$$

where the rate coefficients $R_0(p)$ and $R_1(p)$ are proportional to both electron temperature and density [24]. These population coefficients can be solved by inverting the matrix set up by the rate equations, though it is outside the scope of the present work to do so.

If the plasma species considered is moving then the divergence of the particle flux can be subtracted from the left hand side of Equation 1.26 to calculate a more accurate population. The outflow of particles has no contribution in our simple analysis.

As mentioned earlier, the addition of heavy particle collisions will not effect the form of Equation 1.27, since by quasi-neutrality $n_i = n_e$, ion and electron collisions are interchangeable (except for the differences in coefficients R_0 and R_1) and the low temperature of neutral particles compared to electrons tends to make those collisional terms negligible in comparison.

The exact temperature dependencies of the coefficients R_0 and R_1 are unimportant as no solution is attempted here, but the various terms which arise from the different population mechanisms are reviewed by Fujimoto[24] and Griem[27], among others, if a more complete collisional-radiative model is desired. Instead, several simplifying assumptions can be made which allow an immediate zeroth order diagnosis of trends in the plasma parameters with relatively small data sets.

First, both forms recombination are neglected, which removes the R_0 term entirely. This is a good approximation for both neutral atoms and ions in the plasma plume, as discussed on page 76, though it is likely to break down for neutrals in the ionization region where wall recombination plays an important role in the plasma kinetics. Correspondingly, ionization can be neglected in the plume, somewhat simplifying the equations, though it will dominate near the center of the antenna.

Neglecting recombination allows the ratio of ion-to-neutral emission intensities

from any transition to be modeled by,

$$\frac{\Phi_i}{\Phi_n} = \frac{n_i(p)A_{pq}\lambda_{mn}}{n_n(m)A_{mn}\lambda_{pq}} = \frac{R^*_{1i}(p)n_i(1)}{R^*_{1n}(m)n_n(1)} \tag{1.28}$$

where $n_i(1)$ and $n_n(1)$ are the ground state ion and neutral densities respectively, and the A_{ij}/λ_{ij} terms are incorporated into the population coefficients and designated R^*_{1z}. The population coefficients are still functions of both electron temperature and density, but for low lying states where the corona equilibrium model is a good approximation, the collisional transitions from excited states are negligible and R_1 is dependent on electron temperature only [27]. In this case, the ratio of ion-to-neutral intensities is only a function of temperature and the fraction of ions versus neutrals (both in the ground state) in the collection volume. For coronal equilibrium

These assumptions allow trends in the ion-to-neutral fractions to be examined straightforwardly both spatially in isothermal regions, as done in Section 3.2, and parametrically if the changes in temperature are known. The same assumptions allow trends in the plasma and neutral densities to be examined separately, with plasma density $n_i = \sqrt{\Phi_i/R^*_{1i}}$ being used to find the neutral density $n_n = \Phi_n/R^*_{1n}n_i$.

Doppler Shift

One of the main goals of this study is to characterize the acceleration of ions exiting the Helicon thruster gas confinement tube. Shifts in the central wavelengths of the observed ion line emission due to the Doppler effect can be used to ascertain the axial evolution of ion velocities. The velocity of the radiating atom along the measurement line-of-sight results in a corresponding shift in the observed wavelength of emission by the relation in Equation 1.29.

$$v_{dop} = \frac{c\Delta\lambda}{\lambda_0} \tag{1.29}$$

A schematic showing the basic underlying physics behind the Doppler shift is shown in Figure 1-3. The figure shows the measured Doppler shift velocity along the viewing angle, $v_{dop} = v_z cos(\theta)$. The wavelength measured when the radiating particle

is moving towards the optics is shorter than it would be if stationary and since the blue region of the visible wavelengths is found at shorter wavelengths this is called a blue shift. An observer on the other side of the radiator would measure a longer wavelength which is correspondingly referred to as a red shift.

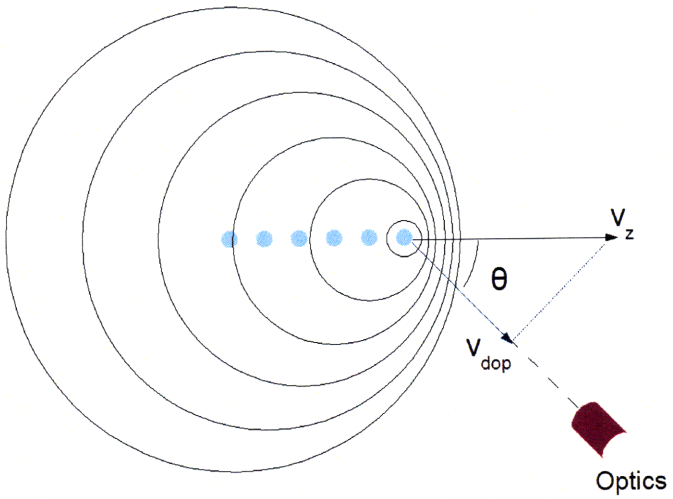

Figure 1-3: Wavefronts Emitted by a Moving Radiator with Axial Velocity, v_z, and its Projection to Angled Optics, v_{dop}

Spatial Resolution

Spectroscopic measurements are inherently volume integrated, with the optics used here collecting all non-absorbed radiation emitted within a long thin cone. The inhomogeneity of the plasma within this volume obscures the measured spectra. Tomographic techniques may be employed to deconvolve spatial profiles from a large range of offset measurements. The simplest of these techniques, the Abel inversion, can be used to reconstruct radial profiles from relatively few measurements when the source measured can be assumed cylindrically symmetrical.

Here we utilize the strong on-axis peak in plasma density observed in the near plume in Section 4.2 to model the collected emission as solely representative of the plasma properties within about 1 cm of the axis. The low electron density regions off axis are expected to contribute thinner ion line emission with proportionally larger

neutral populations.

Measurements of emission from the ionization region are similarly integrated over a region within 1 cm of the axis, which is the size of the neutral gas confinement tube. The transmissive properties of the quartz confinement tube, which have been observed to vary with time and position as the thruster is run for prolonged periods, are not quantified, necessitating the use of line emission intensity ratios as the primary diagnostic.

The angle of the optical fiber used to measure velocity by Doppler shift introduces the added complexity of sampling regions of different axial position. Emission just on the far side of the thruster axis from the optics will be from a denser and somewhat slower moving region than that on the near side, assuming plume expansion. The velocity vectors on opposing sides of the axis should diverge from the centerline symmetrically, so that the projection of the far side velocity vector along the line of sight will be smaller even if the magnitudes are equal. The total effect on the integrated profile is assumed here to average out so that any Doppler shifted peak corresponds solely to the axial velocity where the line of sight intersects the thruster axis, though this may underestimate the actual axial velocity at that point.

1.3.2 Electrostatic Probes

The typical Langmuir probe consists of an electrode which, when exposed to the plasma, collects a current largely dependent on the potential difference between the electrode and the local plasma. The characteristic curve that results when the current of the electrode is monitores as a function of its potential can be used to diagnose several key plasma parameters when certain assumptions are made about the behavior of the plasma.

An ideal I-V characteristic, shown in Figure 1-4, can be modeled for a quiescent DC plasma by Equations 1.30 and 1.31 for potentials below that of the local plasma. Below the plasma potential, electron flow to the electrode is retarded, but their thermal energy allows some electrons to overcome the potential barrier. Assuming the electrons are in thermal equilibrium allows the use of a Boltzmann factor to model

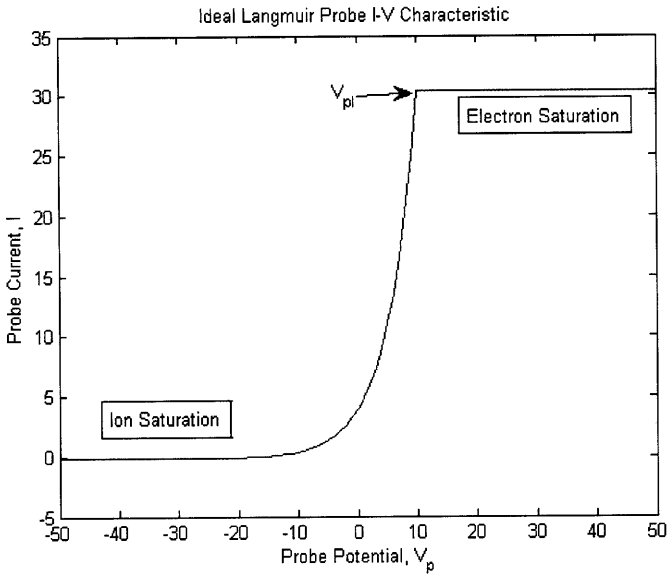

Figure 1-4:

electron current at retarding voltages, as given by,

$$I_e = en_0\sqrt{\frac{kT_e}{2\pi m_e}}e^{\frac{-(V_{pl}-V_p)}{kT_e}}A_p \tag{1.30}$$

where n_0 is the electron/ion density in the quasi-neutral bulk plasma, V_{pl} is the bulk plasma potential, V_p is the electrode potential, T_e is the electron temperature, m_e is electron mass, and A_p the collecting area of the probe.

At sufficiently negative probe potentials all electrons are effectively repelled and the current collected by the probe is comprised almost entirely of ions. This is the ion saturation region shown on Figure 1-4 where the probe collects what is called the ion saturation current given by,

$$I_i = \phi en_0\sqrt{\frac{kT_e}{m_i}}A_p \tag{1.31}$$

where m_i is the ion mass and ϕ is the fraction of bulk ions that enter the sheath which forms around the electrode. For an unmagnetized plasma $\phi = 0.61$ due to the Boltzmann factor at the potential difference needed to satisfy the Bohm criterion.

When a strong magnetic field is present, the ion motion is restricted along field

lines and the fraction of impinging ions decreases. For a perpendicular magnetic field a factor of $\phi = 0.49$ can be used [31]. At the thruster exit the externally applied magnetic field is about 900 G which corresponds to an ion gyroradius of 2 mm for a 0.1 eV ion. The probe used in this study is has a 1 mm diameter collecting surface so the ions may be somewhat magnetized with respect to the electrode near the exit. The choice of either factor is obviated by the fast axial flow of the plasma, which alters the dynamics from the idealized theory presented here. The simple analysis presented provides a way of determining the upper bound of the plasma density for a known temperature.

RF Effects

In RF plasmas the local potential fluctuates with the amplitude and frequency of the perturbing RF waves. The RF perturbation of the plasma potential adds a time dependent term in the exponential electron current function given by Equation 1.30 which alters the I-V characteristic of a conventional Langmuir probe.

Several methods have been proposed to compensate for the rapidly changing potential which include actively driving the probe at the RF voltages used to create the plasma as well as a multitude of passive techniques which allow the probe tip to follow the RF induced oscillations [49, 25]. The probe used in this report does not incorporate any of the RF compensation methods mentioned, but makes use of RF filters outside of the chamber to suppress noise.

An uncompensated probe can still yield useful information if care is taken in the analysis of the I-V characteristic and the RF fluctuations are not too much larger than the electron temperature. The ion current drawn by the probe is not dependent on the plasma potential and therefore can still be measured accurately by a probe with a sufficiently negative bias. The electron current at probe voltages near the ion saturation regime has also been shown to follow the same exponential voltage dependence with and without RF compensation [49, 40]. The addition of RF compensation serves to extend this region of exponential fit to more positive values of probe tip potential.

The time-averaged effect of RF oscillations leads to a factor in Equation 1.30 dependent on RF voltage magnitude and electron temperature which causes a shift in the I-V characteristic to more negative values of probe voltage [28, 40]. The measured floating potential is therefore less than the DC floating potential of the plasma as a result. Such results have been reported when the fluctuation in plasma potential due to RF is assumed sinusoidal, yielding the average electron current equations shown below

$$< I_e >= \frac{1}{\tau}\int_0^{\tau} en_0\sqrt{\frac{kT_e}{2\pi m_e}}e^{\frac{-(V_{pl}+V_{rf}cos(\omega t)-V_p)}{kT_e}}A_p dt \tag{1.32}$$

$$ln < I_e >= \frac{V_{pl}}{kT_e} + ln\left(\frac{1}{4}A_p en_0\sqrt{\frac{kT_e}{2\pi m_e}}\right) + ln[I_0\left(\frac{V_{rf}}{kT_e}\right)] \tag{1.33}$$

where V_{rf} is the amplitude of RF induced fluctuations at frequency ω and the electron current is being averaged over a period τ. These equations are no longer applicable when the probe potential reaches $V_{pl}-V_{rf}$ as the current enters the electron saturation regime.

The effects of plasma potential oscillations on ion current are neglected based on the idealization of ion current collection independence from attracting potential. The measurements described in the following sections suggest a linear dependence of ion current on the probe tip potential and so, following the above model, the RF effects would average out regardless.

Chapter 2

Experimental Apparatus

Experiments were performed inside the MIT Space Propulsion Laboratory ASTROVAC vacuum chamber. The chamber, shown in Figure 2-1, is roughly 1.5 by 1.6 m with a pumping speed of roughly 7500 L/s on Argon obtained using two CTI-Cryogenics cryopumps (CT10 and OB400). Pressure in the chamber is monitored using a cold cathode gauge with a calibration factor of 1.3 for Argon and 2.9 for Xenon.

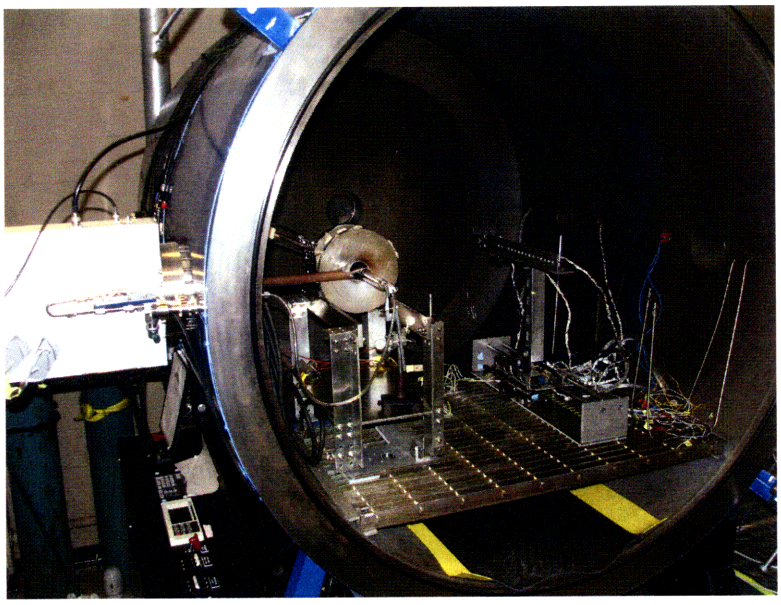

Figure 2-1: The Open ASTROVAC Vacuum Chamber. Inside: mHTX (left) and Emission Spectroscopy Experiment (right) Installed, Also Visible Are Side (far right) and Back Window Ports. Outside: Matching Network (far left) and Gas Propellant Feed.

2.1 Thruster Configuration

The miniature Helicon Thruster Experiment is of minimal complexity, consisting mainly of a quartz neutral gas confinement tube, a half turn helical antenna and an electromagnetic inside of the ASTROVAC chamber.

The thruster is powered by an RFPP RF-10S/PWT unit with a maximum power of 1.2kW at 13.56 MHZ. An L-section network is used for impedance matching where the plasma and antenna are the load. More thorough discussions of the thruster design can be found in the prior literature [48, 45, 42].

The power set point for the RF-10S unit is controlled by a LabView 8 virtual instrument, which then displays the forward, reflected and net delivered RF power as measured by the RF supply. Manual control of the matching network is necessary to ignite a plasma and enter the Helicon mode of thruster operation.

A rough match is made by adjusting a Jennings 7-1000 pF variable capacitor while monitoring amplitude of the antenna current on a Tektronix TDS 210 Oscilloscope connected to a Pearson 6600 current transformer. Fine adjustments are made with a Comet 5-100pF capacitor providing the reactance leg of the L-section network. The current, and correspondingly the forward power, can be maximized without establishing a plasma as the antenna is susceptible to coupling elsewhere.

A reliable ignition procedure, found through extensive experimental experience, was utilized in which the matching network operator uses the coarse adjustment capacitor to set the current amplitude at about half of its maximum value. The fine adjustment capacitor is then used to tune the current amplitude up and past its maximum until a sudden jump in amplitude is seen. Once the jump occurs a plasma has been established and the coarse and fine knobs may be adjusted to minimize reflected power.

2.1.1 Magnetic Field Strength Control

A new electromagnet is used which is shorter and thus has a larger field strength gradient than the magnets discussed in the prior literature. The electromagnet consists

of 11 layers of 2 guage, square cross-section copper bar each with 12 turns with a 4.4 cm inner bore diameter. The magnet was designed to provide a higher maximum axial field strength than the prior magnets, and reaches 0.2 T when supplied with 180 A of current. The current is provided by an Agilent N5761A 6V/180A System DC Power Supply controlled by a LabView 8 virtual instrument described in [48].

The axial field strength of the electromagnet was measured at several values of input current using a AlphaLab Inc. DC Magnetometer equipped with an axial probe. The results are shown in Figure 2-2 matched with a model of the axial field provided by a solenoid, given by Equation 2.1, which is fit to the data to find effective values for the solenoid radius, r_{eff}, and number of turns, N_{eff}. The solenoid has a total length of L=93 mm with fit parameters r_{eff}=41.75 mm and N_{eff}=27.42 turns.

$$B_z = \frac{\mu_0 I N_{eff}}{L/2}\left(\frac{L/2-z}{\sqrt{r_{eff}^2+(L/2-z)^2}}+\frac{L/2+z}{\sqrt{r_{eff}^2+(L/2+z)^2}}\right) \tag{2.1}$$

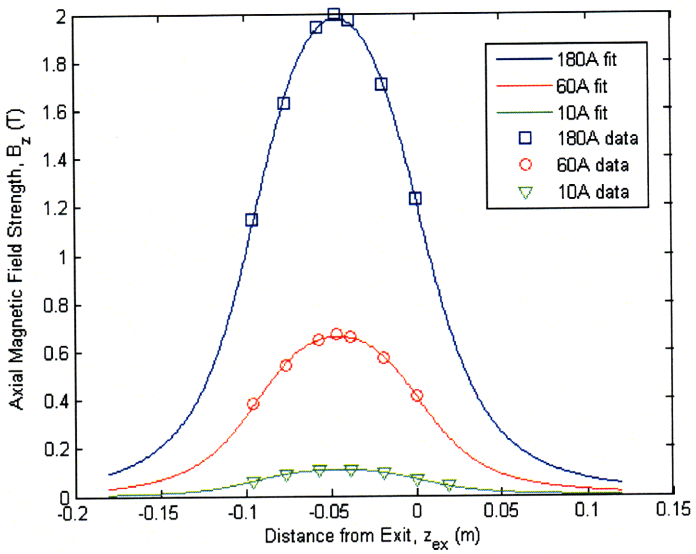

Figure 2-2: Measured Axial B Field vs. Axial Distance from Thruster Exit for Several Values of Magnet Current. The Model Fit Is Shown at Several Current Values Compared to Experimental Data

An overlay of the applied field topography of lines emanating from within the confinement tube on the visual thruster plume is shown in Figure 2-3. It is visually evident that the plasma plume is not strictly bound to the field lines.

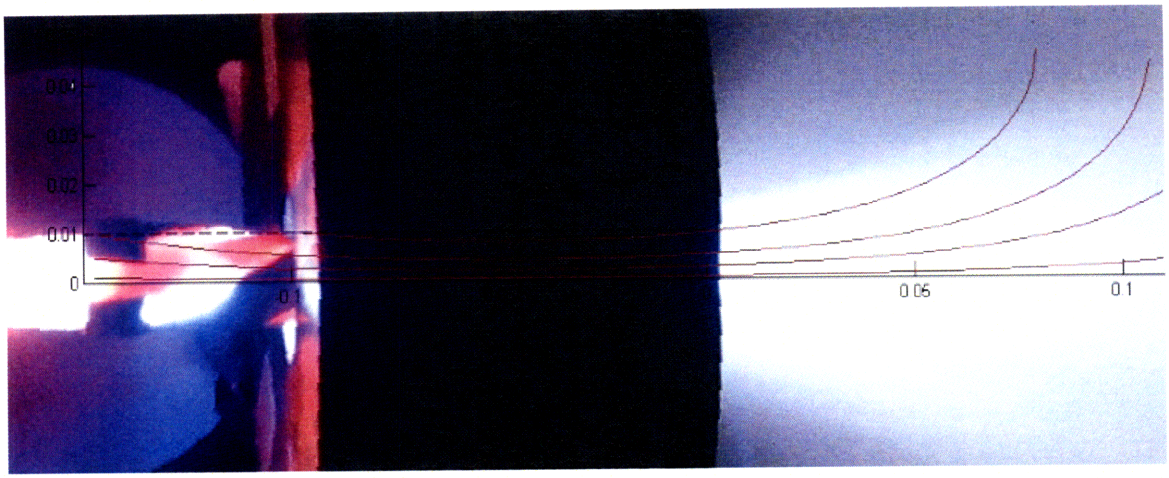

Figure 2-3: mHTX Firing at Nominal Operating Conditions with Overlaid Applied Magnetic Field Lines. X-Axis and Z-Axis Locations Measured in Meters from Antenna Start. Visually, Ionic Plume is Not Following B-Lines

2.1.2 Mass Flow Control

The earliest portion of the mHTX study was carried out with flow control and measurement provided by an Omega FMA6500 Series Digital Mass Flow Controller. The FMA6500 is capable of forcing flow from 0 to 100 mL/min, calibrated for Nitrogen, with a calibration factor of 1.4573 for Argon.

The operation of the FMA6500 began to deteriorate over the course of the study in the presence of RF radiation. Eventually, it became untenable for use during Helicon experiments and was replaced by a capillary tube. The capillary chokes ensures that the flow entering the chamber is choked. The flow rate is then controlled by adjusting the back pressure at the Argon tank using a Concoa Regulator with a 5-200 psig indicator.

The flow rate through the capillary is monitored using a cold cathode gauge installed in the chamber to measure the background pressure. The background pressure is then correlated with the mass flow rate using two Omega FMA-A2400 series mass flow controllers, allowing 0-10 mL/min flows calibrated for Xenon, to supply a known flow into the chamber. The results of one such calibration is shown in Figure 2-4, with the a linear regression curve overlaid to illustrate the general dependency of chamber pressure on flow.

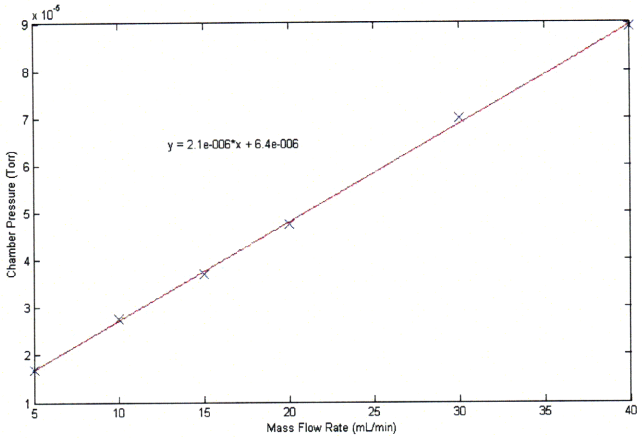

Figure 2-4: Chamber Pressure vs. Mass Flow Rate of Argon

Changes in outgassing characteristics of the chamber and its contents add to the uncertainty of using the backpressure monitoring method of flow rate measurement. Overall, the method was found to be repeatable to within 1 sccm.

2.2 UV-Visible Spectroscopic System

Radiation is collected by Ocean Optics Model 74-UV, f/2 fused silica collimating lenses attached to four separate 200 μm diameter patchcords, which are delivered through a vacuum feedthrough to the receiving end of a 1-m long Princeton Instrument QFB-455-3 four legged fiber optic bundle. The 10-mm bundle contains four groups of 200 μm fibers, with three fibers per bundle, which transmit from 190-1100 nm at the spectrometer end. An Acton FC-466-020 adjustable fiber adapter is used to position the bundle at the entrance slit of the spectrometer.

The threaded collimating lenses were inserted into specially tapped holes in the aiming apparatus shown installed in the chamber in Figure 2-5. The apparatus is connected to a linear stage driven by a single stepper motor. Two of the lenses view the thruster radially while a third is on a rotatable arm and is used to measure the Doppler shift in the plasma plume. The angle of the third fiber with respect to the thruster axis was varied from 41^o to 58^o. This angle corresponds to θ in Figure 2-6.

The axial position of the fiber which views the gas confinement tube is measured

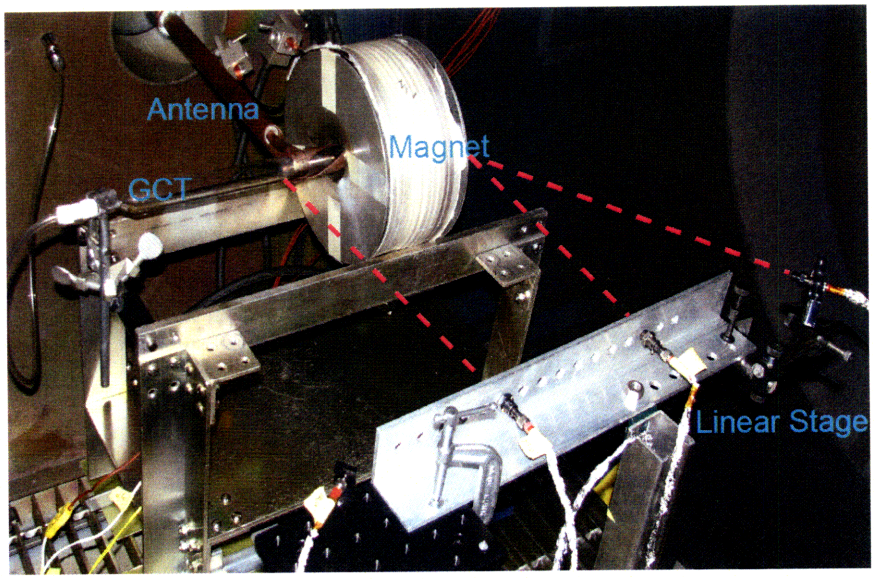

Figure 2-5: Emission Spectroscopy Experiment Collecting Optics Installed on an Axial Stage Moving Inside the Vacuum Chamber

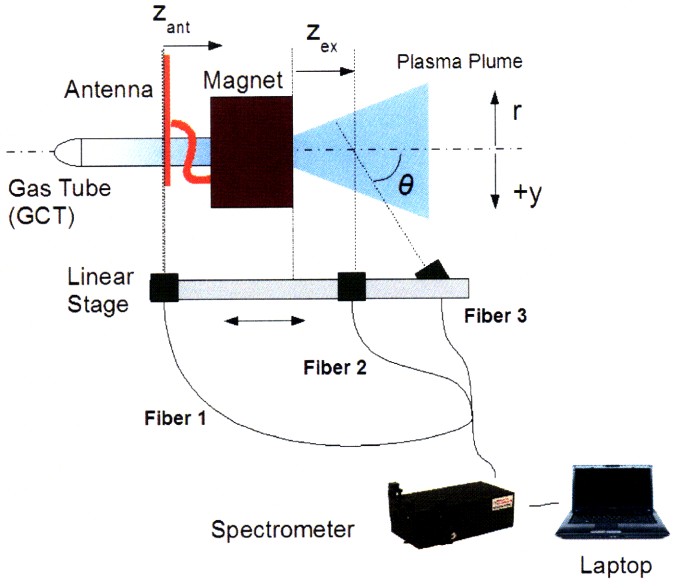

Figure 2-6: Emission Spectroscopy Experiment Schematic

from the start of the antenna with the positive direction facing downstream and is labeled z_{ant} in Figure 2-6. The axial position of the radially viewing fiber in the plume, z_{ex} in Figure 2-6, is measured from the exit plane of the electromagnet, and the angled fiber axial position is measured similarly by the point where its line-of-sight crosses the thruster axis. All three fiber positions are checked before and after each experiment by illuminating the point where they cross the axis with a laser attached to the uncollimated end of the patchcord.

The radiation collected from the bundle is dispersed by an Acton Research Spectra Pro 2750 Spectrograph, which has a 750 mm focal length, an f/9.7 aperture ratio and three selectable gratings: 3600 grooves/mm, 1800 grooves/mm and 300 grooves/mm. The 300 g/mm and 1800 g/mm gratings are blazed at 500 nm for dispersion of 4.36 nm/mm and 0.62 nm/mm respectively. The 3600 g/mm grating is centered at 240 nm for a dispersion of 0.31 nm/mm.

The dispersed light is collected on the same end of the monochromator as it entered, through a narrow 1-2 μm slit, by a CCD camera at a 1:1 ratio. Two CCD models were used during this study. The Roper Scientific CoolSnap K4, with its 2048 x 2048 pixel array at 7.4 x 7.4 μm pixels, was used in order to collect light from all four legs of the fiber bundle. The K4 has a quantum efficiency $> 40\%$ from 400 to 600 nm. Finer work was accomplished with the CoolSnap Cf_2, which has a smaller collection area at 1392 x 1040 elements, with 4.65 x 4.65 μm pixels and a quantum efficiency $> 30\%$ from 400 to 600 nm.

2.2.1 Intensity Calibration

Intensity calibration was achieved with an Oriel Instruments 200W calibrated, quartz halogen, tungsten filament lamp. The lamp was placed in the position of the experiment, with each of the four collimated fibers placed 50cm away, one at a time with measurements collected at each grating position calibrated in this study.

The data provided by Oriel for the tungsten lamp corresponds to collection through an aperture of 1 cm^2. The UV collimators have a diameter of 5 mm, and thus collect roughly over an area of 0.7853 cm^2, with a divergence of 2^o, allowing a planar

approximation of the irradiance.

The irradiance curve for the calibration lamp provided by Oriel is plotted along with the intensity measured by the ionization region viewing fiber are plotted in Figure 2-7. The figure shows that optical system collects radiation well in the 500-750 nm region and is still transmissive up to 900 nm, but has limited performance at UV wavelengths.

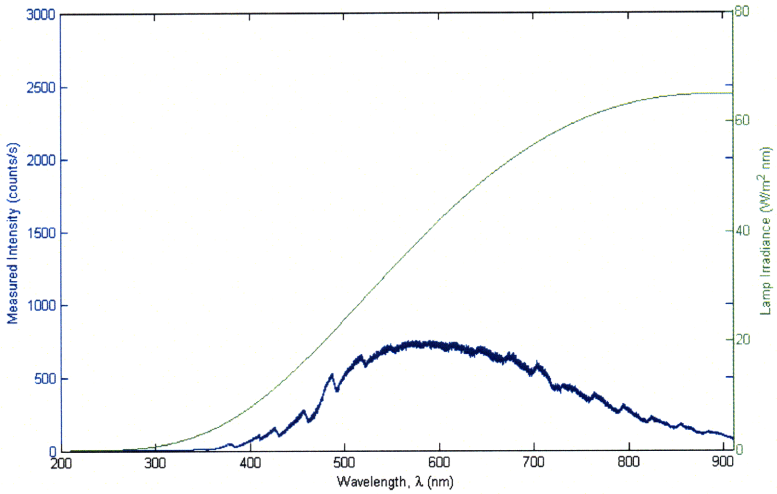

Figure 2-7: Emission Intensity of Calibration Lamp Measured by Ionization Region Fiber and Lamp Irradiance vs. Wavelength

A calibration factor is obtained for each fiber by dividing the lamp irradiance by its measured intensity in counts/s. The resulting factor, shown in Figure 2-8 for the antenna viewing fiber, is multiplied by the measured intensity of our spectra to produce intensity calibrated results in W m^{-2} nm^{-1}. Integration of a line profile then yields results in W m^{-2} .

The mean calibration factor for the ionization region fiber in the main region examined in this study, from 433 nm to 436 nm is 0.103 W s $counts^{-1}$ nm^{-1} m^{-2} with a standard deviation of 4%. The calibration factor for the fiber which views the plume radially is simply 1/7 the factor used for the ionization region fiber.

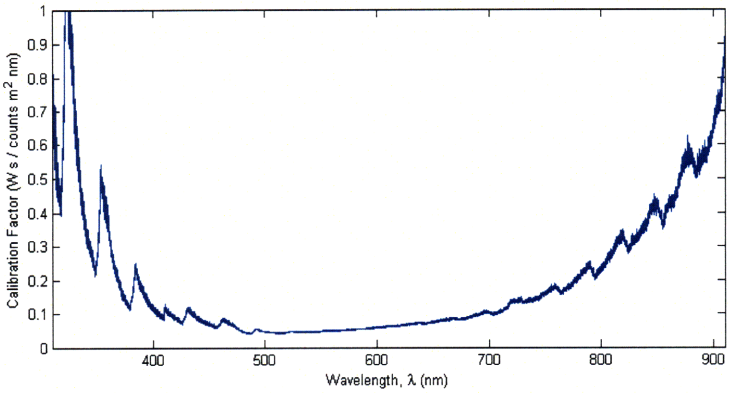

Figure 2-8: Intensity to Irradiance Calibration Factor vs Wavelength for the Ionization Region Fiber

2.2.2 Instrument Function

The instrument function of the optical set-up was examined using a Mercury lamp. The Hg I line at 435.8nm as collected by the K4 CCD is shown in Figure 2-9 exhibiting the characteristic shape of a Voigt distribution. The full width at half maximum (FWHM) of the curve is 3.8 pm, which would correspond to a temperature of 5800 K (0.5 eV) if attributable to Doppler broadening.

The typical Ar II line measured by the K4 in the same spectral region has a FWHM around 7 pm (1.8 eV). For comparison, the main Ar II line of interest at 434.8 nm, had a measured FWHM of 4.2 pm (0.6 eV) when measured in the ionization region of the thruster by the Cf2 CCD at similar operating conditions.

The WinSpec program used to capture data from the CCD and spectrometer is equipped with a simple tool for converting its inherent data files into ASCII format, but with only six digits of output wavelength. The truncation at three decimal places introduces noticeable inaccuracies at higher wavelengths where there is a sub-picometer pixel-to-pixel resolution, to the extent that certain wavelengths have two attributed intensities. In the main region of interest, centered at 434.4 nm, the inter-pixel resolution is around 0.78 pm on the Cf_2 CCD and 1.4 pm on the K4 CCD.

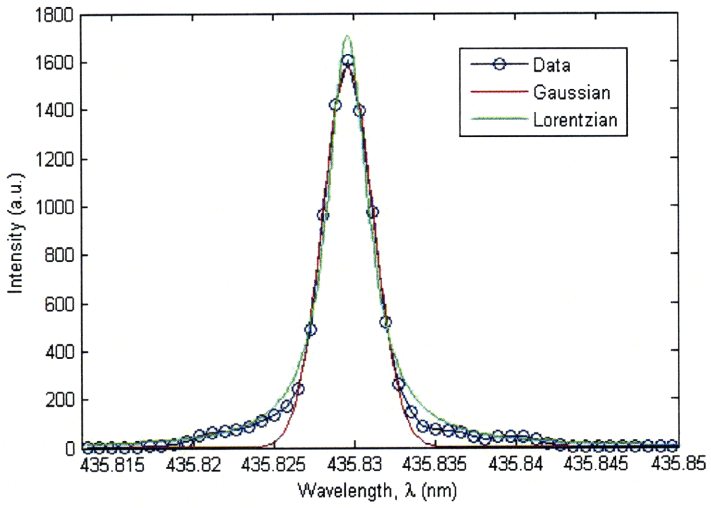

Figure 2-9: Emission Intensity of a Mercury Lamp vs. Wavelength using the K4 CCD with Gaussian and Lorentzian Fits Superimposed

2.2.3 Doppler Shift Method Validation on BHT-200

A Doppler shift, similar to that described in section 3.3, study was performed on the well characterized Busek BHT-200 Hall Effect Thruster [38, 29, 30, 10]. The 3600 g/mm grating was used with the Cf_2 CCD to take simultaneous spectra from a radially viewing fiber and a 45^o angle fiber which intersect at the thruster axis several cm downstream of the exit plane.

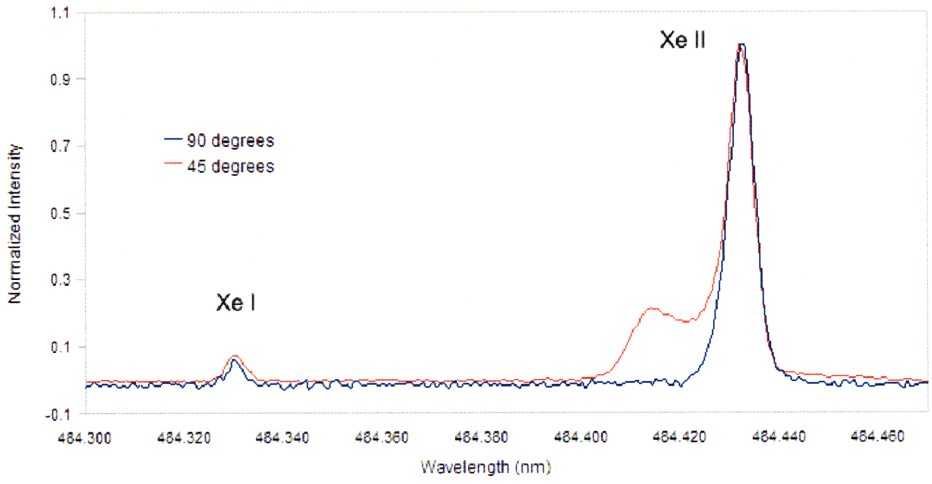

Figure 2-10: Normalized Emission Intensity vs. Wavelength Collected Radially and at a 45^o Angle from Thruster Axis for Doppler Shift Examination of the BHT-200 Operating at 250 V, 0.85 A and 0.836 mg/s of Xenon

Two relatively bright lines at 484.329 nm (Xe I) and 484.433 nm (Xe II) were examined to determine the Doppler shift due to directed ion motion. The resulting spectra, shown in Figure 2-10, indicate a substantial population of nearly stationary ions coexistent with a population shifted to a Doppler velocity of 11.3 km/s along the viewing angle.

The measured Doppler velocity corresponds to an axial velocity of 16 km/s for a strictly axial flow. Laser induced fluorescence measurements of the velocity profiles near the exit of the same thruster revealed axial velocities accelerating from 13.8 km/s at the exit plane to 16.5 km/s 20 mm downstream with symmetrically divergent radial velocities along the line of sight [29]. The radial velocities were shown to reach as high as 10 km/s, leading to velocity vectors diverging from the thruster axis by as much as 31^o.

The Doppler velocity of the shifted peak is once again estimated to be within the velocity corresponding to a half-pixel shift, which is here 396 m/s along the measurement angle or 561 m/s for an axial velocity. The axial velocity measured by the simple Doppler shift technique is then equal to that measured by LIF within the uncertainty of the measurement.

The Doppler broadening temperature of the radially measured Xe II line of 4.16 eV is lower than measured by LIF at the thruster exit, which is likely due to the volume integration containing a large population of ions with lower average radial speeds. The neutral line broadening temperature is only 0.98 eV for comparison, which is above the expected neutral Xe temperature and therefore likely indicative of the instrumental limit.

2.3 Electrostatic Probe Apparatus

An uncompensated planar Langmuir probe is used which consists of a 2 mm diameter tungsten rod enclosed in a 1 mm thick dielectric alumina tube. The exposed end of the tungsten electrode is placed flush with the end of the alumina tube so collection may be assumed solely along the exposed face.

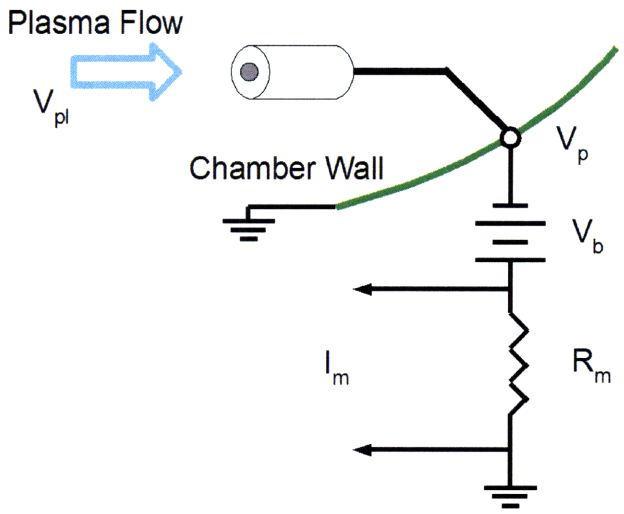

Figure 2-11: Circuit Diagram for the Uncompensated Langmuir Probe

The tungsten electrode, which is at the probe tip potential V_p, is connected to the negative terminal of a DCS 300-3.5E Sorensen Power Supply, used to provide the bias voltage V_b. The Sorensen is connected on the positive side to chamber ground via a 3.4 kOhm measurement resistor. Measurements of the current across the resistor were made for separate experiments by either a Fluke II Multimeter or a NI USB 6009 DAQ. A circuit diagram is given in Figure 2-11, where the plasma potential is labelled V_{pl}.

The main use of the probe is to measure the ion current as a function of axial position. Sizing of R_m based on ion current is accomplished by estimating an upper bound at the exit. Assuming a utilization efficiency of unity, the collection current can be estimated using,

$$I_m = A_p J_i = A_p \frac{e\dot{m}\eta_u}{m_i A_{ex}} \tag{2.2}$$

where A_p is the exposed area of the probe, J_i is the ion current density and A_{ex} is the area at the exit which is set by the confinement tube. At the nominal flow rate used in this study (16 sccm) the probe current is 14 mA. An R_m of 3.4 kΩ was chosen to keep the measurement voltage below 50 V at the exit, while allowing a large range of currents to be measured at locations further downstream.

Chapter 3

Optical Emission Spectroscopy of the mHTX

The emission spectroscopy experiments were aimed at simultaneous characterization of the axial trends in ionization fraction and temperature in the antenna and near-plume regions with Doppler shift measurements to capture the expected ion acceleration as the plasma expands from the thruster exit. The ensuing section describes the results of this characterization effort with comparisons to a simple model.

3.1 Axial Ionization Region Scans

The linear stage described in the previous section was used to make axially resolved measurements of the emission characteristics in the antenna region, collected through radially viewing collimated optics. The optical region of interest for all axial scans spans from 432.9 nm to 435.9 nm, encompassing the Ar lines shown in Table 3.1, from NIST tabulated data, where I_{rel} is the relative intensity of emission measured in representative low density sources [46]. The spectra at all axial positons are shown simultaneously in Figure 3-1.

A linear wavelength calibration was made using the seven visible lines with listed intensity values collected 3 mm upstream of the antenna. The results of the linear calibration yielded residuals with a clearly parabolic shape in wavelength. When a

Species	λ (nm)	I_{rel}	A_{ij} (s^{-1})	E_i (eV)	E_j (eV)
Ar II	433.1200	200	5.74e+07	16.7485279	19.6103067
Ar II	433.2030	50	1.92e+07	16.4441135	19.3053437
Ar I	433.3561	100	5.68e+05	11.8280704	14.6882894
Ar I	433.5338	50	3.87e+05	11.8280704	14.6871173
Ar II	433.7071	-	3.4e+07	21.4264882	24.2843928
Ar I	434.5168	25	2.97e+05	11.8280704	14.6806494
Ar II	434.8064	800	1.171e+08	16.6438534	19.4945327
Ar II	435.2205	50	2.12e+07	16.4573768	19.3053437

Table 3.1: Properties of the Lines Observed in the Small Bandwidth Axial Scans

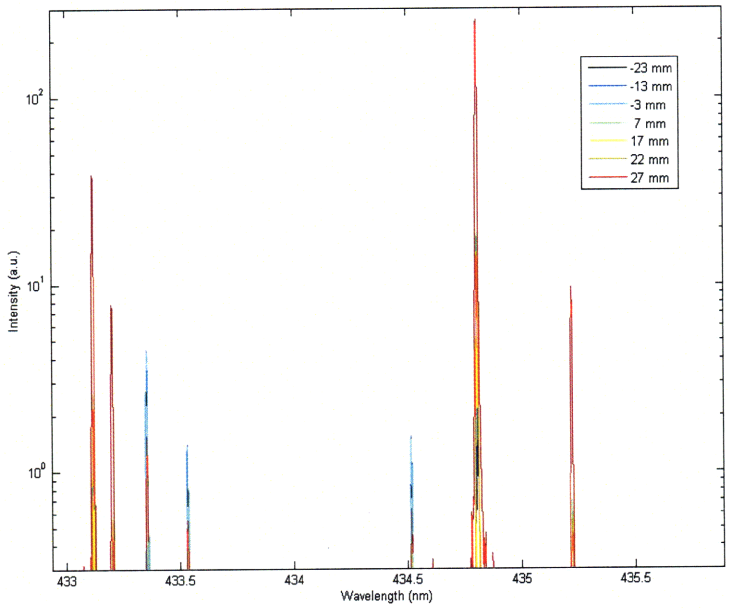

Figure 3-1: Emission Intensity vs Wavelength at Various Distances from the Start of the Antenna. Operating at Nominal Conditions

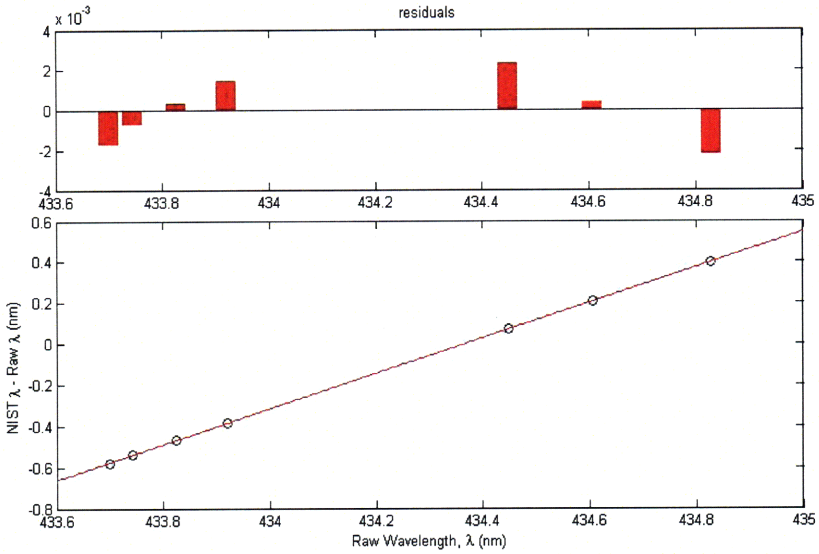

Figure 3-2: Discrepancy of Raw Wavelength with NIST Wavelength vs. Wavelength with Residuals from a Linear Fit

second order polynomial calibration was used instead of a linear one the maximum discrepancy of any line with the NIST tabulated wavelengths dropped from $2.7x10^{-3}$ nm to $6.8x10^{-5}$ nm.

The wavelength calibration makes use of Gaussian curve fits to the observed lines as indicators of their position in the spectrum, as opposed to use of the raw peak positions for higher resolution. The results at 3 mm upstream of the antenna were then chosen to represent spectra at all positions because of the relatively high strength of neutral Argon emission at that position, leading to the highest overall goodness of fit for the Gaussian line representations. Neutral Argon emission is more reliable than ion emission for wavelength calibration due their slow and largely isotropic motion. The calibrated line peaks are within 0.1 pm of the NIST wavelengths when the emission signal to noise ratio is large enough to accurately locate the line peak (i.e. goodness of Gaussian fit greater than 0.97).

The collection optics begin to be obstructed by the antenna at axial positions greater than 29 mm from the start of the antenna. A signal is still obtained as far as 37mm from the antenna, enough so to saturate the Ar II lines at 433.1200 nm and 434.8064 nm when a 90 second integration time is utilized. The high intensities

measured at obstructed positions may be caused by spurious reflection effects.

References herewithin to measured emission intensities refer not to the intensity at the peak, but to the area under the Gaussian fit to the line shape. Trapezoidal integration of the area under the raw lines was only 2% higher on average, with substantial deviations arising only at small values of signal-to-noise.

The emission intensity ratios of all four collected ion lines can be seen in all their combinations in Figure 3-3. The ion emission intensity ratios, in general, appear to rise gradually to a maximum around 17 mm downstream of the antenna feedthrough before dropping off slightly. Overall, the changes are relatively small compared to intensity changes, with standard deviations of less than 13% of the mean values for the ratios of the 433.1nm line to lines at 433.2nm and 435.2nm. The standard deviation is less than less 7% of the mean for all other ratios plotted.

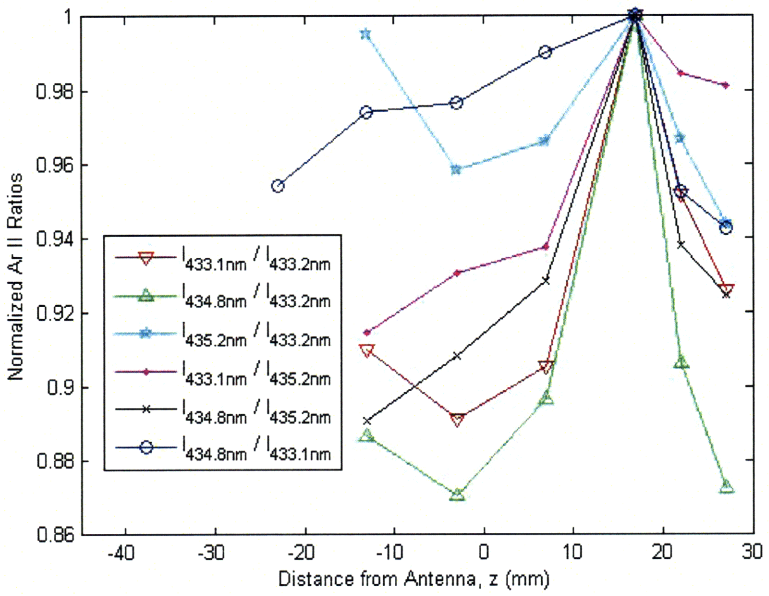

Figure 3-3: Ratio of Ion Line Intensities Measured by a Radially Viewing Fiber Normalized to Individual Maximums vs. Fiber Distance from Antenna Operating at 770W, 0.475 mg/s of Argon and 1333G

Emission intensity ratios of lines within the Ar I spectrum in this bandwidth are similarly spatially distributed, but with even smaller deviations, the largest of which is only 2.5% of the mean. The results suggest either a thermal equilibrium of the electrons, even upstream of the ionization region, or that the given line ratios are

steep functions of electron temperature in this regime.

The Gaussian fits are also used to compare line widths between species as a function of axial position. The full width at half maximum (FWHM) of each radially viewed line is dependent on the distribution of radial velocities due to the Doppler effect. We can make an initial assumption of thermally distributed radial speeds, allowing the use of Equation 3.1 to estimate the temperature of the emitting species, where λ_0 is the central wavelength of the broadened line [36].

$$\Delta\lambda = \frac{2\lambda_0}{c}\sqrt{\frac{2kTln(2)}{m}} \tag{3.1}$$

The thermal broadening assumption leads to high neutral temperatures estimates of around 1.6 eV, as shown in Figure 3-4. At first blush, this unexpectedly large width might be attributable solely to the instrument function of the spectroscopic apparatus, but the appearance of lower temperature Ar I lines in the plume, discussed in the following section, and even thinner Hg lines, discussed in the previous section, obfuscates the problem. It is worth noting that Figure 3-4 shows no temperatures for the 433.5 nm and 434.5 nm Ar I lines past 7 cm downstream of the antenna. This is because the neutral emission intensity from these lines is no longer above the instrument noise at these locations due to the high degree of ionization.

The neutral particle temperature can be estimated alternatively by noting that the ion flux to the dielectric wall is balanced by the counter flux of neutral particles created by recombination at the surface. The magnetic field strength varies from 1.33 kG in the center of the magnet ($z_{ant} \simeq 100$ mm), where the field is parallel to the wall, to around 160 G at z_{ant}=0, where the field intersects the wall at an angle, α 22^o.

$$n_n v_{th_n} \approx n_i c_{s_i} sin\alpha \tag{3.2}$$

Substitution of the ion acoustic speed into Equation 3.2 yields Equation 3.3.

$$T_n \approx \left(\frac{n_i}{n_n}\right)^2 sin^2\alpha T_e \tag{3.3}$$

Assuming the ion-to-neutral emission ratio is driven primarily by the ion-to-

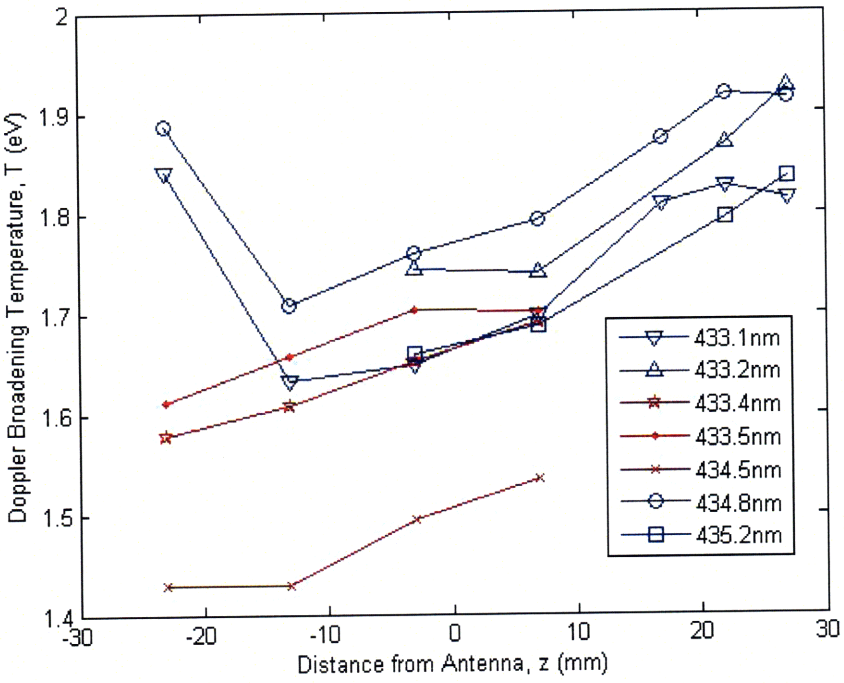

Figure 3-4: Thermal Temperature Corresponding to Doppler Broadening of Lines Measured by a Radially Viewing Fiber vs. Fiber Distance from Antenna Operating at 770W, 0.475 mg/s of Argon and 1333G

neutral density ratio, $x = n_i/n_n$, and the mean electron energy in the ionization region is driven to 20 eV by the length of the antenna allows the estimation of the neutral temperature. Setting the ionization fraction, $f_i = n_i/(n_i + n_n) = x/(x + 1)$ (neglecting multiply charged ions), 27 mm downstream of the antenna to 90%, and assuming the temperature is constant through the entire region, the ratio x at the antenna is only about 18%, and Equation 3.3 gives a nuetral temperature of 1100 K (0.1eV).

Thermocouple measurements from White's study of the same thruster show a steady-state outer wall temperature of around 700 K (0.06 eV) under the antenna [53]. The neutral population is typically assumed to equilibrate near this temperature due to wall collisions. The melting point of quartz is around 1900 K (0.16 eV), which caps the expected neutral temperature. Using these two temperatures as bounds, the ratio x should be between 0.15 and 0.24 at $z_{ant} = -3$ mm, corresponding to ionization fractions of 0.88 and 0.92 at z_{ant}=27 mm.

The assumption that the electron temperature is constant and that the conditions which lead to Equation 1.28 are met in the ionization region are not well justified. Indeed, similar optical emission experiments on a Helicon plasma showed the emission intensity of the Ar II line at 488 nm follows the electron temperature with a strongly peaked axial profile in the ionization region [50].

The FWHM of all measured lines shows statistically little change along the sampled region, with a standard deviation of 2.2% at 434.8 nm and 4% at 433.4 nm, but there is a general rise in Doppler temperature downstream of the antenna start. The small but steady increase in the radial ion velocity downstream may be attributable to the magnetic nozzle effect as the ions enter a strong positive gradient in the applied field.

Measurements of the thruster plume show slightly more variation in line width, with a standard deviation of 4.8% at 434.8 nm and 4.7% at 433.4 nm, with an overall trend for the ions of increasing width with distance from the exit. The width of the 434.8 nm measured 3 cm downstream of the exit is only 0.5% larger than that measured 2.7 cm upstream of the opposite end, while the Ar I line at 433.4 nm is

22% thinner.

The measured ion-to-neutral ratios, pictured in Figure 3-5, exhibit an exponential growth from -13 to 27 mm, over a characteristic length of 7.5 mm. All three ratios plotted have nearly identical growth rates, with a standard deviation of only 0.6%. The growth rate is much slower further than 13 mm upstream of the antenna, signaling an upstream limit to the ionization region. The emission intensities profiles in this region are only meaningful when taken as ratios due to non-uniformities in the transmissivity of the quartz confinement tube, and partial view obstruction by the antenna.

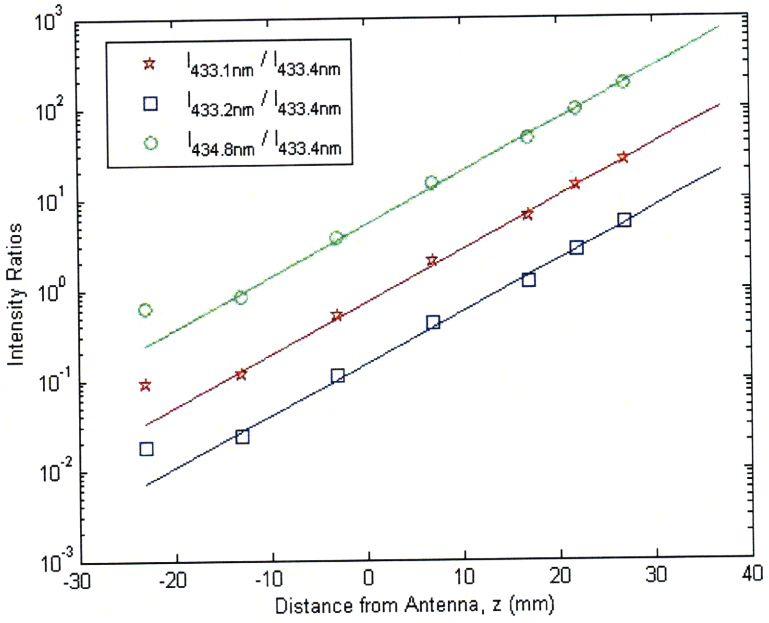

Figure 3-5: Ratio of Ar II to Ar I Line Intensities Measured by a Radially Viewing Fiber vs. Fiber Axial Distance from the Start of the Antenna. Operating at 770W, 0.475 mg/s of Argon and 1333G

Parametric scans were conducted to examine the effects of RF power, magnetic field strength and propellant flow rate on the emission characteristics. Increasing the mass flow rate has an obvious effect on the ionization region shape, as shown in Figure 3-6, despite some spurious data at the upstream end of the ionization region, which moves downstream as the flow rate is increased. A flow rate of 0.267 mg/s (9 sccm) results in the same ion-to-neutral emission 27 mm downstream of the antenna as

the nominal 0.475 mg/s (16 sccm) case, but the exponential growth length is nearly double at 14 mm. Increasing the flow rate additionally, to 0.683 mg/s (23 sccm), shifts the ionization region further downstream, with little change in the measured exponential growth length.

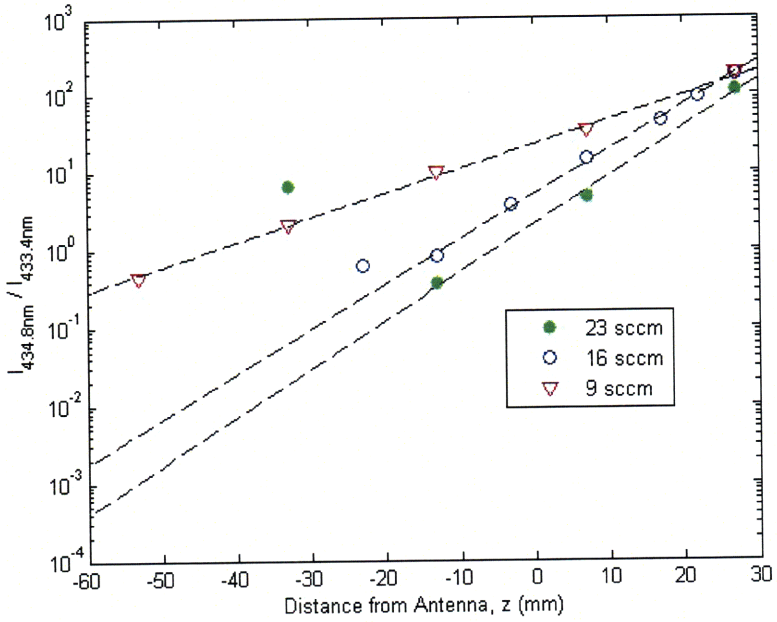

Figure 3-6: Ratio of Line Intensities at 434.8nm and 433.4nm Measured by a Radially Viewing Fiber vs. Fiber Distance from the Antenna for Three Values of Argon Volumetric Flow Rate, Operating at 770W and 1333G

Changes in magnetic field strength have limited correlation to changes in emission from the ionization region, as demonstrated by Figure 3-7. The exponential curves of best fit grow over lengths of 9 and 8.5 mm for field strengths of 667 and 2000 G respectively. The furthest downstream measurement of the Ar II/Ar I ratio doubled as the field strength doubled from 667 G to 1333 G, but varied little as the field strength was increased to 2000 G.

Variation of the delivered RF power had even less of an effect on the emission profiles. As Figure 3-8 shows, the ionization fraction indicated by emission is nearly the same as the nominal case when brought down to 580 W. The ionization fraction is similar when the power is increased to 950 W, with an apparently shallower growth over a characteristic length of 8.7 mm.

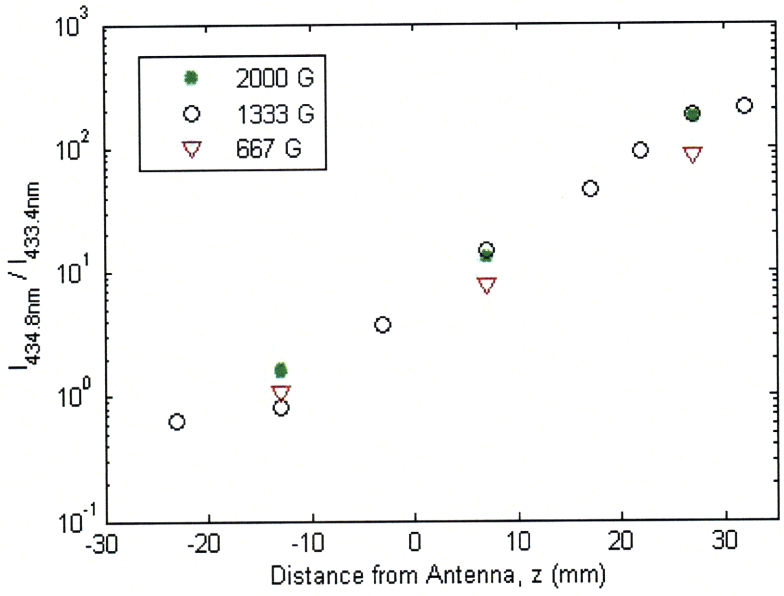

Figure 3-7: Ratio of Line Intensities at 434.8nm and 433.4nm Measured by a Radially Viewing Fiber vs. Fiber Distance from the Antenna for Three Values of Maximum Magnetic Field Strength, Operating at 770W and 0.475 mg/s

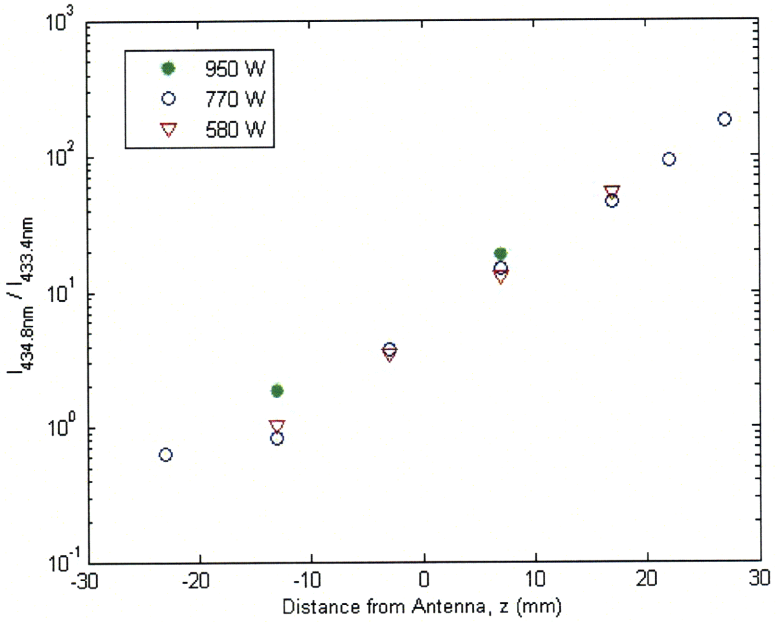

Figure 3-8: Ratio of Line Intensities at 434.8nm and 433.4nm Measured by a Radially Viewing Fiber vs. Fiber Distance from the Antenna for Three Values of Delivered RF Power, Operating at 1333 G and 0.475 mg/s of Argon

3.2 Axial Near-Plume Scans

The plume is mapped using simultaneous spectra from a radially viewing fiber (90^o from axis) and an angled fiber (58^o from axis) to resolve any Doppler shifts, as shown schematically in Figures 2-6 and 1-3. Each line in the 434.4nm centered spectra from the radial fiber is fitted with both a Gaussian and Lorentzian profile. The prominence of one distribution over the other in goodness of fit varies with each spectrum. The Gaussian distribution is expected to dominate in regions of high collisionality. A convolution of the two profiles may provide the best fit, as evidenced by Figure 3-9, but is not attempted here for simplicity.

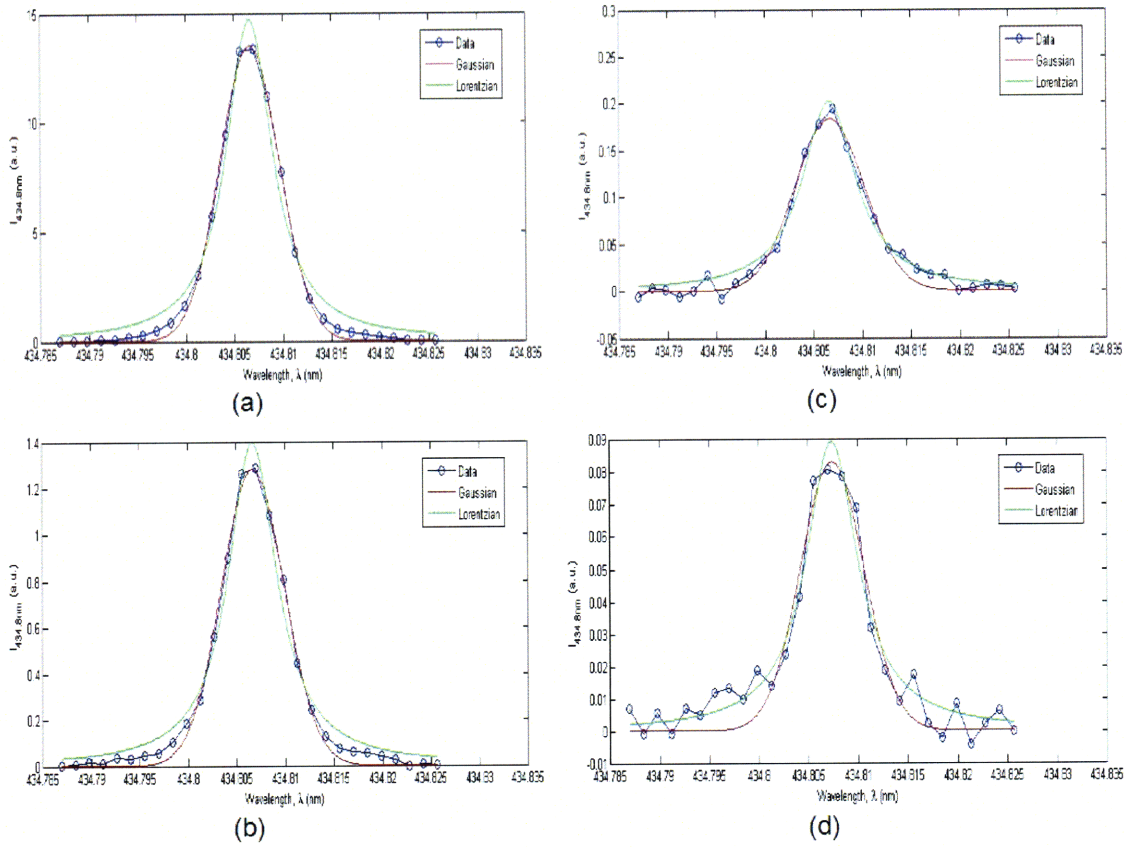

Figure 3-9: Emission Intensity of Ar I 433.4 nm Line vs. Wavelength at (a) 20mm (b) 50mm (c) 80mm (d) 110mm from Thruster Exit with Both Gaussian and Lorentzian Fits. Thruster Operating at 770W, 0.475 mg/s of Argon and 1333G

The width of the Ar I line at 433.4 nm corresponds to a temperature of 15000 K at the thruster exit, as shown in Figure 3-10, which is unphysically high, though

slightly less than observed in the ionization region (18500 K for the 433.4 nm line) with higher gas density and pressure. The inflated temperature is likely due to the instrument function of the spectroscopic apparatus being the dominant contributor to the line shape at such small widths (.06 Angstroms).

The majority of the neutral population at the exit should come from the wall recombination of ions flowing to containment surfaces or from unionized propellant gas. The neutral temperature should therefore largely reflect the temperature of the quartz tube. A more reasonable estimate of the neutral temperature at the exit is then 350 K (0.03 eV), corresponding to line width of 0.0011 nm, which is less than the inter-pixel bandwidth of the current study [53].

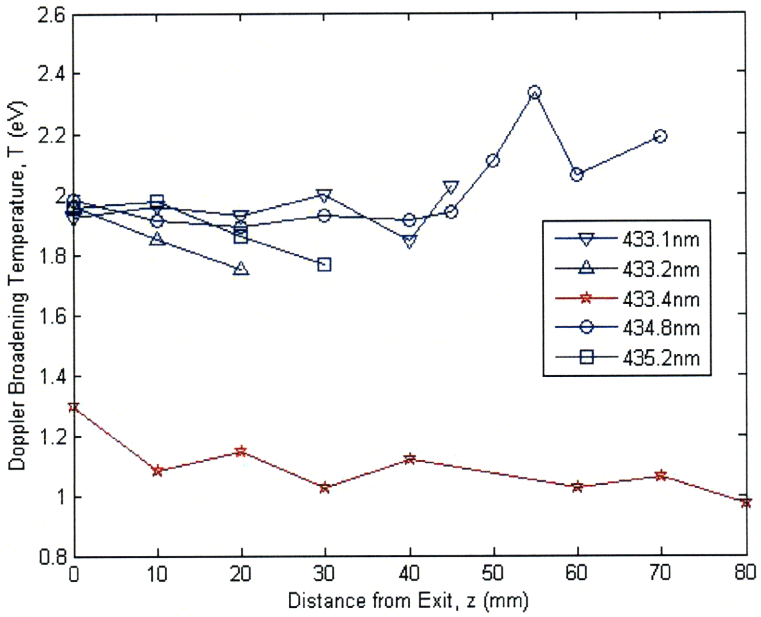

Figure 3-10: Doppler Broadening Temperature Corresponding to Line Width vs. Axial Distance from Thruster Exit. Operating at 770W, 0.475 mg/s of Argon and 1333G

Other broadening mechanisms include the Stark and pressure effects, which are small as $n_e \leq 2\text{x}10^{19}$ m^{-3} because of the acceleration in the expanding plume and P$\leq$ 10 mTorr. The natural line width, inferred by energy uncertainty, can be estimated by summing the decay rates from the states p and q involved in the transition as shown in Equation 3.4 [36]. The subscript k refers to any lower energy state, which

for the p level of the 433.4 nm Ar I line is only the ground state. The q level of the 433.4 nm line has three possible radiative decay times, leading to a natural linewidth of 0.05 pm which is negligible even at low temperatures.

$$\Delta\nu_N = \frac{1}{2\pi}[\Sigma A_{pk} + \Sigma A_{qk}] \tag{3.4}$$

Although the magnitude of the results is inaccurate, Figure 3-10 shows an ion temperature double that of the neutrals, which is a realistic result as they share similar heating mechanisms though ions have the added contribution of Coulomb interactions. The figure also indicates that both species are nearly isothermal over the axial region of interest.

One indicator of the electron temperature in the plasma is the ratio of emission intensities from the same species, under the assumptions of our simplified analysis in Section 1.3.1. All possible combinations of ion line ratios are shown in Figure 3-11 individually normalized to their maximum values. The overarching trend of the ion-to-ion line ratios is a decrease with distance from the exit, although in some cases this is very small ($< 10\%$).

Similar trends might be expected for the neutral-to-neutral Ar emission ratios, but as Figure 3-12 shows, no trend emerges at all. Taking ratios of neutral emission intensities is problematic, however, because only the dominant line at 433.4 nm maintains a high enough signal-to-noise ratio to yield an accurate representation of the intensity profile.

The ratios of the dominant Ar II lines (434.8 nm and 433.2 nm) to the dominant Ar I line (433.4nm) decrease nearly exponentially with distance from the thruster exit, as shown in Figure 3-13. The results of exponential fits to the data give characteristic scale lengths for decay between 16 and 19 mm. Lines from each species taken separately decay exponentially with distance over a length of 100 mm for Ar I and 15 mm for Ar II, as represented in Figure 3-14.

Any ion-to-neutral line intensity ratio should be largely proportional to the ionization fraction, as discussed in section 1.3.1. An ion line intensity itself should be

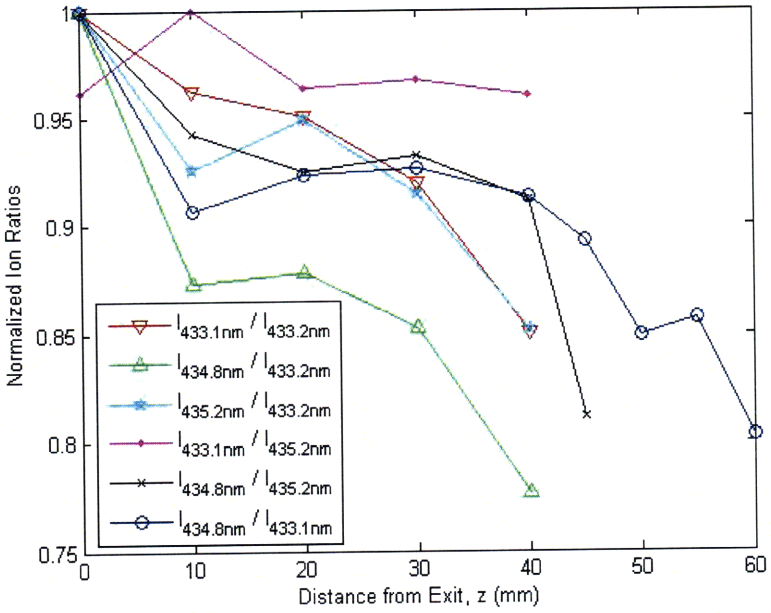

Figure 3-11: Ratio of Ion Line Intensities Measured by a Radially Viewing Fiber Normalized to Individual Maximums vs. Fiber Distance from Exit. Operating at 770W, 0.475 mg/s of Argon and 1333G

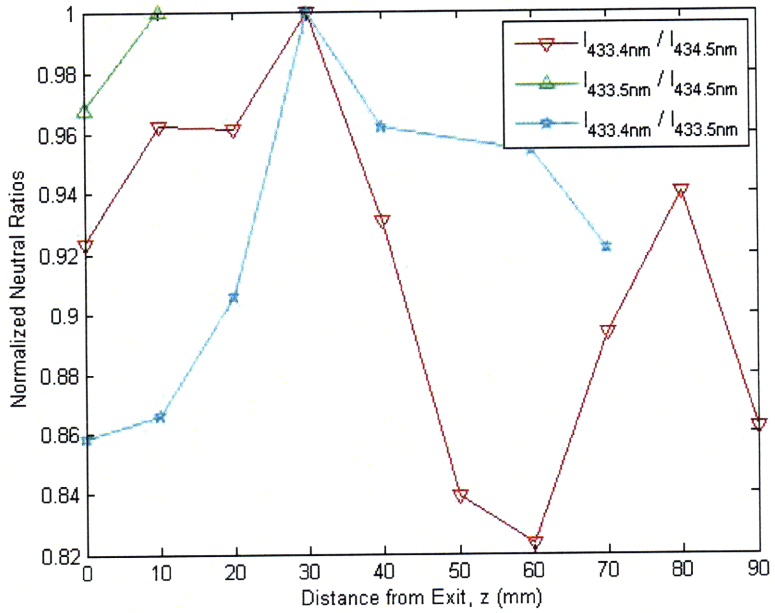

Figure 3-12: Ratio of Neutral Line Intensities Measured by a Radially Viewing Fiber Normalized to Individual Maximums vs. Fiber Distance from Exit. Operating at 770W, 0.475 mg/s of Argon and 1333G

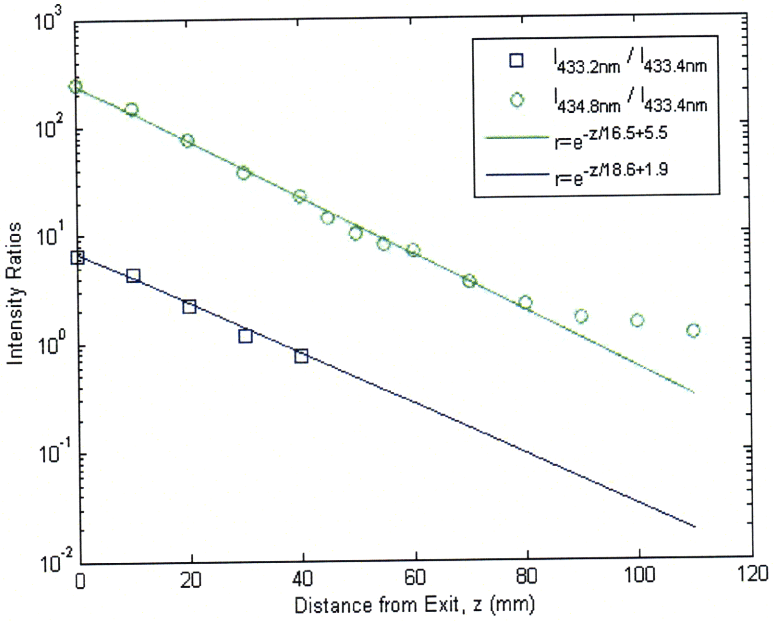

Figure 3-13: Ratio of Ar II to Ar I Line Intensities Measured by a Radially Viewing Fiber vs. Fiber Axial Distance from Thruster Exit. Operating at 770W, 0.475 mg/s of Argon and 1333G

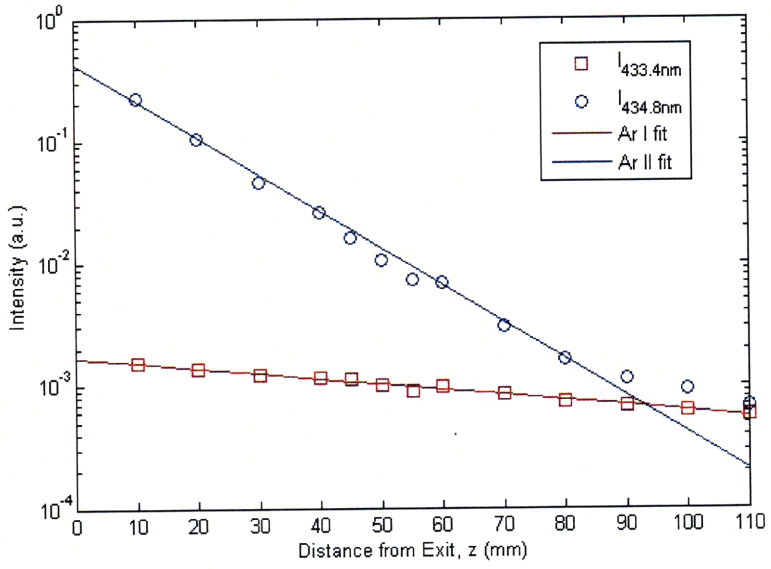

Figure 3-14: Ar II and Ar I Line Intensities Measured by a Radially Viewing Fiber vs. Fiber Axial Distance from Thruster Exit. Operating at 770W, 0.475 mg/s of Argon and 1333G

proportional to the plasma density squared, so a decay length of 15 mm for Ar II emission suggests a decay length of 30 mm for the plasma density, assuming isothermality of electrons. Any neutral line exhibits intensities proportional to the product of the plasma and neutral densities, which would require a growth in the neutral density over a scale length of 43 mm in order to account for a 100 mm decay length in intensity, as follows from Figure 3-14.

The upstream gas feedthrough used to calibrate mass flow rate with chamber pressure was also used to leak a known amount of Argon into the chamber in an attempt to quantify the chamber backpressure effect on the neutral density distribution. Without the addition of extraneous gas, the background pressure was a nearly constant P_{ch} of 4x10^{-5} Torr. This corresponds to $n_{ch} = \frac{N_A P_{ch}}{P_a t m v_{stp}} = \frac{6.2\times10^{23}4\times10^{-5}}{760\cdot.0224} = 1.4 \times 10^{12}$.

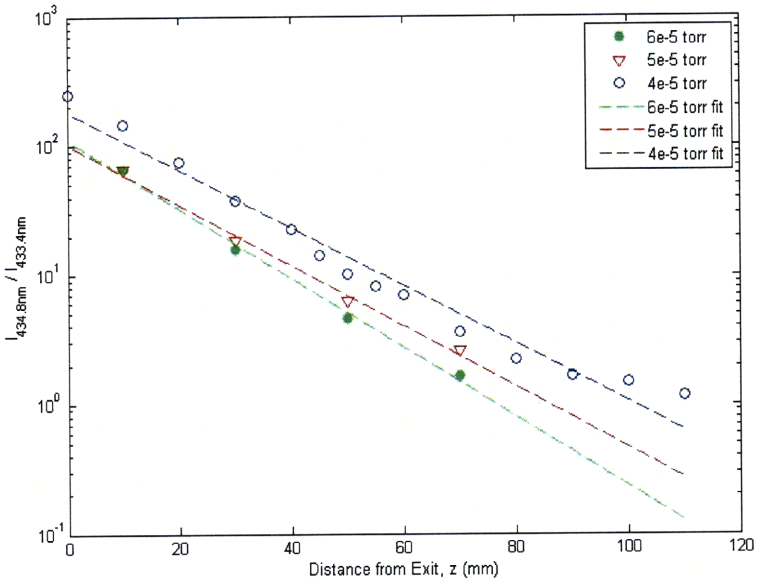

Figure 3-15: Ratio of Line Intensities at 434.8nm and 433.4nm Measured by a Radially Viewing Fiber vs. Fiber Axial Distance from Thruster Exit for Three Values of Chamber Pressure, Operating at 770W, 0.475 mg/s of Argon and 1333G

A constant flow of 5 sccm of Argon outside of the thruster increased the background pressure from the 4x10^{-5} Torr at normal operation to 5x10^{-5} Torr. The ratio of the 434.8nm Ar II line to the 433.4nm Ar I line is clearly reduced by the increase in background pressure. An exponential fit to the ratio has a characteristic decay length of 18 mm. The Ar I intensity decay length is 106 mm, suggesting neutral

density growth over a scale of 43 mm, as found with no auxiliary flow.

The chamber pressure settled at 60 μTorr with 10sccm of Ar leaked into the chamber. The increase in background pressure shortened the decay length of the ion-to-neutral emission intensity to 15 mm, while the neutral emission decay length rose to 114 mm, indicating a shorter neutral density growth length of 36 mm. A linear extrapolation of neutral emission decay length to a background of 10^{-12} torr yields a length of 72 mm, which still requires a growing neutral density far from the thruster exit.

Similar dependencies might be expected when the chamber pressure is increased by adding propellant flow to the thruster itself. A sub-nominal flow rate of 0.267 mg/s (9 sccm) produced an ion-to-neutral emission intensity ratio profile with a characteristic exponential decay length of 22 mm, well above the decay length estimated at nominal flow as expected. At a super-nominal flow rate of 0.683 mg/s (23 sccm), the decay length dropped to 16.5 mm. The results are shown graphically in Figure 3-16.

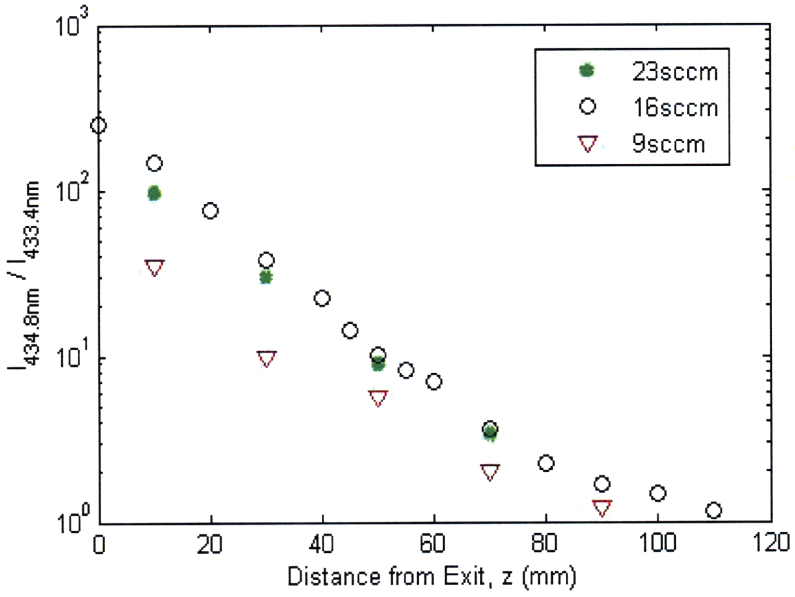

Figure 3-16: Ratio of Line Intensities at 434.8nm and 433.4nm Measured by a Radially Viewing Fiber vs. Fiber Axial Distance from Thruster Exit for Three Values of Argon Volumetric Flow Rate, Operating at 770W and 1333G

The ion-to-neutral emission ratio 10 mm from the exit quadruples when the flow rate increases from 9 to 16 sccm, then drops 40% when increased further from 16

to 23 sccm, suggesting an optimum exists between the two extremes. Ar I emission intensity decays over 70 mm for sub-nominal flow and 107 mm for super-nominal, indicating a much stronger dependency of decay length on flow moving from low flow rate to nominal than from nominal to high flow.

The magnetic field strength was shown to have an even larger effect on the emission characteristics. This fact is demonstrated by the ion-to-neutral emission ratio plotted in Figure 3-17 for three different maximum field strength values. The Ar II/Ar I ratio is 21 times larger when the field is doubled from 667 G to 1333 G, as measured 1 cm downstream of the axis, but only 32 times as large when tripled to 2000 G. On axis plasma density was noted to saturate in a similar manner at an applied field of around 800 G in Argon in a different Helicon experiment [35].

The field strength also has a drastic effect on the Ar I emission decay length which is as small as 36 mm for 667 G and as large as 320 mm for 2000 G. Continuing our simple proportionality analysis, the results indicate that while the decay length of the plasma density increases slightly with field strength from 29 to 33 mm, the more drastic effect is seen in the supposed neutral density growth length decrease from 160 to 36 mm.

The amount of RF power delivered to the plasma was varied from 580 to 950 W with comparatively little effect on the emission profiles, plotted in Figure 3-18. The Ar II/Ar I ratio more than doubles from 580 to 770 W, then is seen to drop by 14% upon increase to 950 W, as measured 10 mm from the exit. The plasma density decay length is 28 mm for both 580 and 950 W, but the neutral density length changes from 46 to 38 mm respectively. The results of the simple scaling analysis are summarized in Table 3.2, where λ_n is the growth length for neutral density and λ_i is the decay length of the plasma density.

The results from the power scan are counterintuitive, as an increase in power input to the plasma is not expected to result in a decrease in emission intensity, even across the small bandwidth studied here. The nominal and above nominal scans were performed on different days and the odd changes in emission intensity are posited as an artifact of changing optical properties of the apparatus over long enough time

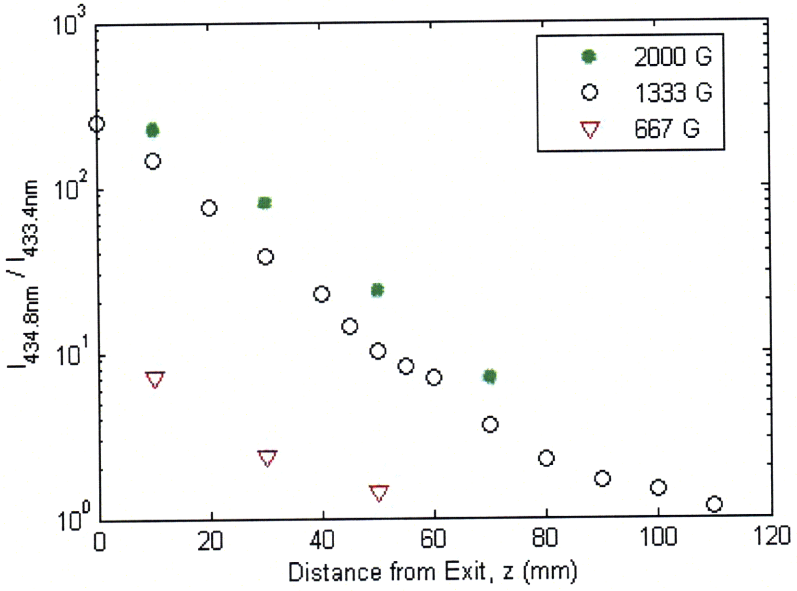

Figure 3-17: Ratio of Line Intensities at 434.8nm and 433.4nm Measured by a Radially Viewing Fiber vs. Fiber Distance from Thruster Exit for Three Values of Maximum Magnetic Field Strength, Operating at 770W and 0.475 mg/s of Argon

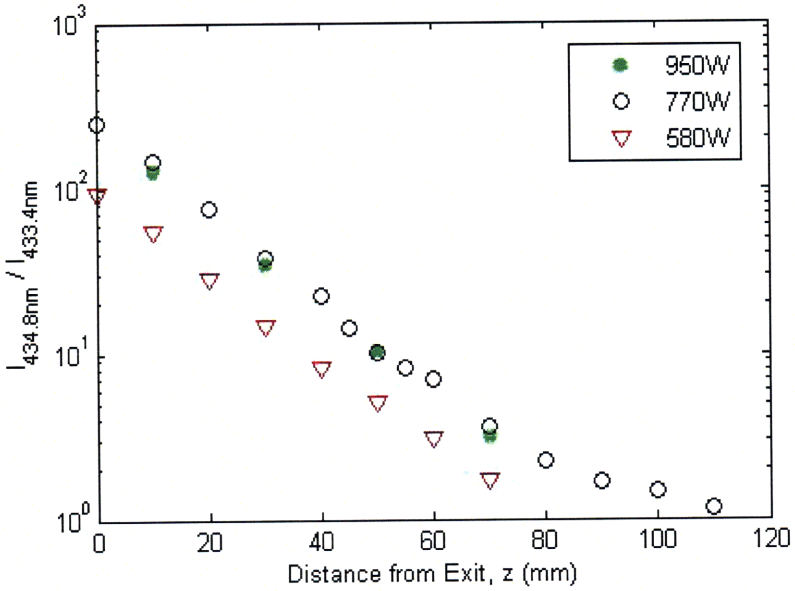

Figure 3-18: Ratio of Line Intensities at 434.8nm and 433.4nm Measured by a Radially Viewing Fiber vs. Fiber Distance from Thruster Exit for Three Values of Delivered RF Power, Operating at 1333 G and 0.475 mg/s of Argon

Condition	λ_n (mm)	λ_i (mm)
Nominal	+45	-31
9 sccm	+74	-36
23 sccm	+42	-30
+5 sccm	+44	-41
+10 sccm	+35	-27
667 G	+160	-29
2000 G	+36	-33
580 W	+46	-28
950 W	+38	-28

Table 3.2: Characteristic Length for Each Species at Different Conditions of Exponential (+) Growth or (-) Decay.

scales. A follow-on study was performed accordingly to determine the effects of RF power on emission by running immediately successive scans at a single axial location to minimize changes due to optical coating and positional hysteresis.

The results, obtained with the 1800 g/mm grating, reveal a much clearer dependency of emission properties on the RF power delivered to the plasma. Figure 3-19 shows the small but definite increase in ion line widths with power, while the neutral line width appears independent, with a standard deviation of 4% compared to 9-12% for the ions, which are all best fit by lines with slopes corresponding 0.1 eV per 100 W. The ion-to-neutral emission intensity ratios, plotted in a normalized form in Figure 3-20, exhibit a nearly linear dependence on power, increasing at a rate of 15% every 100 W until saturating above 980 W.

The decay lengths suggested by the application of the simplified rate equations to the measurements can be compared to equally rough estimations of the mean free paths in the plume under examination. First, estimates of the neutral and plasma densities can be made at the exit of the quartz confinement tube by assuming sonic conditions at this point and applying a utilization efficiency of η_u=0.90. The number density is found using the conservation of particles, as shown in Equation 3.5, where j indicates the species in question, $\dot{m}_i$ is just $\eta_u \dot{m}$, $\dot{m}_n$ is $(1-\eta_u)\dot{m}$, and c_s is the sound speed.

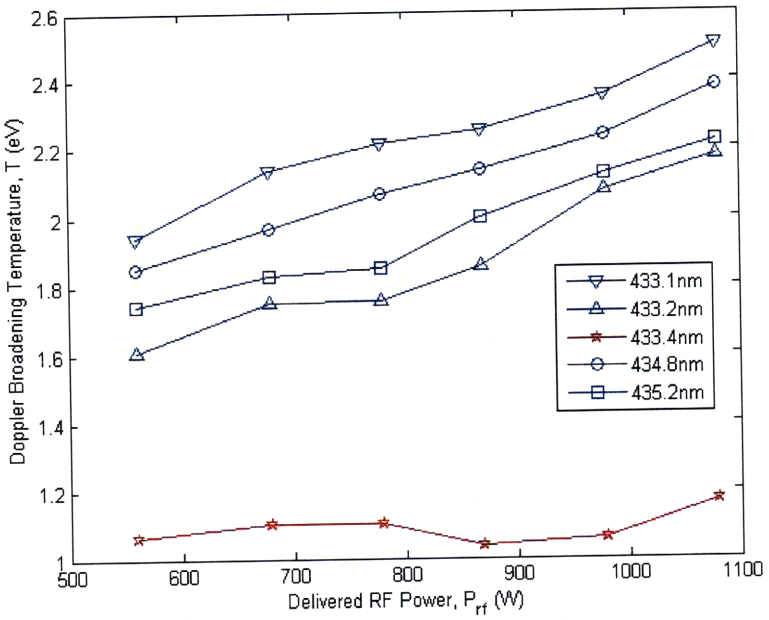

Figure 3-19: Doppler Broadening Temperature Corresponding to Line Width vs. Delivered RF Power Observed 5 mm from Thruster Exit. Operating at 0.475 mg/s of Argon and 1111 G

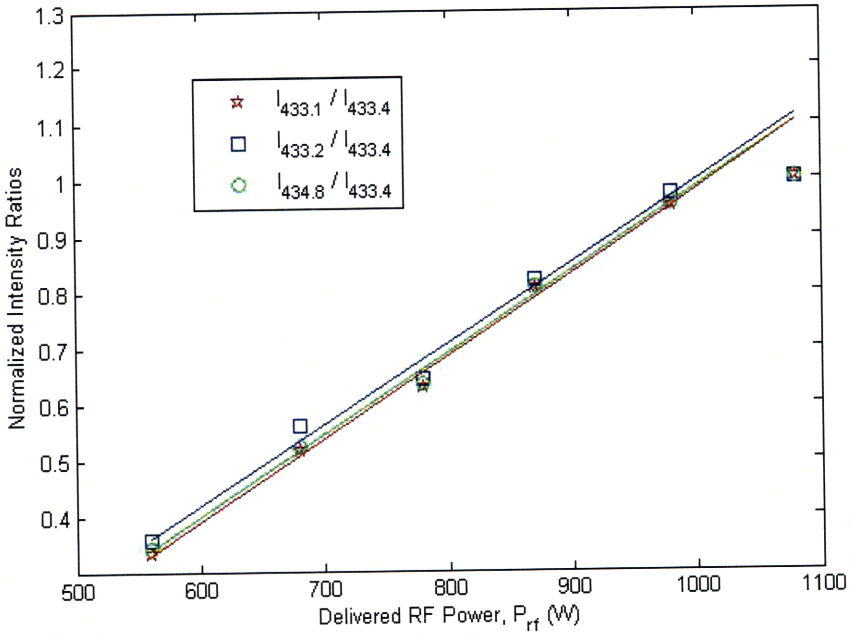

Figure 3-20: Normalized Ar II to Ar I Emission Ratios vs. Delivered RF Power Observed 5 mm from Thruster Exit. Operating at 0.475 mg/s of Argon and 1111 G

$$n_j = \frac{\dot{m}_j}{m\pi a^2 c_{s_j}} \tag{3.5}$$

The sound speed for neutral Argon is given by Equation 3.6, where γ for a monatomic gas is 5/3. Assuming a neutral gas temperature of 500 K as before, the sound speed is 415 m/s and the neutral density is 6.7x10^{18} m^{-3}.

$$c_{s_n} = \sqrt{\gamma R T_n} \tag{3.6}$$

The analogous condition for Argon ions is the ion acoustic speed given in Equation 1.18, where the electron temperature, kT_e, is assumed to be much greater than that of the ions. If the electron temperature is 5 eV, the ion acoustic speed is 3460 m/s and the plasma density is 7.3x10^{18} m^{-3} which is of the expected magnitude.

The dominant recombination mode for the plasma plume conditions studied here is generally three body recombination. The rate of electron catalyzed three body recombination can be calculated by finding the product of the square plasma density and the rate coefficient, $\alpha'(T_e)$, found in Equation 3.7 [41]. Dividing the ion sound speed by the rate of recombination allows comparison to characteristic lengths. For the order of 5 eV plasma assumed at the thruster exit the recombination length, $\lambda_{tbr} = \frac{1}{\alpha' n_e^2}$, is over 10^5 km and is clearly negligible. An electron temperature of $\leq$ 3100 K (0.27 eV) is necessary to obtain a recombination length less than 10 cm using this relation.

$$\alpha'(T_e) = 3.69 \cdot 10^{-44} \left(\frac{11.7}{T_e} + 2\right) exp\left(\frac{4.12}{T_e}\right) \quad (m^6/s) \tag{3.7}$$

$$\alpha'(T_e) = 1.09 \cdot 10^{-20} T_e^{-9/2} \quad (m^6/s) \tag{3.8}$$

An alternative three body recombination rate, shown in Equation 3.8 requires an electron temperature of 3640 K for a 10 cm electron catalyzed recombination length [21]. Electrons are the dominant third body for recombination collisions due to the efficient energy exchange in electron-electron collisions. In comparison electron-atom

collisions result in electrons losing only a fraction $2m_e/m_n$ ($2.7x10^{-5}$) of their energy on average. The mean free path for electrons thermalizing with neutrals is then almost one million kilometers.

The charge exchange (CEX) collision cross section can be calculated using Equation 3.9,

$$\sigma_{CEX}(E) = \left(7.49 \cdot 10^{-10} - 0.73 \cdot 10^{-10} ln(E)\right)^2 \ m^2 \tag{3.9}$$

where E is the energy of the Ar ion in eV [39]. An ion moving axially at the ion acoustic speed has a kinetic energy of 2.5 eV which results in a CEX cross section of $4.65x10^{-19}$ m^2, corresponding to a CEX mean free path, $\lambda_{CEX} = \frac{1}{n_n \sigma_{CEX}}$, of 32 cm. This mean free path is only a couple times larger than the region being studied spectroscopically. For comparison, taking the Argon atom radius as 71 pm, the hard sphere ion-neutral collision mean free path is over 4 m. The use of Equation 3.9 in estimating CEX cross sections shows little dependence on the energy of the ions since it is inside a logarithmic term so the mean free path will always be greater than 10 cm.

It is worth noting that errors in the measurement rise significantly as the emission intensity drops downstream of the thruster exit. The prominent ion line at 434.8 nm registers below 1% of the full scale of the collection device around 7 cm from the exit. The second brightest line, at 433.1 nm, is already below 1% of full scale at 4 cm downstream. This effect is readily observed in the uncertainty of intensity measurements, but it becomes harder to quantify when examining the Doppler shifts. The general trend is of increased uncertainty with distance from the thruster exit.

3.3 Doppler Shift Scans

The 58^o angled fiber is used to capture the Doppler shift of Ar II lines due to the axial velocity of ions in the plasma plume, with the radial fiber measurements as a benchmark. Ar I lines within the small bandwidth measured should show no shift in peak wavelength from 90^o to 58^o and are thus used to ensure proper wavelength

calibration between the two fibers. Typical shifts needed to match Ar I lines are less than 1.5 pm.

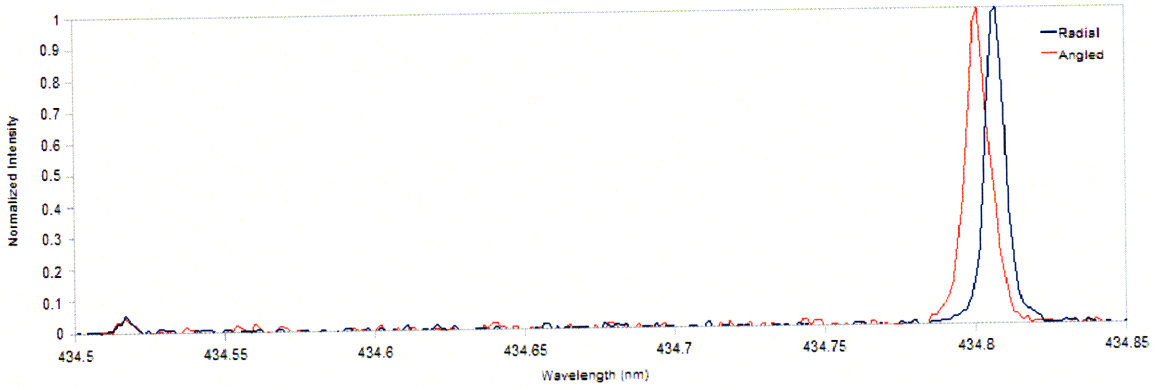

Figure 3-21: Emission Intensity vs. Wavelength Measured Radially and at a 58^o Angle 5 cm Downstream of Thruster Exit. Operating at 770W, 0.475 mg/s of Argon and 1333G

A representative spectra taken 5cm downstream of the exit is shown in Figure 3-21, where both an Ar I line and a Doppler shifted Ar II line are visible. Emission intensity is normalized for comparison between fibers due to differing transmissivities. The shift in the peak wavelength of the ion line at this particular distance is clear and corresponds to a velocity of 4340 m/s along the line-of-sight of the fiber.

Spectra taken closer than 3 cm from the thruster exit display a more ambiguous shift. The peak wavelength is apparently shifted by less than one pixel with a broadened shape on the blue side of the peak. These measurements are taken close enough to collect spurious light reflected from the metal face of the magnet or the interior of the magnet bore, which may be obscuring the results here.

A clearly blue-shifted peak dominates spectra taken from 3 to 6 cm downstream of the exit. The ion line shifts to continually shorter wavelengths as the angled fiber is moved further downstream. The continued shift in this range, displayed in Figure 3-22, indicates ion acceleration substantially downstream of the exit of the thruster.

At and beyond 7cm downstream of the exit a minorly blue-shifted peak emerges with a peak wavelength near that measured by the radially viewing fiber. As Ar II emission decreases towards the background noise level, the secondary peak begins to dominate the Doppler-shifted line. The nearly stationary peak is likely due to the

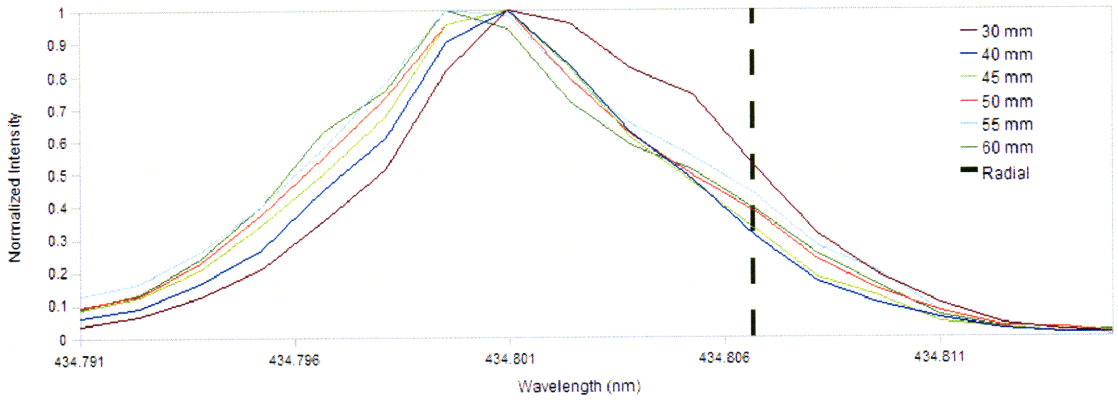

Figure 3-22: Emission Intensity vs. Wavelength Measured at a 58^o Angle for Various Distances Downstream of Thruster Exit. Operating at 770W, 0.475 mg/s of Argon and 1333G

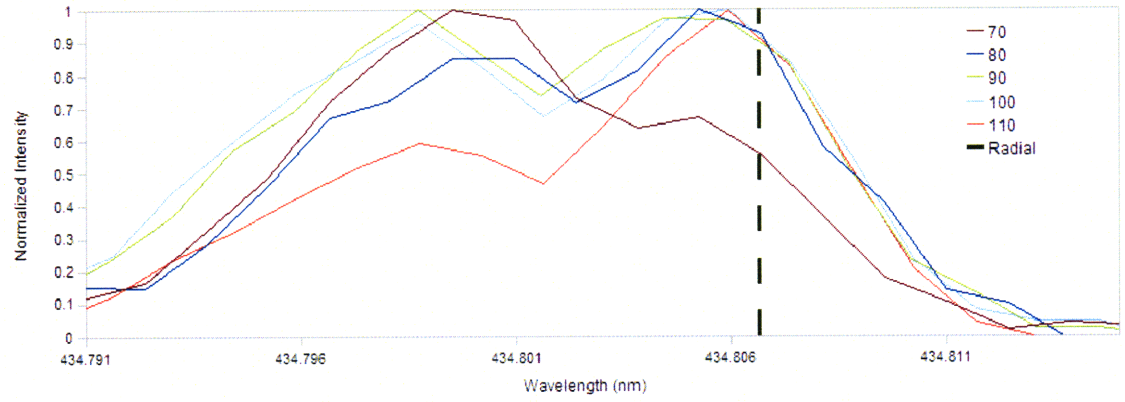

Figure 3-23: Emission Intensity vs. Wavelength Measured at a 58^o Angle for Various Distances Downstream of Thruster Exit Exhibiting CEX Peaks. Operating at 770W, 0.475 mg/s of Argon and 1333G

predominance of CEX ions, which no longer have the directed velocity of the bulk ions, at these distances. Spectra exhibiting the CEX peak are shown in Figure 3-23.

Each of the three line shape types are shown concurrently in Figure 3-24, normalized to the maximum intensity of each line. The close overlap of the profile at 1 cm with the CEX peak at 9 cm suggests similar processes are responsible. The raw line shapes from 1 to 8 cm downstream are shown on a logarithmic scale in Figure 3-25.

The CEX peak in Figure 3-25 appears to effect the line shapes at all axial locations. A large drop in the CEX emission intensity is seen between 1 and 4 cm, while there is very little decrease in intensity from 4 to 8 cm. The fast peak, on the other hand, exhibits a smaller proportional drop between 1 and 4 cm and a much larger drop between 4 and 8 cm. While the larger drop in CEX intensity closer to the exit may be due to reflection effects and the overlap of the two peaks, the disparity in decay of the fast peak and slow peak at larger axial distances is likely due to the drop in fast ion density predicted in Section 1.2.2 as jet expands and accelerates. The CEX population should also undergo acceleration and rarefication by the ambipolar field but the continuity equation in this case also includes a source term due to continual CEX collisions which, coupled with the increase in neutral density indicated in Section 3.2, may lead to the slow decay observed far from the exit.

The velocity of the Doppler shifted peak along the line of sight was estimated for each spectrum acquired by fitting each 434.8 nm line profile with the summation of two idealized profiles, one for the CEX population and one for the main population of flowing ions. At first Gaussian profiles were fit to each population, but a lower residual norm was obtained by fitting a Gaussian to the CEX ions and a Lorentzian to the main flow. The results for several representative axial positions can be seen along with their respective radial line profiles in Figure 3-26.

An axially resolved picture of the main velocity component along the line of sight is then calculated using Equation 1.29, where the wavelength shift is taken from the peak of the Lorentzian or Gaussian fits to the NIST tabulated wavelength of 434.8064 nm. The resulting v_{dop} for the CEX and main populations are given in Figure 3-27 for the Gaussian plus Lorentzian fits along with the double Gaussian fits. It is worth

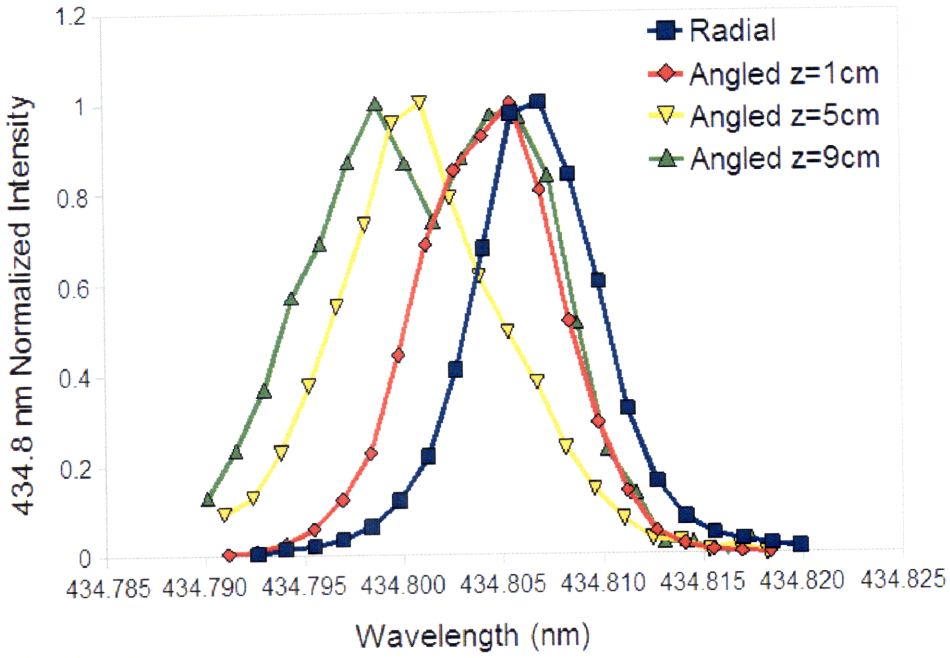

Figure 3-24: Normalized Emission Intensity vs. Wavelength for Various Distances from Exit Collected at a 58^o Angle from Thruster Axis for Doppler Shift Examination. Operating at 770W, 0.475 mg/s of Argon and 1333G

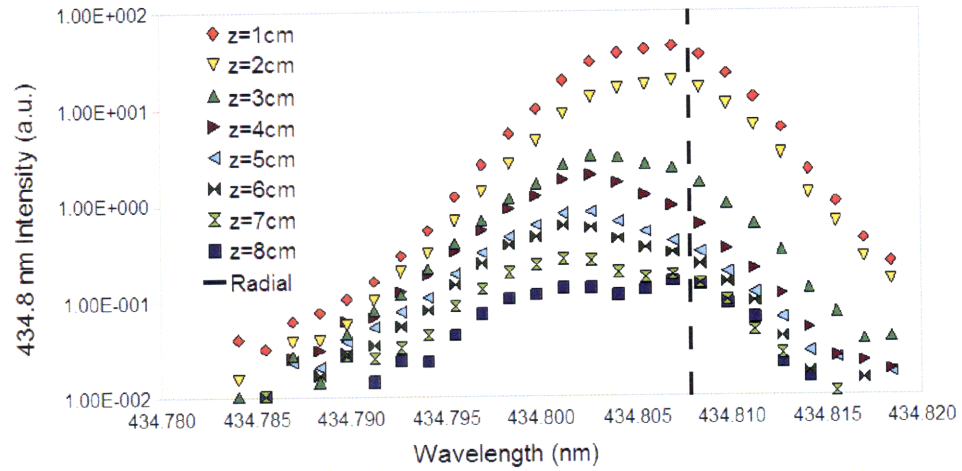

Figure 3-25: Emission Intensity vs. Wavelength for Various Distances from Exit Collected at a 58^o Angle from Thruster Axis for Doppler Shift Examination. The Peak Wavelength Measured by Radial Fibers is Denoted by Dashed Line. Operating at 770W, 0.475 mg/s of Argon and 1333G

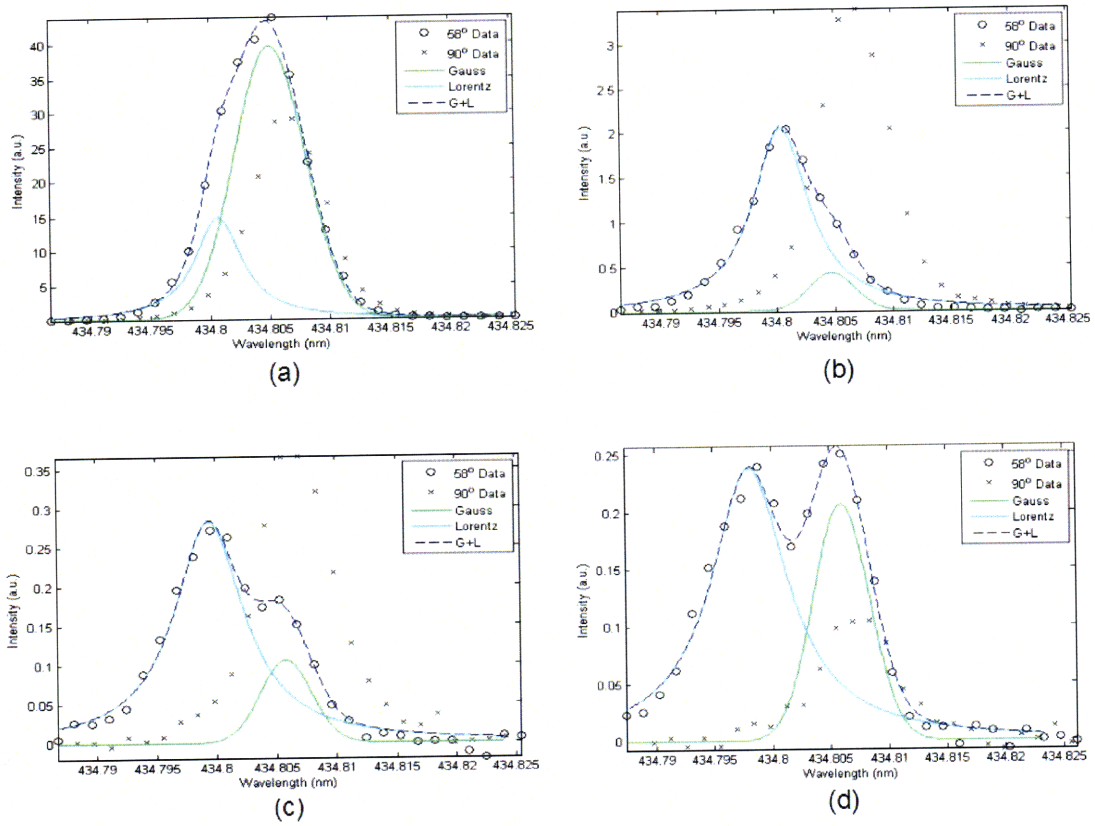

Figure 3-26: 434.8 nm Line Profiles at 90° and 58° Fit by the Summation of a Gaussian and a Lorentzian vs. Distance from the Thruster Exit Plane, Operating at 770W, 0.475 mg/s of Argon and 1333G at an Axial Distance of (a) 10mm (b) 40mm (c) 70mm and (d) 100mm from the Thruster Exit

noting that the CEX peak velocity is roughly invariant with distance, a behavior it would not exhibit if it were caused instead by the projection of a divergent main velocity vector on the far side of the thruster axis.

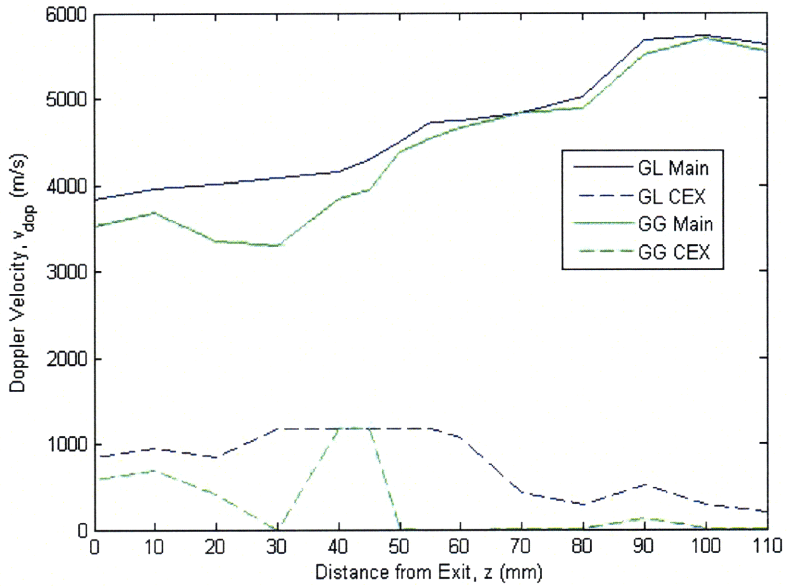

Figure 3-27: Doppler Shifted Peak Velocity 58^o From Thruster Axis Calculated Using Two Different Line Fitting Methods vs. Distance from the Thruster Exit Plane. Operating at 770W, 0.475 mg/s of Argon and 1333G

The Doppler velocity is then 5626 m/s at a distance of 11 cm from the exit. If the velocity of the radiating atoms is assumed to be dominated by the purely axially moving ions at the center of the plume, the axial velocity is then 10616 m/s for an I_{sp} of 1082 seconds. We will work under the assumption that the Doppler velocity is simply the projection of the velocity of the axially moving main population for the remainder of the study unless otherwise noted. It is a useful simplification for comparison with theory and for estimation of the upper bounds of thruster performance.

The location of peak emission intensity is at most uncertain to within one half the inter-pixel wavelength, post wavelength calibration, corresponding to a highly conservative Doppler velocity uncertainty of about 500 m/s. The lower bound of the estimated CEX velocity at the exit is then on the order of the predicted neutral sound speed at a gas temperature 500 K.

Mass Flow Rate Scans

The results from the 58^o angled fiber vary significantly with the propellant mass flow rate. Two highly Doppler shifted peaks appear at most axial locations for all mass flow rates. In some cases the peaks are sharp indicating a large population at velocity distinct from the remainder of the ions, while in others the peaks are apparently spread thin over a large range of velocities, possibly due to flow diverging from the centerline.

At the highest flow rate tested of 0.683 mg/s (23 sccm of Argon) the slower peak dominates 3 cm downstream, but is almost superseded by the faster peak at 7 cm downstream. Both peaks appear to blue shift slightly with increased axial distance, but all shifts are within one pixel or equivalently a roughly 1 km/s Doppler shift. The two peaks correspond to velocities of around 3100 m/s and 5400 m/s. Assuming these peaks can be attributed to divergent ions near the core of the plume moving at the same speed on different sides of the thruster axis, the velocity is nearly constant at 8.1 km/s firing 9.6^o from the central axis.

While the explanation that the far blue shifted peak is the $v*cos(58^o-\theta)$ projection and the less blue shifted peak is the $v * cos(58^o + \theta)$ projection provides a simple reasoning for the location of the two peaks it offers no explanation of the monotonic change in their relative intensities, illustrated in Figure 3-28.

The plume scan at a flow rate of 0.267 mg/s (9 sccm of Argon) results in a 434.8 nm line profile with three apparent peaks, as displayed in Figure 3-29, one of which is nearly stationary and assumed due to CEX ions. The irregular line shapes, shown in Figure 3-29, complicate the Gaussian and Lorentzian fitting procedure utilized for the nominal flow data, but one can pick out locations where the normal profile appears disrupted by an overlapping peak to estimate velocities of apparent populations. Application of the diverging velocity vectors assumption yields a nearly constant 12^o firing angle (excluding the relatively smooth profile at 1 cm, which yielded 14^o), though the relative intensities of the peaks once again fail to follow a consistent pattern.

Figure 3-30 traces the inferred peak locations used to estimate Doppler velocities

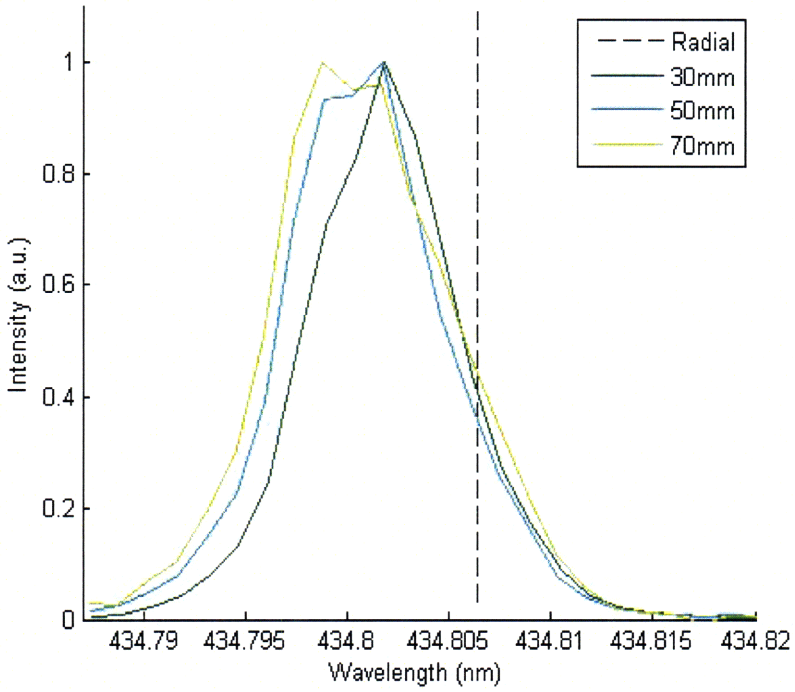

Figure 3-28: Normalized Emission Intensity vs. Wavelength for Various Distances from Exit Collected at a 58^o Angle from Thruster Axis. Operating at 770W, 1333G and 0.683 mg/s of Argon

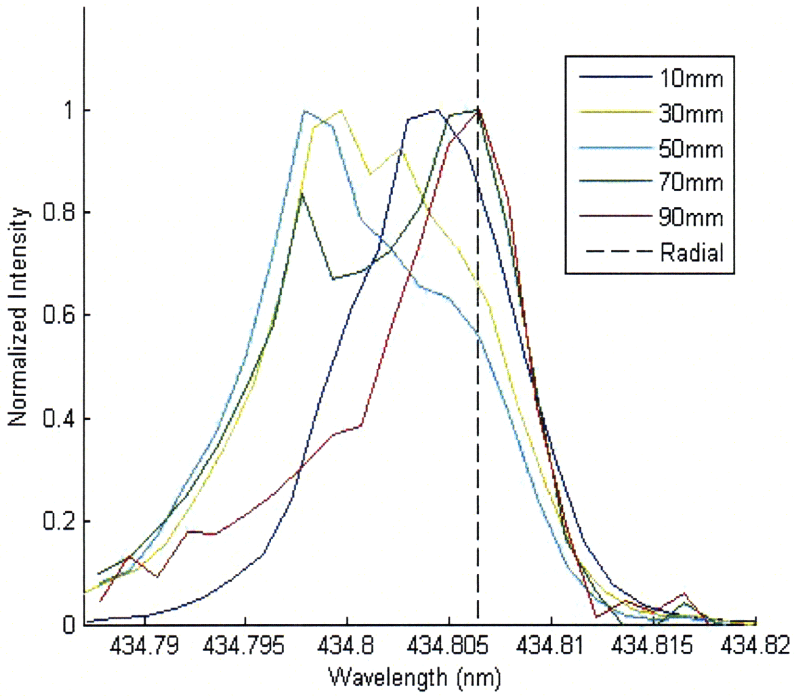

Figure 3-29: Normalized Emission Intensity vs. Wavelength for Various Distances from Exit Collected at a 58^o Angle from Thruster Axis. Operating at 770W, 1333G and 0.267 mg/s of Argon

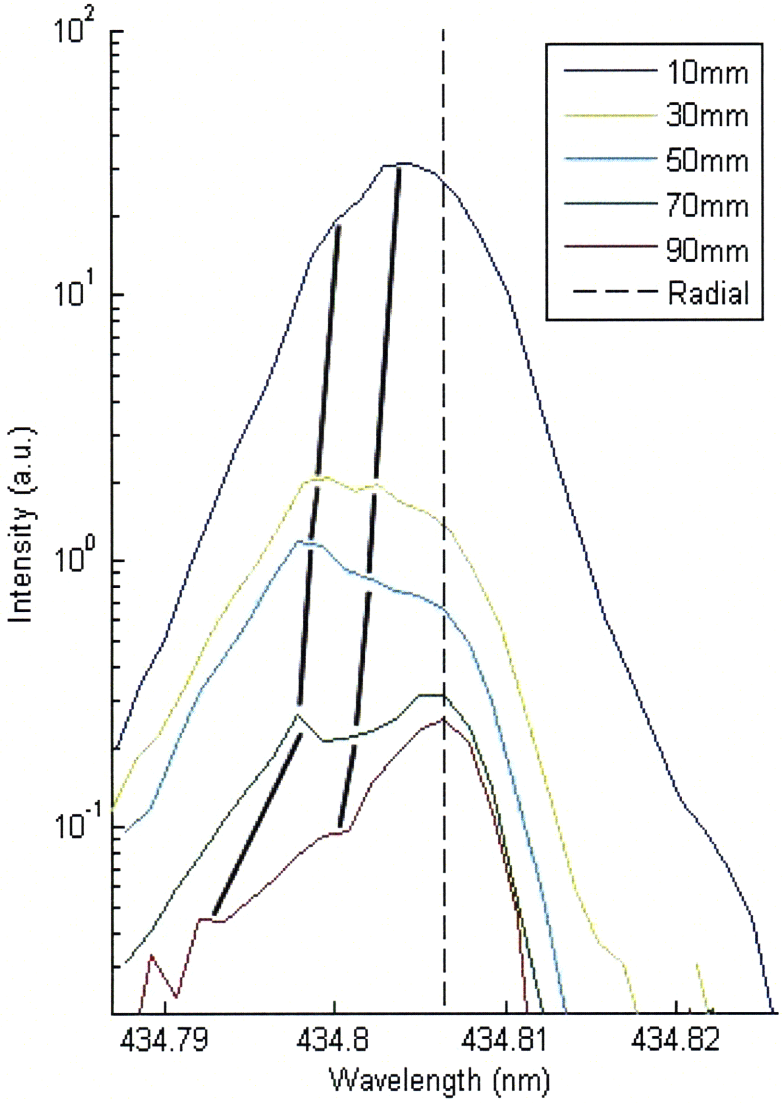

Figure 3-30: Emission Intensity Near 434.8 nm vs. Wavelength for Various Distances from Exit Collected at a 58^o Angle from Thruster Axis with Trace of Inferred Peak Locations. Operating at 770W, 1333G and 0.267 mg/s of Argon

from 434.8 nm line irregularities, leading to the range of velocities plotted in Figure 3-31, which shows similar acceleration in the Doppler velocities for both peaks at 0.267 mg/s. The difference in velocities between the two peaks increases by only 20% from 1 cm to 5 cm, but doubles from 1 cm to 9 cm, dispelling the hypothesis that one population was accelerated by some upstream mechanism to which the second population was not exposed.

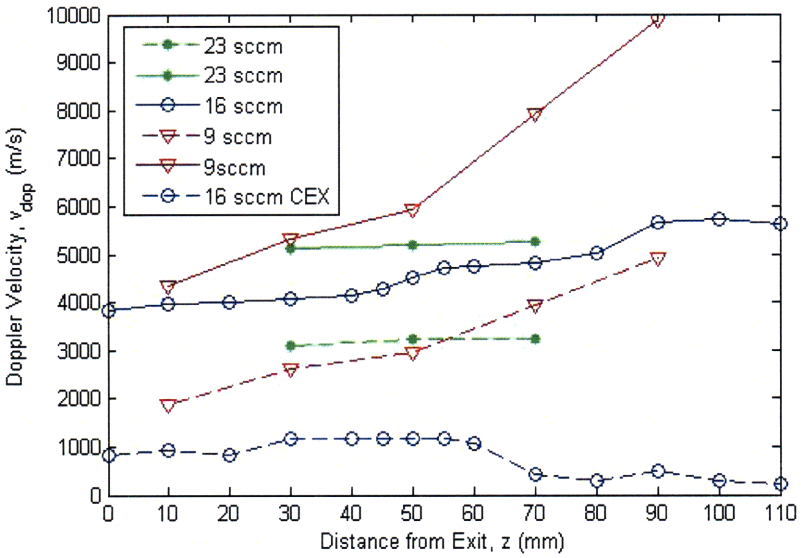

Figure 3-31: Doppler Velocity vs. Distance from Thruster Exit for Various Mass Flow Rates of Argon. Operating at 770W and 1333G

Figure 3-32 gives the axial velocities obtained with off-nominal flow rates using the angled velocity vector assumption. The plot gives the expected result of increased axial flow speed with decreasing flow rate, which was found independently using a retarding potential analyzer to measure the ion energy distribution [48].

In general both the angled and radial profiles get broader and less intense as the flow rate is decreased, though the effect is less noticeable at points further downstream. Oddly, the radially measured intensity is higher at 0.475 mg/s than at 0.683 mg/s, while the low flow rate intensity is significantly lower than both. The intensities observed by the angled fiber are comparable for low and nominal flow, which both register much lower than the high flow case.

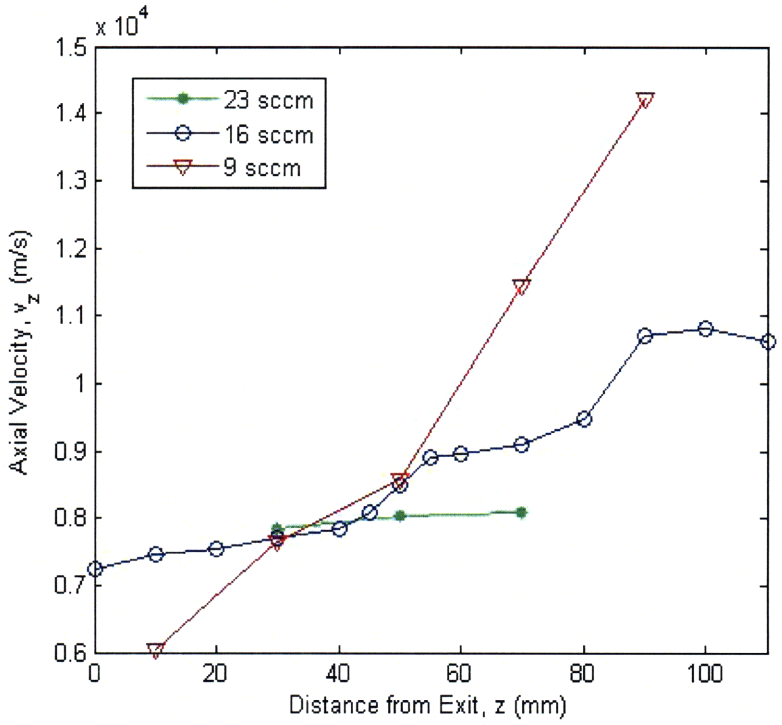

Figure 3-32: Axial Velocity vs. Distance from Thruster Exit for Various Mass Flow Rates of Argon. Operating at 770W and 1333G

Field Strength Scan

Angled fiber measurements of the thruster running at two off-nominal magnetic field strengths showed the strong dependence of the 434.8 nm line shape on field topology. The resulting line shapes can all be seen normalized to maximum intensity in Figure 3-33.

The full field strength case (2000 G) exhibits one consistently doppler shifted peak, with the appearance of a CEX peak at 7 cm from the exit. The 434.8 nm line at full field is consistently further blue shifted than the nominal case and has relatively smaller secondary peaks which matches visual observations of increased plume collimation in the region of interest.

At 10 mm the main peak shift corresponds to a Doppler velocity of 1470 m/s, but the asymmetry of the line matches that found in the nominal case shown in Figure 3-26(a), and the same fitting technique yields a Doppler velocity of 4660 m/s. The difference between main peak shift and the faster Lorentzian fit peak shift is 3000

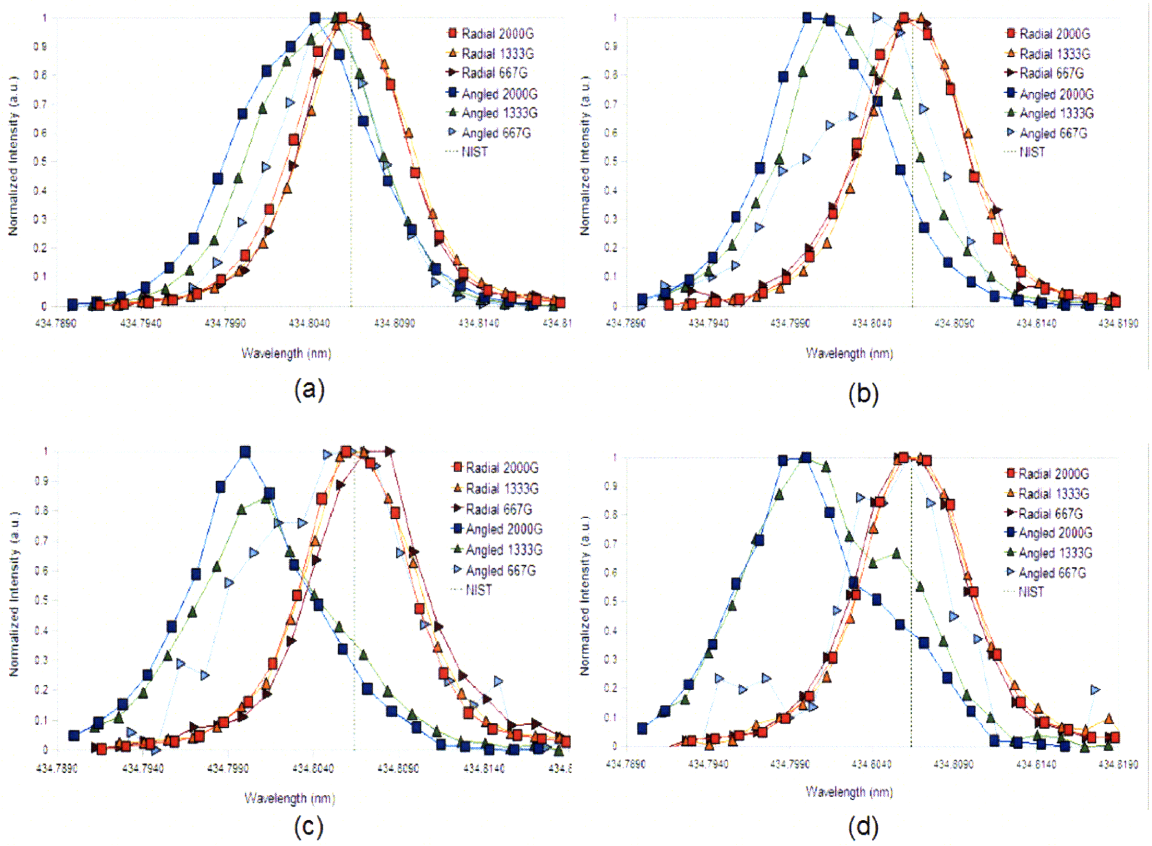

Figure 3-33: Normalized Emission Intensity vs. Wavelength for (a) 10mm (b) 30mm (c) 50mm (d) 70mm from Exit Collected Radially and at a 58^o Angle from Thruster Axis for Doppler Shift Examination. Operating at 770W, 0.475 mg/s and Various Field Strengths

m/s in both nominal and high field cases.

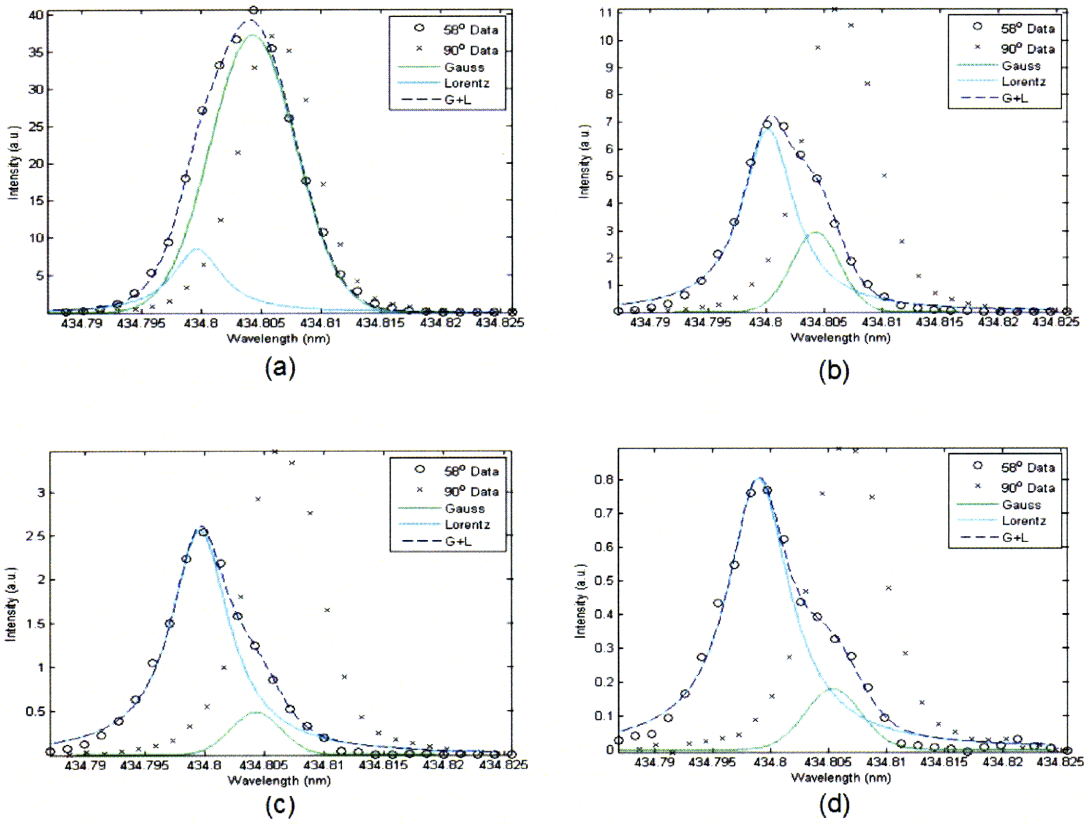

Figure 3-34: 434.8 nm Line Profiles at 90° and 58° Fit by the Summation of a Gaussian and a Lorentzian vs. Distance from the Thruster Exit Plane, Operating at 770W, 0.475 mg/s of Argon and 2000G at an Axial Distance of (a) 10mm (b) 30mm (c) 50mm and (d) 70mm from the Thruster Exit

The high field profiles are amenable to the same two-peak fitting used for nominal flow, resulting in the well matched shapes of Figure 3-34. The velocities implicated by the fitting procedure, in Figure 3-35, are very similar to those found with the nominal field, though slightly elevated. Subtracting the so-called CEX velocity from the main population velocity and assuming a purely axial flow for both conditions shows, in Figure 3-36, essentially no difference from 1333 to 2000 G.

The low field strength spectra appear always dominated by the near stationary peak, hypothesized to be due to charge exchange processes. The plume becomes so diffuse and the emission intensity so low at such low field strengths that the profiles appear too noisy to extract any useful Doppler shift data.

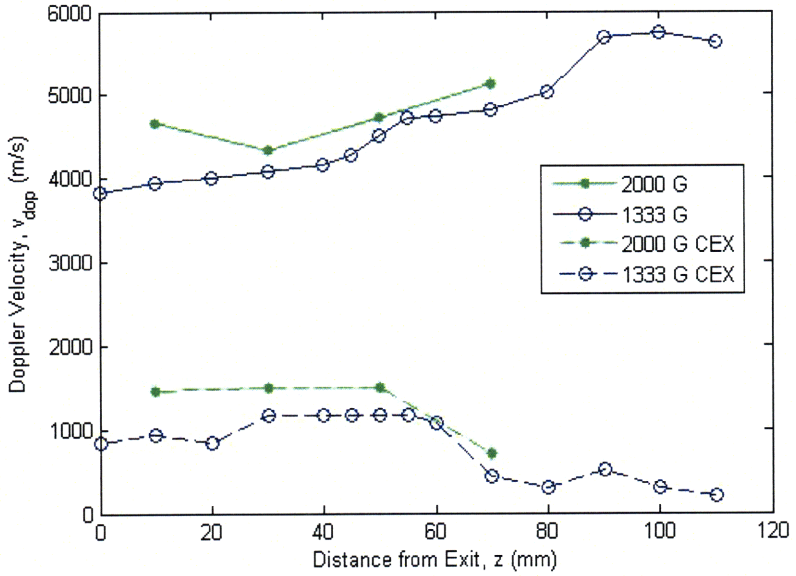

Figure 3-35: Doppler Velocity vs. Distance from Thruster Exit for Various Magnetic Field Strengths. Operating at 770W and 0.475 mg/s of Argon

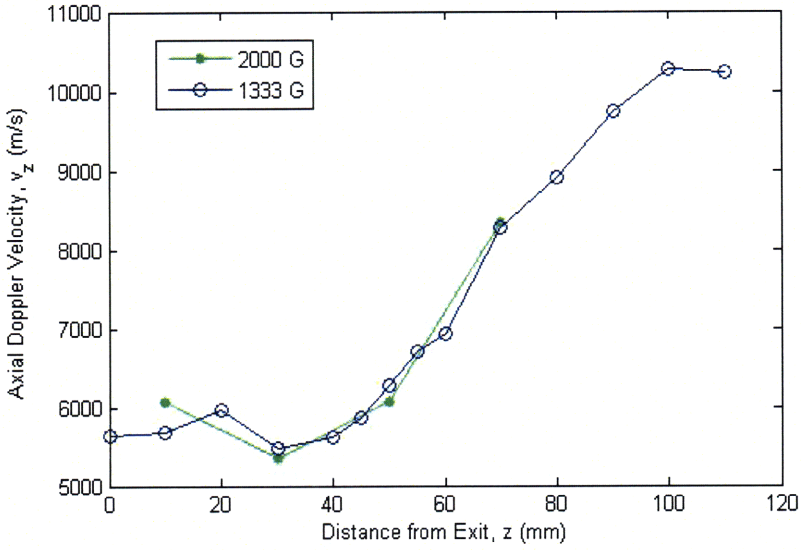

Figure 3-36: Axial Doppler Velocity Difference Between Main and CEX Populations vs. Distance from Thruster Exit for Various Magnetic Field Strengths. Operating at 770W and 0.475 mg/s of Argon

RF Power Scan

The two axial scans at off-nominal power provided starkly different results. The Doppler shifted 434.8 nm line shapes are presented for all power levels in Figure 3-37 at several representative axial positions.

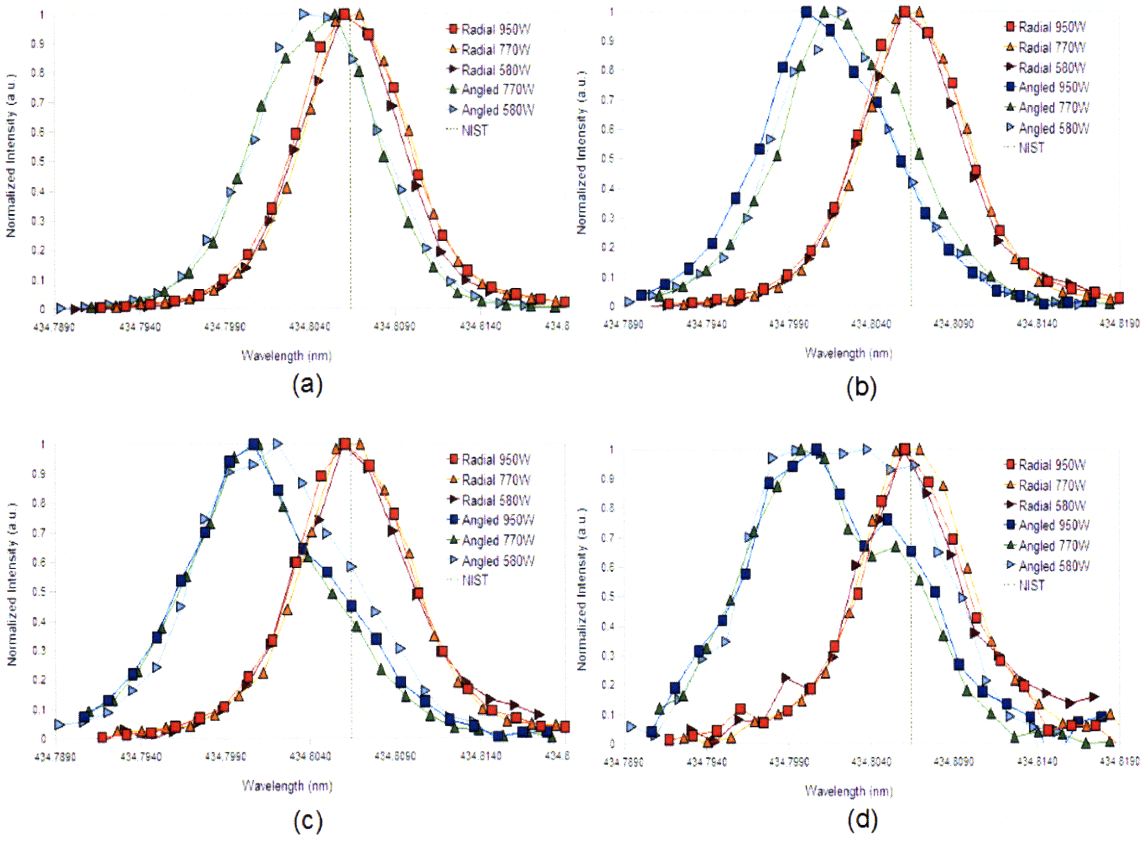

Figure 3-37: Normalized Emission Intensity vs. Wavelength for (a) 10mm (b) 30mm (c) 50mm (d) 70mm from Exit Collected Radially and at a 58^o Angle from Thruster Axis for Doppler Shift Examination. Operating at 1333 G, 0.475 mg/s and Various Values of Delivered RF Power

The changes in line shapes from 770 W to 950 W are the slightest seen in any off-nominal spectra, the main difference being a single pixel further blue shift for the high power line at 30 mm. The only other noticeable difference is a slight higher relative contribution from the CEX peak in the high power spectra.

The low power spectra, on the other hand, are markedly different in shape. Figure 3-38 gives a semilog view of the evolution of line shapes at low power, which show a

fairly constant form when taken less than 6 cm from the exit. By 6 cm the peak is completely shifted by around 5 km/s with a strong asymmetric broadening towards higher frequencies. At 7 cm the peak is broad and nearly flat from 434.8067 to 434.7980 nm, a shape not like any seen at the other conditions. The mechanism behind the broad peak is unclear, but it suggests a spread in velocity components along the viewing angle from 0 to 5.8 km/s that is in no way reflected in the shape of the 434.8 nm line measured by the radial fiber.

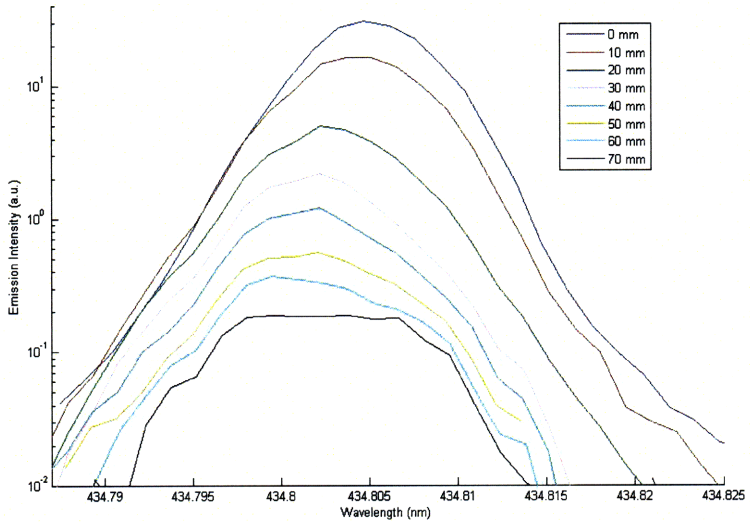

Figure 3-38: Emission Intensity vs. Wavelength for Various Distances from Exit Collected at a 58^{o} Angle from Thruster Axis. Operating at 1333 G, 0.475 mg/s and 580 W

The same fitting algorithm used for the nominal profiles can be used to extract velocity data from the two off-nominal power scans. It is notable that the results of the fitting algorithm are somewhat dependent on the allowed location of the Gaussian fit intended to capture CEX populations.

Allowing the Gaussian fit to be centered at any frequency lower than the center frequency of the Lorentzian fit produces the two-population Doppler velocities shown in Figure 3-39. When the Gaussian peak is constrained to within 1.5 pixels of the NIST tabulated wavelength the velocities shown in Figure 3-40 result.

If the Gaussian peak is truly representing a slow moving CEX population the constrained results should prove more reliable. The slip velocity between the two

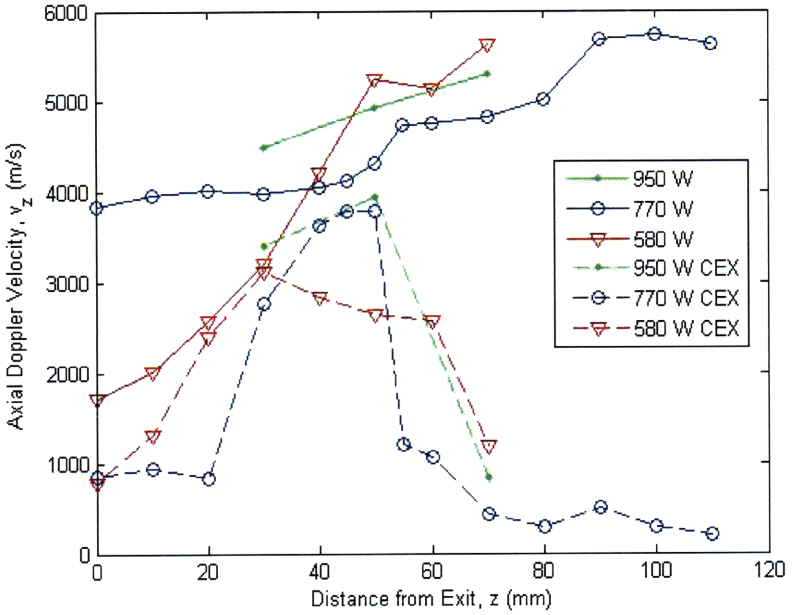

Figure 3-39: Doppler Velocity vs. Distance from Thruster Exit for Various Values of Delivered RF Power for an Unrestrained CEX Velocity. Operating at 1333 G and 0.475 mg/s of Argon

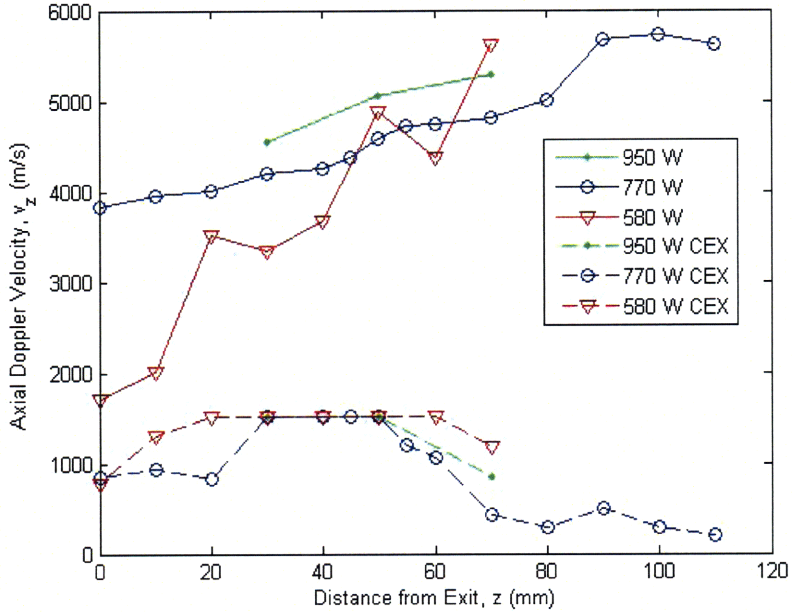

Figure 3-40: Doppler Velocity vs. Distance from Thruster Exit for Various Values of Delivered RF Power for a Constrained CEX Velocity. Operating at 1333 G and 0.475 mg/s of Argon

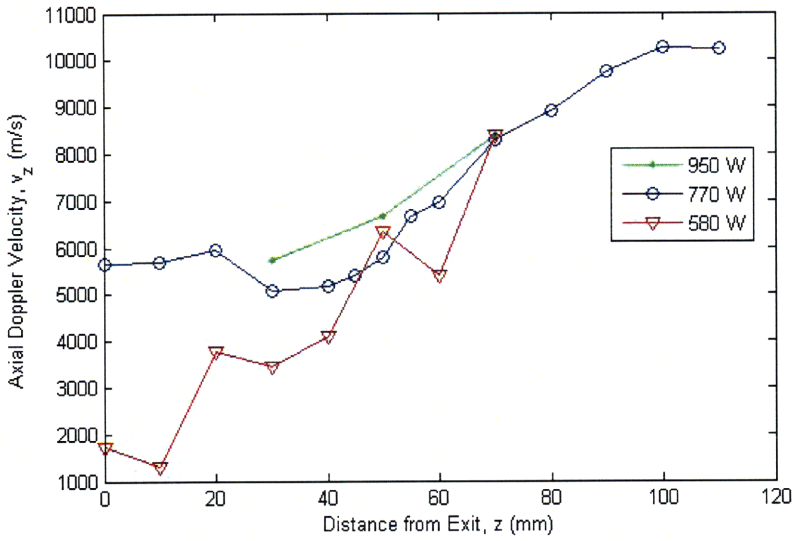

Figure 3-41: Axial Doppler Velocity Difference Between Main and CEX Populations vs. Distance from Thruster Exit for Various Values of Delivered RF Power for a Constrained CEX Velocity. Operating at 1333 G and 0.475 mg/s of Argon

populations is plotted in Figure 3-41 assuming axially directed flow for both, for comparison with the magnetic field strength scan results. While changes in the velocity distributions with delivered RF power are suggested by the changes in line shapes, most changes to the dominant Doppler velocity are within our conservative uncertainty estimates.

3.3.1 Comparison to Semi-Empirical Model

The strong electron pressure gradient indicated by the axial plume scan is hypothesized as the main source of acceleration.

The strong electron pressure gradient indicated by the axial plume scan is hypothesized as the main source of acceleration as discussed in the introductory sections. The ion momentum equation found in Section 1.2.2 can be recast as Equation 3.10 and a solved with the model of $n_e(z)$ indicated by the radial plume emission study, as given in Equation 3.11, where λ_i is the characteristic ion density decay length in meters.

$$m_i n_e \frac{\partial\left(v_i^2\right)}{\partial z} = 2\frac{\partial\left(n_e k T_e\right)}{\partial z} - m_i n_e n_n \sigma_{in} v_i^2 \tag{3.10}$$

$$n_e(z) = n_{e_0} e^{-\frac{z}{\lambda_i}} \tag{3.11}$$

$$v_i^2 = e^{-n_n \sigma_{in} z + C} + \frac{2kT_e}{n_n \sigma_{in} m_i \lambda_i} \tag{3.12}$$

Solving the differential equation is trivial and yields Equation 3.12, where C is a constant of integration that can be solved for if the exit velocity is known. To estimate an exit velocity the 2-D expansion model is invoked from Section 1.2.2, neglecting ion-neutral collisions for simplicity, and a value of γ determined by fitting results to the Doppler shift measurements, using $\theta_{div} = 8.5^o$ as discussed in the following chapter. The velocity profiles were found using a basic root finding in Matlab, choosing the root corresponding to a decreasing neutral density.

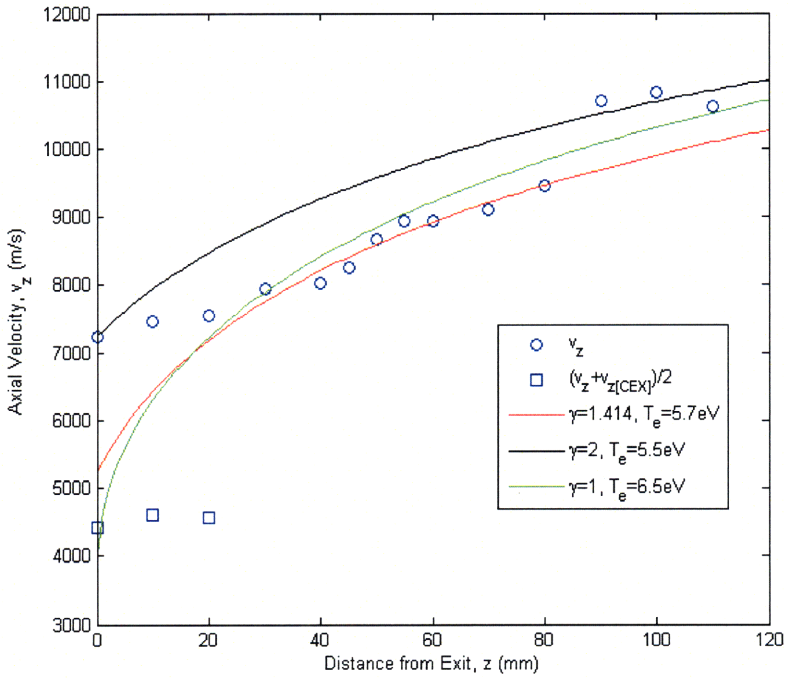

Figure 3-42: Axial Velocity vs. Distance from Thruster Exit with Fits from the 2-D Expansion Model to Fast Ion Doppler Shift Data and the Average of Fast and Slow Ion Doppler Shift Data. Operating at 1333 G and 0.475 mg/s of Argon

Figure 3-42 shows the results using several combinations of fit parameters γ and T_e. The figure shows that γ=2 if the exit velocity is truly that found using the two-peak fitting routine. If the exit velocity is instead somewhere between the CEX and fast velocity measured by the peak fitting method, then the best fit is given by γ=1, corresponding to a sonic exit velocity for the ion species.

An axial ion velocity model can then be found in the form of Equation 3.13 by applying the assumption that ions become sonic at the thruster exit. This derivation requires a constant neutral density over the region of interest. It is also worth noting that the relation shown in Equation 3.11 no longer matches the data at distances greater than 80 mm.

$$v_i^2 = \frac{2kT_e}{n_n \sigma_{in} m_i \lambda_i} \left(\frac{n_n \sigma_{in} \lambda_i}{2} + 1 - e^{-n_n \sigma_{in} z} \right) \tag{3.13}$$

Estimates of the axial ion velocity profile can be obtained for the different conditions if the relevant cross sections and neutral density can be accurately estimated. The charge exchange cross section is 3.4-5.6 10^{-19} m^2 for ion energies from 1-10 eV using Equation 3.9, while the ion-neutral hard sphere collision cross section is only 0.6×10^{-19} m^2 and can be neglected when estimating σ_{in}.

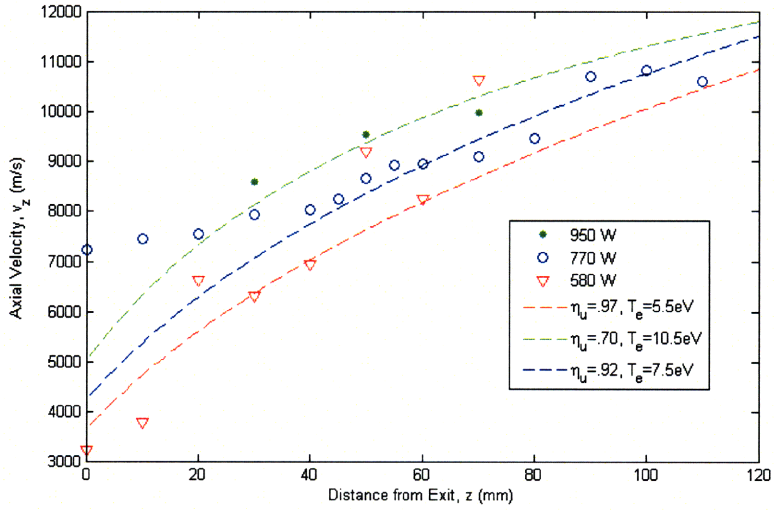

Figure 3-43: Axial Velocity vs. Distance from Thruster Exit with Fits from the 2-D Expansion Model to Fast Ion Doppler Shift Data and the Average of Fast and Slow Ion Doppler Shift Data. Operating at 1333 G and 0.475 mg/s of Argon

Application of this semi-empirical model to the axial velocities measured by Doppler shift for the fast moving ion species is shown in Figure 3-43 where both η_u and T_e are varied to obtain the best fit. The increase in electron temperature with power required to match the results is as expected, but the decrease in utilization efficiency is at odds with both our expections and the results of Figure 3-20 which shows a clear increase in ion-to-neutral emission fraction with RF power. The utilization efficiency is related to the ratio $x = I_{434.8}/I_{433.4}$ by,

$$\eta_u = \frac{x}{x + \frac{c_{s_n}}{c_{s_i}}} \tag{3.14}$$

where c_{s_i} is proportional to $T_e^{1/2}$, so if x and T_e are both increasing with power, so should η_u. The decrease in η_u with power in Figure 3-43 due to the increasing concavity of the velocity profiles which corresponds to the measured neutral growth in Table 3.2 getting shallower at lower powers. The measured plasma decay lengths have little effect on the results.

Figure 3-44 shows the results of fitting the 2-D expansion model to the same Doppler shift data, all with γ=1. A similar increase in T_e with P_{rf} is found, though it is more linear than estimated with the semi-empirical model.

The effect of the magnetic nozzle is excluded from this analysis because we are working under the assumption of cold ions. If the ion temperature is less than 1eV then conservation of the magnetic dipole moment will only lead to an increase in parallel velocity of less than 400 m/s when the magnetic field goes to zero.

The assumption of negligible ∇T_e is left for experimental verification, but is expected to remain valid. The emission decay lengths suggest $\nabla n_e/n_e$ is around 32 so for an electron temperature as low as 3eV near the thruster exit, a gradient of about 1 eV / cm is necessary to be on par with the ∇n_e effect. No such gradient is found in the invasive probe measurements of the following chapter.

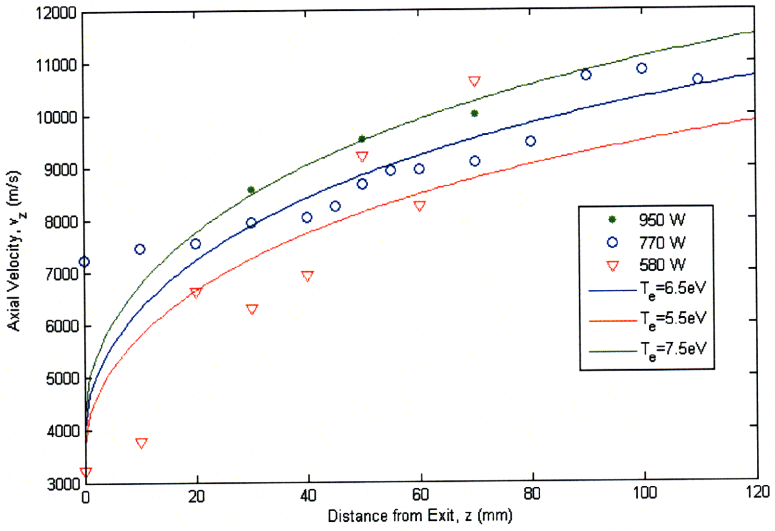

Figure 3-44: Axial Velocity vs. Distance from Thruster Exit with Fits from the 2-D Expansion Model to Fast Ion Doppler Shift Data and the Average of Fast and Slow Ion Doppler Shift Data. Operating at 1333 G and 0.475 mg/s of Argon

Chapter 4

Invasive Measurements of the mHTX

Langmuir probe measurements of the spatial trends in ion flux and electron temperature in the near plume were made for comparison with the spectral data. The invasive probe data is intended to verify the on-axis dominated emission approximation, isothermality of the electrons near the exit and the spectrally measured exponential decay in ion density. The ensuing section describes the results of this verification and compares the results of the two diagnostics.

4.1 Current-Voltage Characteristics

A Fluke 21 II Hand-Held Multimeter was set parallel to a R_m=3.4 kOhm [Figure 2-11] measurement resistor to monitor the current through the circuit as the probe tip voltage was swept across a range of negative biases with respect to the vacuum chamber ground. Initial scans were made at various distances from the thruster exit along the central axis to determine the bias necessary to repel the majority of the electron current.

The resulting curves, plotted in Figure 4-1, show that while the positive ion current never really saturates it does behave fairly linearly at all locations below around -50 V. There is also a general trend of increasing dependence of the probe current

on tip potential with distance from the exit, which adds some complexity to the interpretation of ion saturation current at different axial positions.

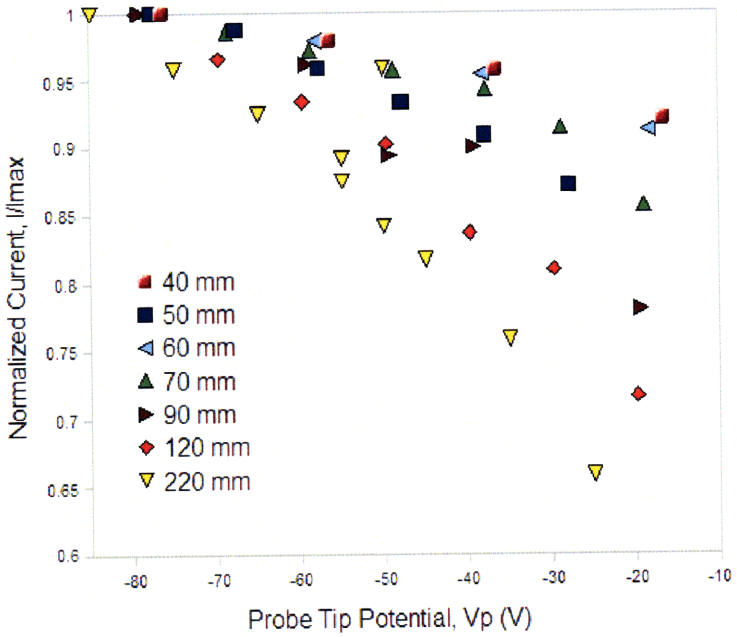

Figure 4-1: Normalized Probe Current vs. Probe Tip Potential at Various Distances from Exit. Operating at 770 W, 1333 G and 0.475 mg/s of Argon.

Linear fits to the ion currents in Figure 4-1 are extrapolated to zero probe tip voltage for comparison with the raw data at a constant bias of -80 V. The resulting curves, plotted in natural logarithm in Figure 4-2, exhibit exponential decays within 10 cm of the thruster, characterized by decay lengths of 38 mm and 32 mm for the -80 V and 0 V cases respectively.

Further probing into the electron current dominated regime was accomplished using a series of 9 V batteries to apply a constant -27 V bias between one end of the Sorensen power supply and ground. The polarity of the Sorensen was reversed to allow the probe tip to reach large positive potentials and the measurement resistor was changed to 9 kOhm for compatibility with the NI 6009 USB DAQ used to record the data. The resulting I-V curves, shown normalized in Figure 4-3(a), exhibited spatial characteristics similar to those shown in Figure 4-2.

The normalization to maximum current collected at each axial location is misleading when determining electron temperature trends due to the expected shift in

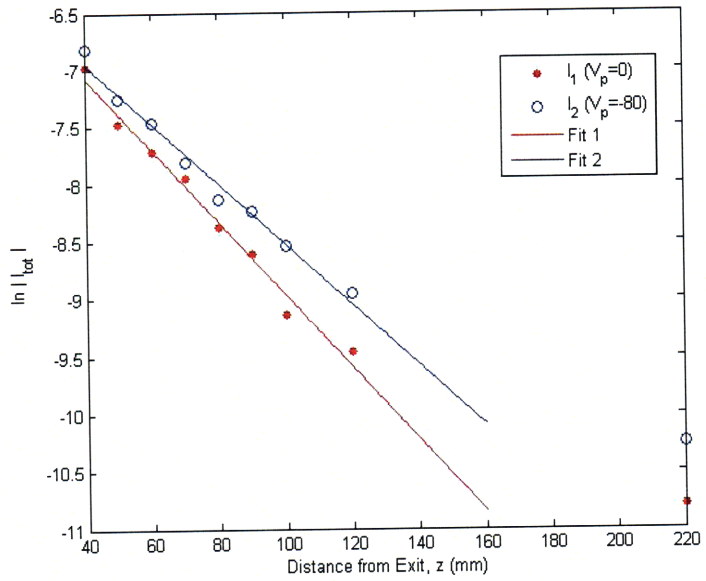

Figure 4-2: Natural Logarithm of Probe Current vs. Distance the from Exit. Taken at -80 V Probe Tip Potential and Extrapolated to 0 V Probe Tip Potential. Operating at 770 W, 1333 G and 0.475 mg/s of Argon.

the floating potential as one moves closer to the thruster, shown for all conditions studied in Figure 4-4. Shifting all curves by their respective floating potentials and normalizing each by pinning the maximum measured current to the I-V curve at 80 mm results in Figures 4-3(a-c), which allows a better assessment of the differences in temperature. The curves collapse onto one another indicating similar temperatures, with the slight exception of the curve at 60 mm which appears to have a somewhat higher temperature.

It is clear from Figure 4-3(b) that different sections of the I-V curve are being measured at different axial locations due to the large floating potential shifts, which complicates the normal procedure for calculating electron temperatures by obscuring the ion portion of the collected current. Assuming the current collected with a -80 V bias on the Sorensen power supply is the constant valued ion current at each position yields mixed results, and even grossly undershoots the apparent ion current at some locations due to the relatively high uncertainty in the measurement.

Good comparisons can be made between locations using the same pinning technique displayed in Figures 4-3(b-d), but one must still prescribe a normalized ion

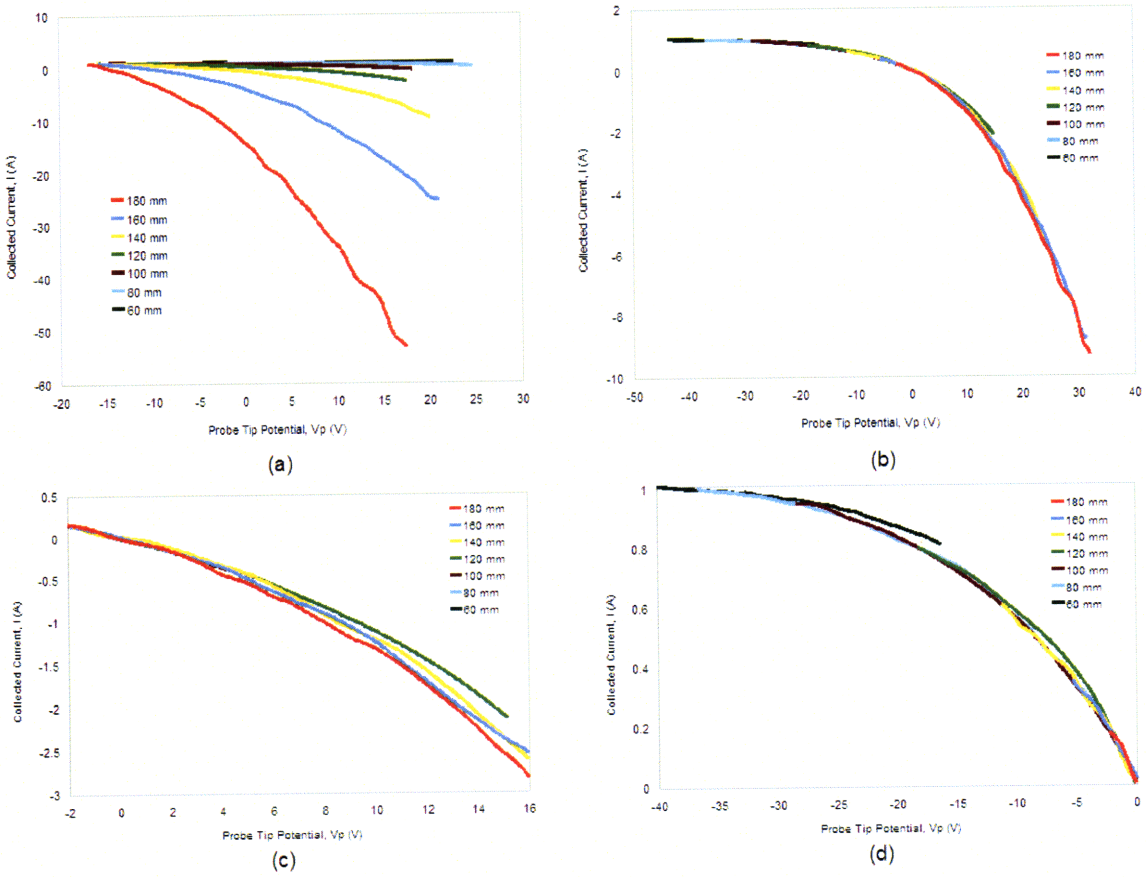

Figure 4-3: Probe Current vs. Probe Tip Potential at Various Distances from Exit. (a) Normalized to Maximum Current Individually (b) Floating Potential at Origin Normalized to Curve at 80 mm (c,d) Blow up of (b). Operating at 770 W, 1333 G and 0.475 mg/s of Argon.

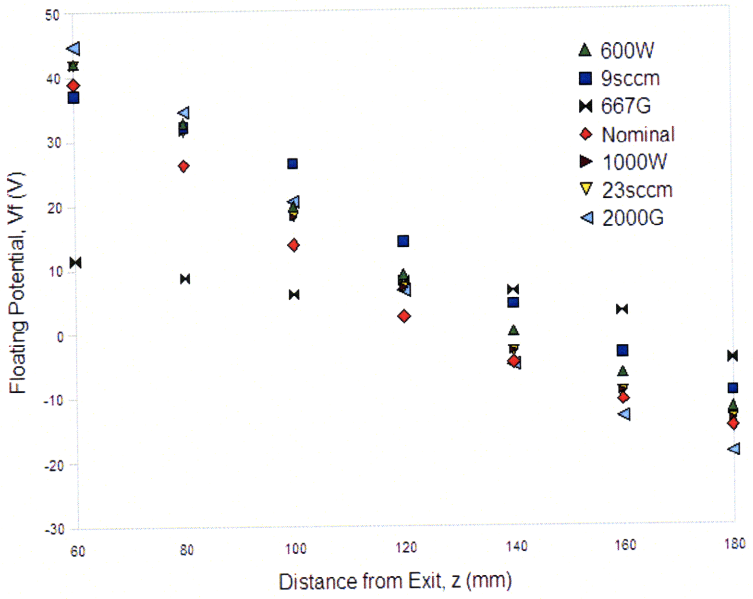

Figure 4-4: Floating Potential vs. Distance the from Exit at Various Operating Conditions. Nominal Operation at 770 W, 1333 G and 16 sccm of Argon.

current to allow temperature estimates. An ion current was chosen which maximizes the correlation coefficient for a linear fit of the natural logarithm of the electron current. The resulting electron current curves are given for each condition in Appendix 6, with their corresponding average electron temperatures shown in Figure 4-5.

The results are mixed and could benefit from the averaging of several curves at each datum location. Few trends are evident from Figure 4-5, save an apparent inverse relation between temperature and flow rate. Uncertainty analysis is somewhat superseded by the arbitrariness of steps in the data reduction related to the incompleteness of the data. Rather the main utility of the data is in the similarity of the measured curves.

Constancy of electron temperature in the near plume makes the floating potential a function of only plasma potential and RF fluctuation amplitude, as given in Equation 4.1, which is found by setting Equation 1.31 equal to Equation 1.32. The drops in floating potential with distance from exit that are displayed for most conditions in Figure 4-4 are due in this case to a strong negative gradient in plasma potential, the true shape of which is obscured by RF effects. If the RF fluctuation potential equals the electron temperature the floating potential is shifted left by $T_e/4.2$, an effect that

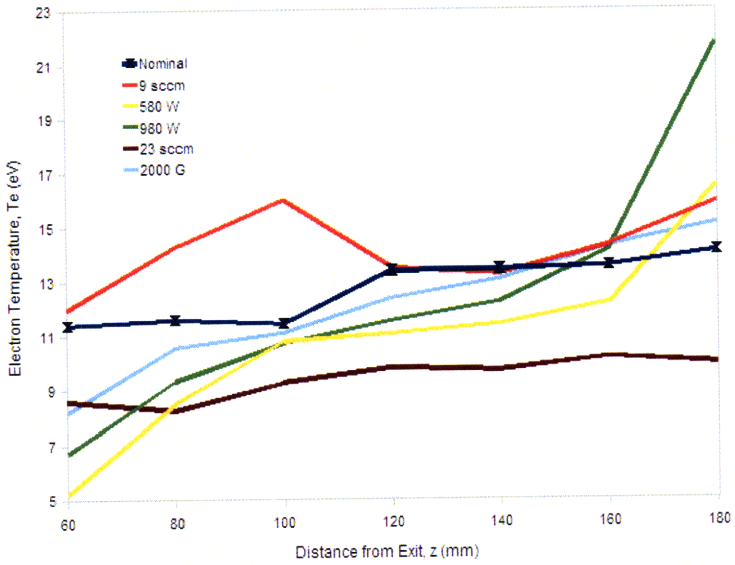

Figure 4-5: Electron Temperature vs. Distance the from Exit at Various Operating Conditions. Nominal Operation at 770 W, 1333 G and 16 sccm of Argon.

decreases precipitously for lower RF voltages. If the RF voltage is as much as ten times the temperature V_{fl} is shifted by $8T_e$.

$$V_{fl} \simeq V_{pl} + kT_e \left[\frac{1}{2} ln(\frac{2\pi m_e}{m_i}) - ln(I_0(\frac{V_{rf}}{kT_e}))\right] \tag{4.1}$$

4.2 Electron Repelling Spatial Scans

The ion-dominated current was monitored as the probe was scanned along y-axis (x=0) for several z-axis locations in order to verify the assumption that the plasma density is strongly peaked along the thruster axis in the region of spectroscopic interest. The previous section showed that in general the collected current tended to linearize to positive (thus ion-dominated) currents at bias voltages of around -50 V, so this point was chosen to examine the radial trends in ion current.

The natural logarithm of the measured current at several locations is given in arbitrary units in Figure 4-6 for comparison. Measured current drops by more than 90% within 15 mm of the thruster axis at axial distances of 5 cm and closer. At 13 cm from the exit the current drops by 50 % within a 2 cm radius, while it takes roughly

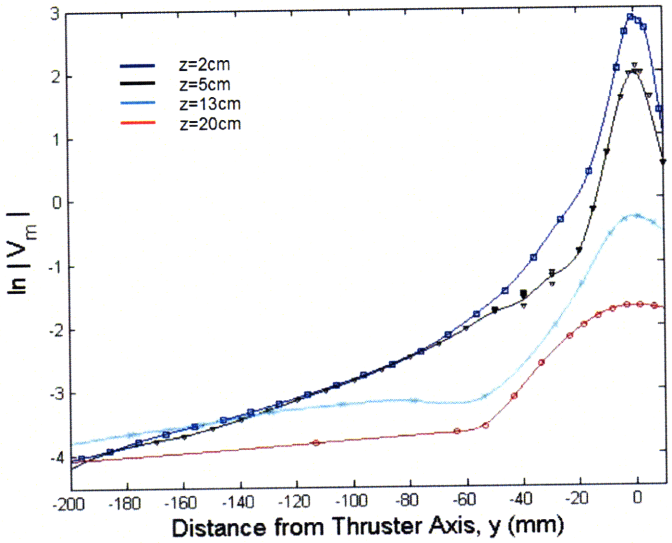

Figure 4-6: Natural Logarithm of the Voltage Across the Current Measuring Resistor vs. Y-Axis Location at Various Distances from Thruster Exit. Operation at 770 W, 1333 G and 16 sccm of Argon.

35 mm to drop that much at an axial distance of 20 cm.

A contour plot of cubic spline fits to the results, shown in Figure 4-7(b), displays a small degree of divergence. Visually, the plume appears stratified between a central jet about the size of the confinement tube, a conically shaped region the size of the magnet bore, and an outer diffuse region which appears to diverge somewhat with the magnetic field lines.

The total ion current through a given circular cross-section is not directly measured. Instead the current density, $J(r_i)$, is measured at discrete radial positions, where $r = \sqrt{x^2 + y^2}$.

$$I(R) = \int_0^{2\pi} \int_0^R J(r) dr r d\theta \tag{4.2}$$

The total ion current can be estimated from these measurements using Equation 4.3, which is simply the midpoint quadrature of Equation 4.2.

$$I \simeq \pi \sum_{i=1}^{N} [J(r_{i+1}) r_{i+1} + J(r_i) r_i][r_{i+1} - r_i] \tag{4.3}$$

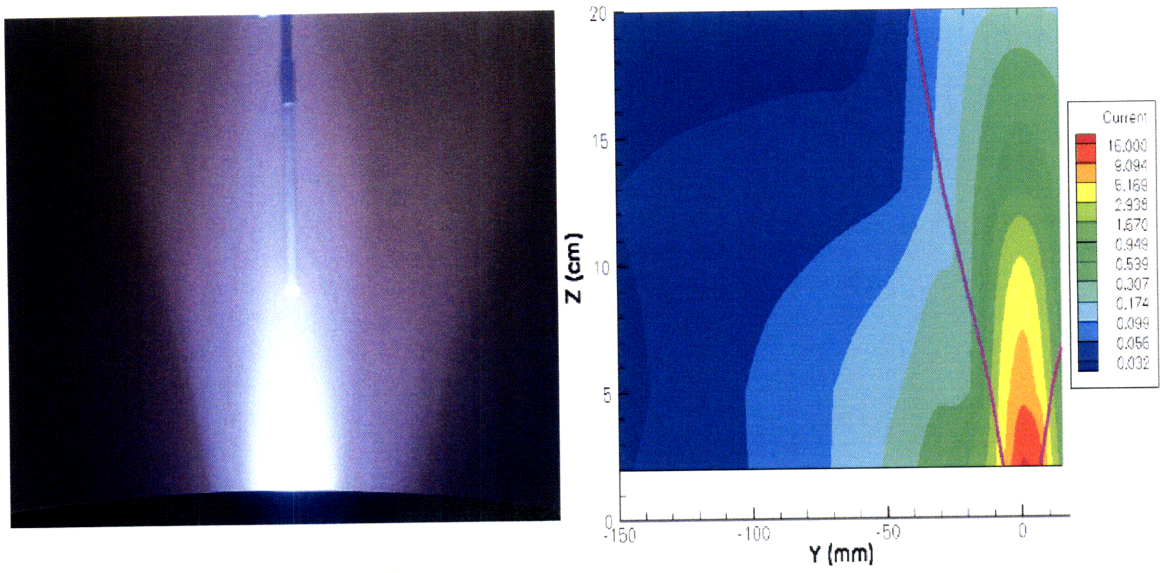

Figure 4-7: (a)Photograph of Langmuir Probe in Near Plume (b) Y-Z Contour Plot of Ion Current on an Exponential Scale with Divergence Angle Overlaid. Operation at 770 W, 1333 G and 16 sccm of Argon.

Here the current density is assumed to be circularly symmetric, relieving any angular dependencies from the equation. The validity of this assumption is questionable and should be examined experimentally.

The results of integrating the obtained ion current profiles from the thrust axis to a radius of 15 cm using Equation 4.3 are shown in Figure 4-8. An exponential fit to the data results in a decay length of 98 mm and an extrapolated utilization efficiency of 99% at the exit, with a correlation coefficient of 0.994.

The ion flux is not expected to decrease noticeably over the distances measured here. It is possible that the unprobed current in the far wings is responsible for the shortfall, since the scans here account for limited angles of ion flow from the exit, with $\theta_{div} = tan^{-1}\frac{R-a}{z}$ ranging from 81^o at z=2 cm to 33^o at 20 cm.

It is also worth noting that although changes in the current-voltage characteristic were observed at different positions the bias voltage for electron repulsion was kept constant during these spatial scans. The probe is therefore measuring the current in different portions of the I-V characteristic as the probe position is altered, and

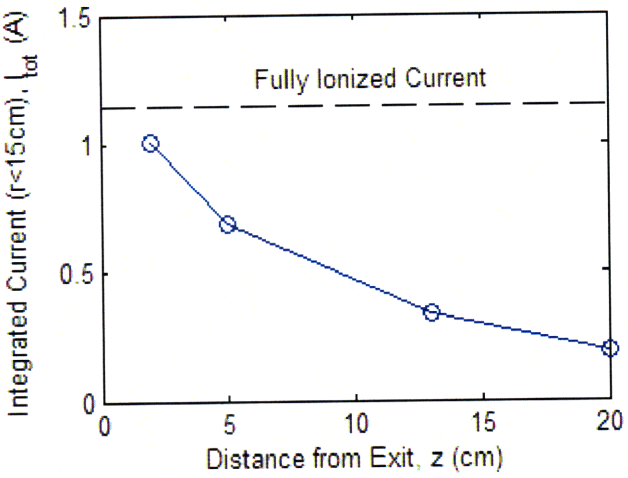

Figure 4-8: Ion Current Integrated Through a Circle of 15 cm Radius on the X-Y Plane vs. Distance from Thruster Exit. Operation at 770 W, 1333 G and 16 sccm Argon. The Current Resulting from Complete Single Ionization of Incoming Gas Flow is Shown.

for example, may be collecting sufficient electron current in regions far from the exit to suppress the ion current measurements in these locations. This effect could be minimized in a straightforward manner by simply increasing the bias potential far enough below ground that all profiles exhibit only slow changes.

The mean divergence angle of the plume was calculated using Equation 4.4 on each of the spline fitted profiles. The results show a self-collimating effect, with the divergence angle falling from 19^o at 2 cm to 11^o at 20 cm. The current weighted mean angles are overlaid on the contour plot of ion current in Figure 4-7(b). These angles are slightly different from the θ_{div} defined in Section 1.2.2 in that they are defined from z_{ex}=0 instead of $z_{ex} = -z_0$. Measuring the angle from z_0 gives a divergence of 8.5^o at 20 cm.

$$\overline{\theta_{div}}(R,z) = \frac{\int_0^R J(r) tan^{-1}\left(\frac{r}{z}\right)\, dr}{\int_0^R J(r)\, dr} \tag{4.4}$$

The effects of the finite pumping speed of the chamber on the radial profile near the exit were examined by leaking in known amounts of Argon into a port on the -y side of the chamber as was done in Section 3.2. An external flow of 10 sccm of Argon resulted in a pronounced increase in collected current at radial distances greater than

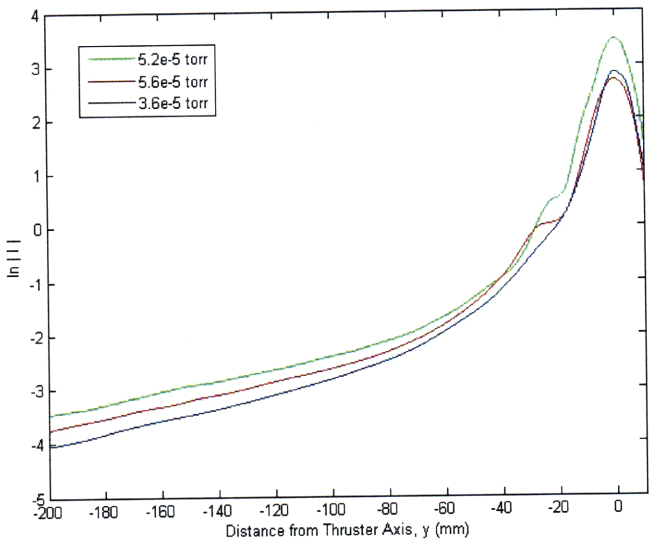

Figure 4-9: Natural Logarithm of the Ion Current vs. Y-Axis Location 2 cm Downstream of Thruster Exit. Operation at 770 W, 1333 G and Either 16 sccm of Argon with No External Flow (36microTorr), with 10 sccm External Flow (56microTorr) or with 23 sccm of Argon and No External Flow (52microTorr).

3 cm, but nearly identical current within the plasma jet, as seen in Figure 4-9.

An increase in background pressure due to external flow is expected to result in a corresponding increase in charge exchange ions. The low energy CEX ions are forced away from the core by gradients in the plasma potential, creating the characteristic humps seen forming around 3 cm from the thrust axis [4]. When the propellant flow input to the thruster was increased by 7 sccm instead of the external flow, both the hump near 3 cm and an increase in the plasma jet current were noted.

4.3 Comparison to Spectral Results

Axial scans of the ion current were conducted with the Langmuir probe biased to -80 V to allow a straightforward comparison with the radially measured emission characteristics. The maximum magnetic field strength, propellant mass flow rate and delivered RF power were scanned in the usual way.

Figure 4-10 once again illustrates the strong dependence of ion flux exiting the thruster on the applied magnetic field strength. An asymptotic trend appears at high

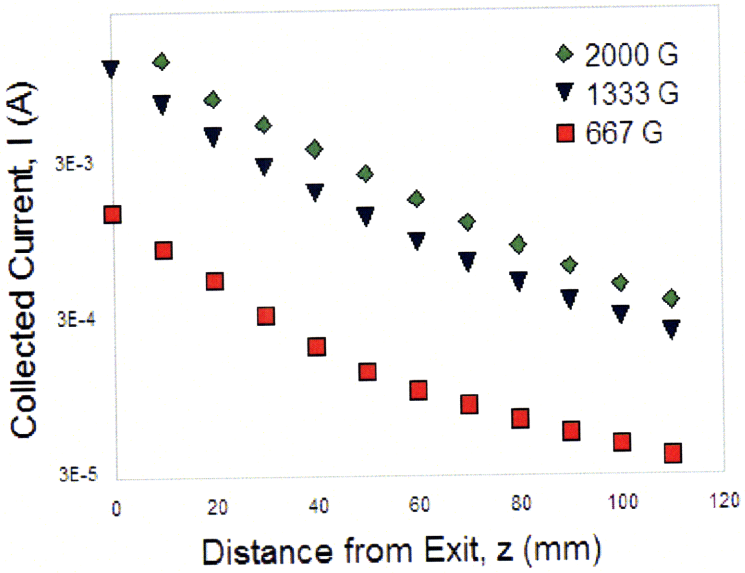

Figure 4-10: Probe Current vs. Distance from Exit at -80 V Bias. Operating at 770 W, 0.475 mg/s of Argon and Various Magnetic Field Strengths.

values of applied field in an identical manner as observed by emission spectroscopy. At lower field strengths ions flow unimpeded to the walls of the confinement tube where they recombine forming neutrals, drastically reducing propellant utilization.

Figure 4-11 shows an almost linear dependence of ion flux at the exit on propellant mass flow rate. Measurements of emission at 434.8 nm and 433.4 nm did not suggest a linear increase in ionization fraction with flow rate once again indicating an inverse relationship between flow rate and ion velocity. At higher mass flow rates the ion flux appears to decay over a shorter distance than at low flow rates, just as indicated by the decay of Ar II to Ar I emission intensity ratios.

The results of the RF power scan, shown in Figure 4-12, indicate a maximum ion flux is obtained for delivered power levels between 580 and 980 W. The spectroscopic measurement of ionization fraction shows a similar trend, although it is much less pronounced. Interestingly, Figure 4-4 reveals a minimum in floating potential occurring between 580 and 980 W.

The steep drop-off in measured ion flux between 770 W and 980 W was thought once again to be due to in part to the rightward shift of the I-V characteristic at 980 W. A 16 V increase in floating potential was measured from 770 W to 980 W a

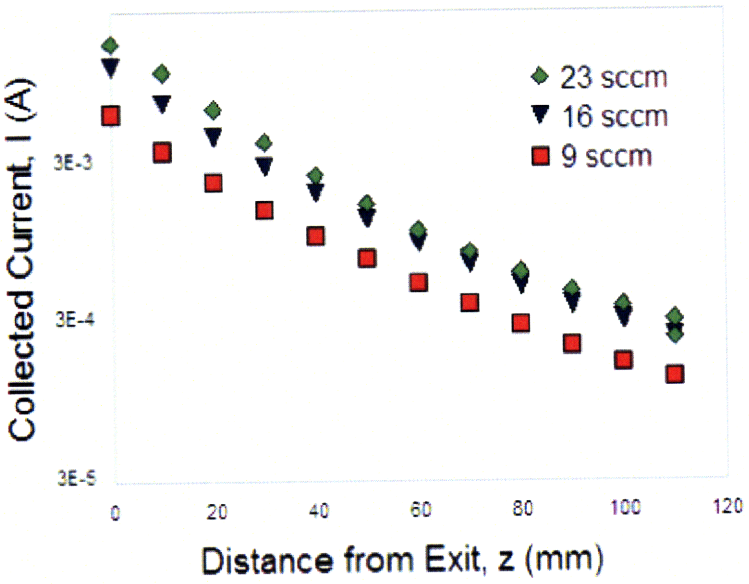

Figure 4-11: Probe Current vs. Distance from Exit at -80 V Bias. Operating at 770 W, 1333 G and Various Mass Flow Rates of Argon.

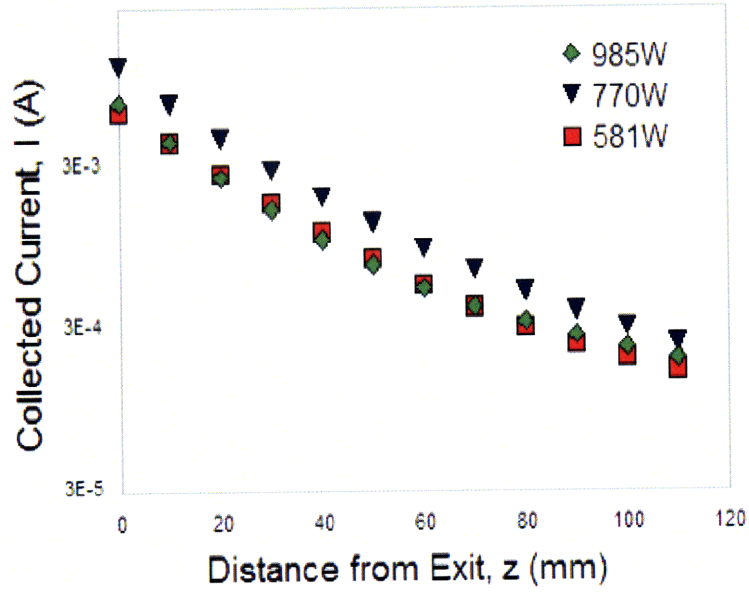

Figure 4-12: Probe Current vs. Distance from Exit at -80 V Bias. Operating at 1333 G, 0.475 mg/s of Argon and Various Values of Delivered RF Power.

distance of 6 cm from the exit. At a -65 V bias the collected current was 94% of that collected at -80 V under nominal operating conditions. The ion current at 980 W, measured 6 cm from the exit, however, was only 59% of the nominal current, a trend seemingly refuted by the spectroscopic measurements of Figures 3-20 and 3-41.

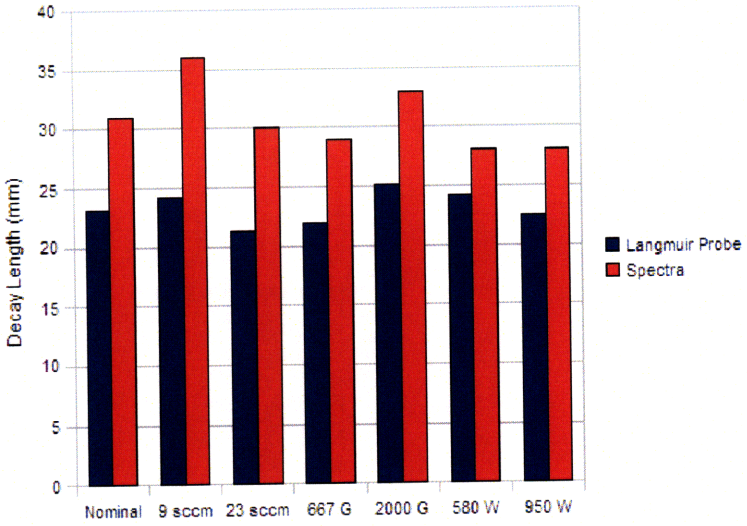

Figure 4-13: Characteristic Length of Plasma Density Decay for Various Operational Modes as Inferred by Langmuir Probe and Emission Spectroscopy Measurements.

The Langmuir probe measured ion current decays nearly exponentially in the region up to 6 cm downstream of the exit, allowing similar decay length measurement to those discussed in the previous chapter. The decay length measured spectroscopically, presented graphically in figure 4-13, is 7.5 mm longer on average than measured by the Langmuir probe with a standard deviation of 2.5 mm. The stronger deviation from an exponential decay noted by invasive measurements may be due to the acceleration of ions downstream of the exit, as the Langmuir probe is used to measure ion flux rather than density.

Figure 4-14 compares several ratios exhibiting, under our assumptions, proportionality to the plasma density. The plot shows the ion current dropping twice as much as the square root of Ar II emission does over 10 cm, indicating a stronger pressure gradient than predicted by simple emission spectroscopy. The growing discrepancy between the measurements with distance from thruster may be due to the divergence of the plume depopulating the central stream quicker than indicated by

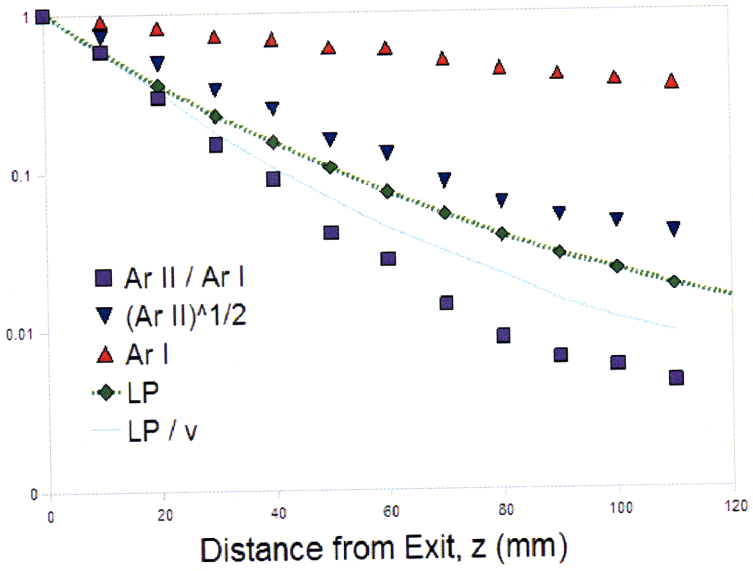

Figure 4-14: Different Ratios Proportional to Plasma Density vs. Distance from Exit. Operating at 770 W, 1333 G and 0.475 mg/s of Argon. (Ar II/Ar I) 434.8 nm to 433.4 nm Emission Intensity Ratio (Ar $II^{1/2}$) Square Root of 434.8 nm Emission Intensity (Ar I) 433.4 nm Emission Intensity (LP) Langmuir Probe Measured Ion Current (LP/v) Probe Current Over Doppler Measured Axial Velocity

the line-of-sight integrated spectral measurements.

4.4 Uncertainty Analysis

The uncertainties in the invasive data were difficult to quantify due to a somewhat erratic dependence of the collected current on time. At times a repeatable and stable current could be measured. At nominal conditions multiple measurements were made at certain locations which showed a reasonable quiescent deviation. At z=2cm and y=-5cm the standard deviation over two separate thruster firings (seven total measurements) is 7% of the mean measured current. The standard deviation from three measurements at y=-0.1cm is similar at 6% of the mean measured current.

As the system, both thruster and probe, heat up a steadily decreasing current was noted while the probe remained stationary. Time resolved measurements of the decreasing current revealed an almost uniform drop of 3%/minute when taken over 3 to 6 minute runs in the center of plume. Measurements were made at axial distances of 11 and 21 cm downstream of the exit. Current measurements at y=0 and z=11cm with a bias of -50V had a standard deviation 5% of the mean current during three separate runs performed over a time period of two hours. The third run, which was taken after a 90 minute cool-down from the first two exhibited a much slower decay in current over time of less than 0.1%/minute.

Average scans along the y-axis lasted 6 minutes with several lasting as long as 12 minutes. If the average drop per minute measured over the three minute scans holds for longer scans, measured currents would be expected to drop anywhere from 18 to 36% over the course of a run. Good correlation to the predicted drop in current was found for two such y-scans when measurements were made at y=-5cm at roughly 6 minute intervals during one continuous firing.

While accounting for the decrease in measured current with time eliminates the discrepancy between measurements at the same point during the same run, it does not alleviate the poor run-to-run precision. The measured current still changed by as much as 26% between two lateral scans at 5cm downstream of the exit. This large discrepancy was confined to data points taken at positive y locations. The error was only as high as 12% for all other y positions.

Later attempts to confirm the observed drops revealed no clear patterns in time. Current dropped monotonically for a time before reversing directions. After rising slightly over a short interval, the current apparently stabilized. Upon returning to the same position at a later point in the run a different current was measured and a steady increase in time noted, with no stabilization observed. Ultimately, after collecting current at one point for a total of 22 minutes, the standard deviation of the data was 6.6% of the mean. The stable current was, incidentally, 93% of the mean. A standard deviation of 5% of the mean occured in similar data taken over a total of 26 minutes at a point closer to the thruster axis.

Chapter 5

Conclusions

A simple method of analysis was presented for the characterization of electric propulsion devices with emission spectroscopy and applied to measurements of a Helicon thruster experiment over a narrow optical bandwidth. Although none of the optical measurements provide absolute values for any plasma parameter, save the Doppler shift scans, they do allow qualitative comparisons to be made easily between operating conditions.

5.1 Applicability of OES

The simple application of optical emission spectroscopy provides a qualitative tool for the observation of the effects of operational conditions on the state of the plasma. Comparison of relative intensities of emission from the propellant gas at different states of ionization, along with comparison of the emitted line widths, provide a relatively easy-to-apply litmus test of operational effects on plasma temperature.

The small temperature gradients measured in the region of interest justify the use of ion-to-neutral emission ratios as an indicator of axial trends in the ionization fraction. The results of the axial scans were corroborated to varying degrees by invasive measurements, which present many drawbacks of their own in singling out plasma parameters.

5.2 Implications on Thruster Design

Only one thruster configuration was examined in this study with sparse parametric scans, limited to RF power, propellant flow rate and B-field strength. Several trends were noticeable, however, which can be levied to optimize thruster geometries.

The magnetic field topology appears to have a strong effect on the utilization efficiency until a saturation point is reached. Little effect on the ion velocity was noted sufficiently downstream when the field strength was brought above 1333 G. These results suggest an optimal field can be obtained which sufficiently collimates the beam to avoid heavy losses to confinement tube walls but is not strong enough to hinder detachment or trap a substantial population of low energy ions.

The propellant flow rate was shown to have an inverse relationship with the final ion velocity in the plume. The velocity increase appears to be due to the relatively higher electron temperatures achieved at higher ratios of input power to input propellant flux rather than a change in the plasma density gradient. Energy efficiency can then be maximized for a given mission by throttling the mass flow rate as the orbital velocity decreases. The exact effects of doing so on the provided thrust have yet to be characterized.

The power scans, though somewhat inconclusive, point to an interesting interplay between delivered RF power, ionization fraction and the plasma temperature. A more complete study is needed to isolate competing effects, but preliminary results show little advantage in extending the operation to higher powers.

5.3 Suggested Future Work

The optical measurements were idealized as dominated by the central region, ascribing to them a spatial resolution that is increasingly tenuous at distances further than 5 cm from the thruster exit. A more thorough examination of the effects of the volume integration which each measurement truly represents can be made using topographic techniques, which may be simplified by the cylindrically symmetric geometries of the

thrusters examined. These experiments can be carried out easily with the acquistion of an accurate 2-D translation stage.

More Langmuir probe scans are needed to eliminate systematic error as a possible cause for some of the observed trends. Drifts in the measured current over time were in some cases quite substantial, necessitating corroboration of the initial data.

Similar time dependence may arise in the optical measurements as coating of the optical apparatus and drift in alignment may create some unaccounted for error. Corroboration of the data with similar and more complete scans is recommended if these diagnostic methods are to be pursued.

Bibliography

[1] E. Ahedo and M. Martinez-Sanchez. The role of current-free double-layers in plasma propulsion. *44th AIAA/ASME/SAE/ASEE Joint Propulsion Conference*, 2008.

[2] A. Anders, S. Anders, and E. Hantzsche. Validity conditions for complete and partial local thermodynamic equilibrium of nonhydrogenic level systems and their application to copper vapor arcs in vacuum. *IEEE Transaction on Plasma Science*, 1989.

[3] A.V. Arefiev and B.N. Breizman. Theoretical components of the vasimr plasma propulsion concept. *Physics of plasmas*, 2004.

[4] Y. Azziz. *Experimental and Theoretical Characterization of a Hall Thruster Plume.* PhD thesis, Massachusetts Institute of Technology, 2007.

[5] O. Batishchev and K. Molvig. Kinetic model of a helicon plasma source for vasimr. *39th ASME/AIAA*, 2001.

[6] O. Batishchev and K. Molvig. Numerical study of plasma production in the vasimr thruster. *27th IEPC*, 2001.

[7] O. Batishchev, K. Molvig, F. Chang-Diaz, and J. Squire. Study of gas burn-out regime in the vasimr helicon plasma source. *30th EPS CFPP Conference*, 2003.

[8] O. Batishchev, J. Pucci, N. Sinenian, Z. LaBry, M. Celik, and M. Martinez-Sanchez. Mini-helicon thruster experiment at mit. *48th Meeting of Division of Plasma Physics*, 2006.

[9] O. Batishchev, N. Sinenian, M. Celik, and M. Martinez-Sanchez. Development of the mini-helicon thruster at mit. *30th IEPC*, 2007.

[10] B.E. Beal, A.D. Gallimore, and W.A. Hargus. Preliminary plume characterization of a low-power hall thruster cluster. *AIAA Journal*, 2002.

[11] A.A. Belevtsev, V.F. Chinnov, and E.K. Isakaev. Emission spectroscopy of highly ionized high-temperature plasma jets. *Plasma Sources Science and Technology*, 2006.

[12] I.A. Biloiu, E.E. Scime, C. Biloiu, and S.A. Cohen. Validity conditions for complete and partial local thermodynamic equilibrium of nonhydrogenic level systems and their application to copper vapor arcs in vacuum. *IEEE Transaction on Plasma Science*, 1989.

[13] F.R. Chang-Diaz. An overview of the vasimr engine: High power space propulsion with rf plasma generation and heating. *Radio frequency power in plasmas*, 2001.

[14] C. Charles and R. Boswell. Current-free double-layer formation in a high-density helicon discharge. *Applied physics letters*, 2003.

[15] F.F. Chen. Plasma ionization by helicon waves. *Plasma Physics and Controlled Fusion*, 1991.

[16] F.F. Chen and R.W. Boswell. Helicons-the past decade. *IEEE Transaction on Plasma Science*, 1997.

[17] Y. Chiu, B.L. Austin, S. Williams, R.A. Dressler, and G.F. Karabadzhak. Passive optical diagnostic of xe-propelled hall thrusters i. emission cross sections. *Journal of Applied Physics*, 2006.

[18] S.A. Cohen, N.S. Siefernt, S. Stange, R.F. Boivin, E.E. Scime, and F.M. Levinton. Ion acceleration in plasmas emerging from a helicon-heated magnetic-mirror device. *Physics of Plasmas*, 2003.

[19] C.M. Dennin, M. Wiebold, and J.E. Scharer. Observations of neutral depletion and plasma acceleration in a flowing high-power argon helicon plasma. *Physics of Plasmas*, 2008.

[20] N. Dorval, J. Bonnet, and J.P. Marque et. al. Determination of the ionization and acceleration zones in a stationary plasma thruster by optical spectroscopy study: Experiments and model. *Journal of Applied Physics*, 2002.

[21] E.Hinnov and J.G. Hirschberg. Electron-ion recombination in dense plasmas. *Physical Review*, 1962.

[22] C. Foissac, C. Dupret, and P. Supiot. Electrical and spectroscopic characterizations of a low pressure argon discharge created by a broad-band helical coupling device. *Journal of Physics D: Applied Physics*, 2009.

[23] C. Foissac, M. Kramer, and B. Lorenz. Spectroscopic investigations of electron heating in a high-density helicon discharge. *Journal of Physics D: Applied Physics*, 2007.

[24] Takashi Fujimoto. *Plasma Spectroscopy.* Oxford University Press, 2004.

[25] A. Ganguli, B.B. Sahu, and R.D. Tarey. A new structure for rf-compensated langmuir probes with external filters tunable in the absence of plasma. *PLASMA SOURCES SCIENCE AND TECHNOLOGY*, 2007.

[26] D. Gawron, S. Mazouffre, and C. Boniface. A fabry-perot spectroscopy study on ion flow features in a hall effect thruster. *PLASMA SOURCES SCIENCE AND TECHNOLOGY*, 2006.

[27] Hans R. Griem. *Principles of Plasma Spectroscopy.* Cambridge University Press, 1997.

[28] M. Hannemann and F. Sigeneger. Langmuir probe measurements at incomplete rf compensation. *CZECHOSLOVAK JOURNAL OF PHYSICS*, 56, 2006.

[29] W.A. Hargus and C.S. Charles. Near exit plane velocity field of a 200-watt hall thruster. *Journal of Propulsion and Power*, 2008.

[30] W.A. Hargus and M.R. Nakles. Evolution of the ion velocity distribution in the near field of the bht-200-x3 hall thruster. *42nd AIAA/ASME/SAE/ASEE Joint Propulsion Conference*, 2006.

[31] Ian H. Hutchinson. *Principles of Plasma Diagnostics.* Cambridge University Press, 2002.

[32] G.F. Karabadzhak, Y. Chiu, and R.A. Dressler. Passive optical diagnostic of xe-propelled hall thrusters ii. collision-radiative model. *Journal of Applied Physics*, 2006.

[33] J.H. Kim and H.Y. Chang. A study on ion energy distribution function and plasma potentials in helicon wave plasmas. *Physics of Plasmas*, 1996.

[34] M. Kramer, B. Clarenbach, and W. Kaiser. A 1mm interferometer for time and space resolved electron density measurements on pulsed plasmas. *Plasma sources science and technology*, 2006.

[35] M. Light, F.F. Chen, and P.L. Colestock. Quiescent and unstable regimes of a helicon plasma. *PLASMA SOURCES SCIENCE AND TECHNOLOGY*, 2002.

[36] Geoffrey Marr. *Plasma Spectroscopy.* Elsevier Publishing Company, 1968.

[37] R.F. Meulenbroeks, P.A. van der Heijden, M.C. van de Sanden, and D.C. Schram. Fabry-perot line shape analysis on an expanding cascaded arc plasma in argon. *Journal of Applied Physics*, 1993.

[38] M.R. Nakles, L. Brieda, G.D. Reed, W.A. Hargus, and R.L. Spicer. Experimental and numerical examination of the bht-200 hall thruster plume. *43rd AIAA/ASME/SAE/ASEE Joint Propulsion Conference*, 2007.

[39] B.J. Nichols and F.C. Witteborn. Measurements of resonant charge exchange cross sections in nitrogen and argon between 0.5 and 17 ev. *NASA Ames*, 1966.

[40] L. Oksuz, F. Sobern, and A.R. Ellingboe. Analysis of uncompensated langmuir probe characteristics in radio-frequency discharges revisited. *Journal of Applied Physics*, 1999.

[41] T.G. Owano, C.H. Kruger, and R.A. Beddini. Electron-ion three-body recombination coefficient of argon. *AIAA Journal*, 1993.

[42] J.E. Palaia. Empirical aspects of a mini-helicon plasma thruster experiment (mhtx@mit). Master's thesis, Massachusetts Institute of Technology, 2002.

[43] D.D. Palmer and M.L. Walker. Operation of an annular helicon plasma source. *44th AIAA/ASME/SAE/ASEE Joint Propulsion Conference*, 2008.

[44] D.D. Palmer, M.L. Walker, M. Manete, and et. al. Performance analysis of a medium-power helicon thruster. *44th AIAA/ASME/SAE/ASEE Joint Propulsion Conference*, 2008.

[45] J.M. Pucci. An analysis of energy balance in a helicon plasma source for space propulsion. Master's thesis, Massachusetts Institute of Technology, 2003.

[46] Yu Ralchenko, A.E. Kramida, J. Reader, and NIST ASD Team. Nist atomic spectra database (version 3.1.5), May 2009. http://physics.nist.gov/asd3.

[47] K.P. Shamrai and V.B. Taranov. Volume and surface rf power absorption in a helicon plasma source. *Plasma sources science and technology*, 1996.

[48] N. Sinenian. Propulsion mechanisms in a helicon plasma thruster. Master's thesis, Massachusetts Institute of Technology, 2008.

[49] Isaac Sudit and Francis Chen. Rf compensated probes for high-density discharges. *PLASMA SOURCES SCIENCE AND TECHNOLOGY*, 1994.

[50] Isaac Sudit and Francis Chen. Discharge equilibrium of a helicon plasma. *PLASMA SOURCES SCIENCE AND TECHNOLOGY*, 1996.

[51] X. Sun, C. Biloiu, R. Hardin, and E.E. Scime. Parallel velocity and temperature of argaon ions in an expandin, helicon source driven plasma. *Plasma sources science and technology*, 2004.

[52] M.D. West, C. Charles, and R.W. Boswell. Testing a helicon double layer thruster immersed in a space-simulation chamber. *Journal of Propulsion and Power*, 2008.

[53] D.B. White. Power balance in a helicon plasma source for space propulsion. Master's thesis, Massachusetts Institute of Technology, 2008.

[54] R. Winglee, T. Ziemba, L. Giersch, J. Prager, J. Carscadden, and B.R. Roberson. Simulation and laboratory validation of magnetic nozzle effects for the high power helicon thruser. *Physics of plasmas*, 2007.

[55] T. Ziemba, J. Slough, and R. Winglee. High power helicon propulsion experiments. *Space Technology and Applications International Forum*, 2005.

Chapter 6

Appendix A: Langmuir Probe I-V Curves

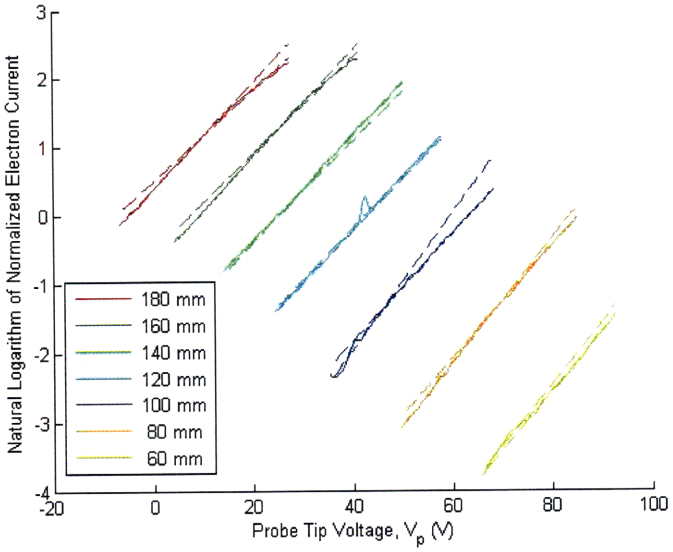

Figure 6-1: Natural Logarithm of Normalized Electron Current vs. Probe Tip Potential at Various Distances from Exit Arbitrarily Offset Along the Potential Axis for Clarity. Operating at 770 W, 1333 G and 0.475 mg/s of Argon.

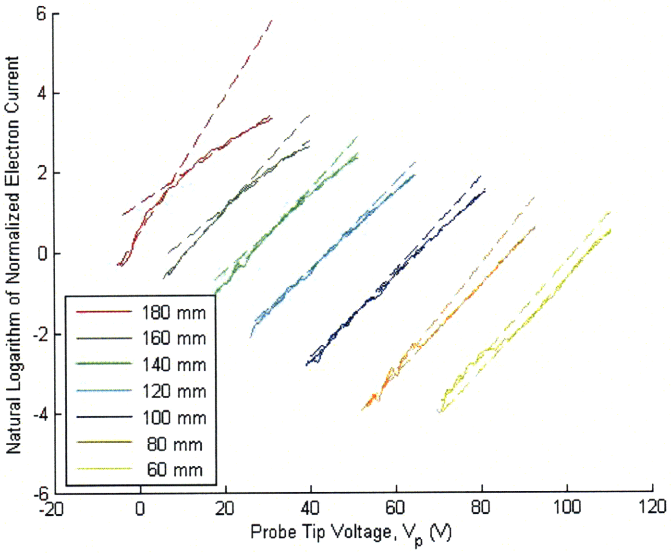

Figure 6-2: Natural Logarithm of Normalized Electron Current vs. Probe Tip Potential at Various Distances from Exit Arbitrarily Offset Along the Potential Axis for Clarity. Operating at 770 W, 1333 G and 0.683 mg/s of Argon.

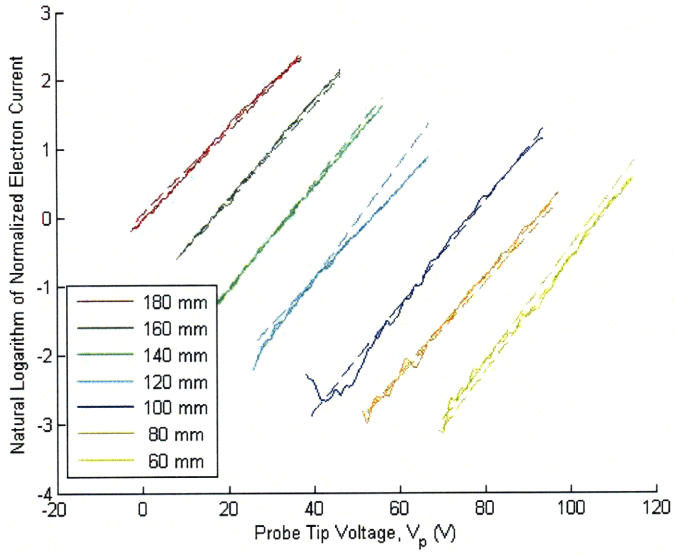

Figure 6-3: Natural Logarithm of Normalized Electron Current vs. Probe Tip Potential at Various Distances from Exit Arbitrarily Offset Along the Potential Axis for Clarity. Operating at 770 W, 1333 G and 0.267 mg/s of Argon.

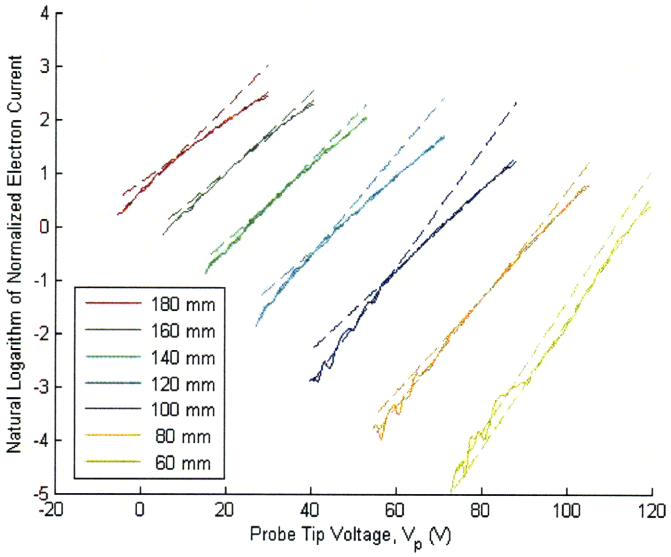

Figure 6-4: Natural Logarithm of Normalized Electron Current vs. Probe Tip Potential at Various Distances from Exit Arbitrarily Offset Along the Potential Axis for Clarity. Operating at 770 W, 2000 G and 0.475 mg/s of Argon.

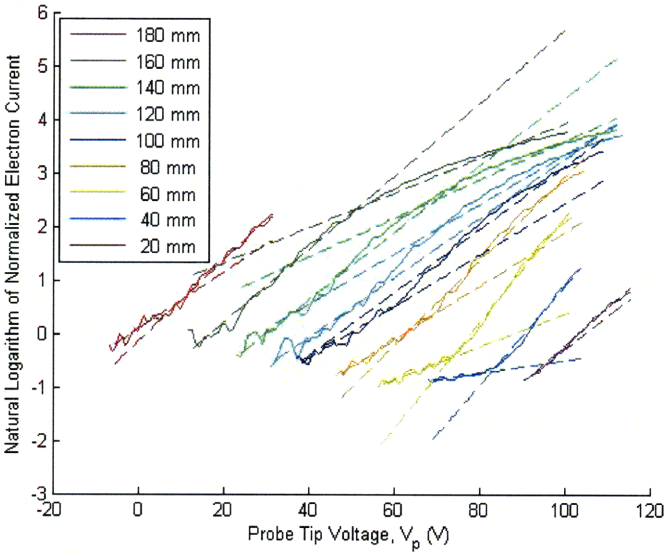

Figure 6-5: Natural Logarithm of Normalized Electron Current vs. Probe Tip Potential at Various Distances from Exit Arbitrarily Offset Along the Potential Axis for Clarity. Operating at 770 W, 667 G and 0.475 mg/s of Argon.

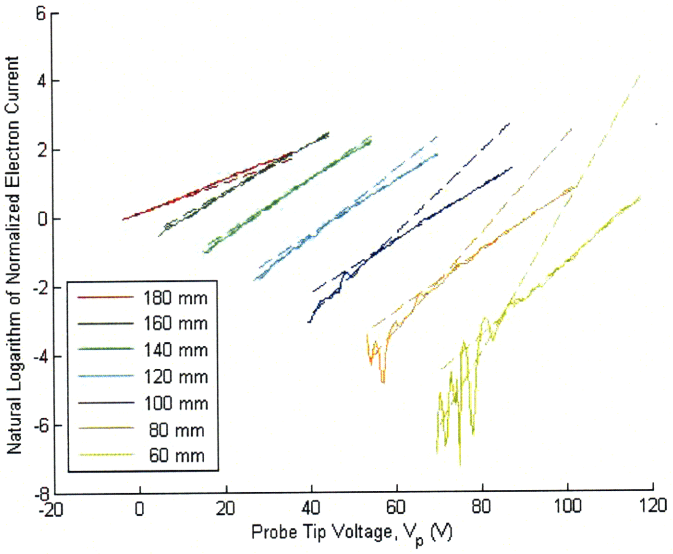

Figure 6-6: Natural Logarithm of Normalized Electron Current vs. Probe Tip Potential at Various Distances from Exit Arbitrarily Offset Along the Potential Axis for Clarity. Operating at 950 W, 1333 G and 0.475 mg/s of Argon.

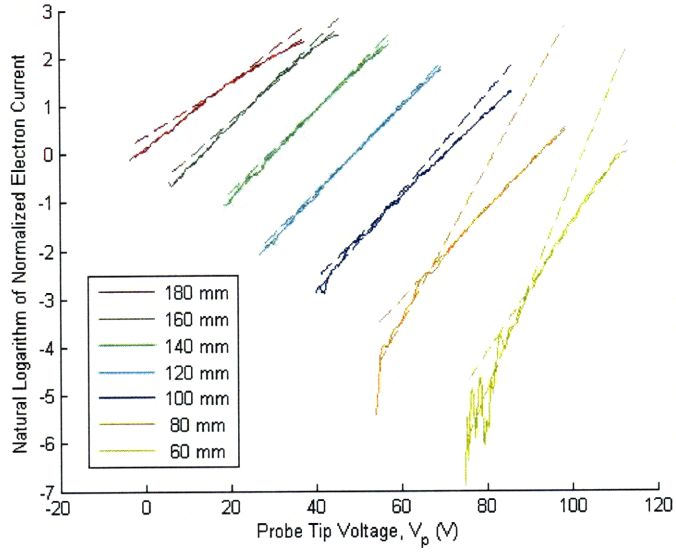

Figure 6-7: Natural Logarithm of Normalized Electron Current vs. Probe Tip Potential at Various Distances from Exit Arbitrarily Offset Along the Potential Axis for Clarity. Operating at 580 W, 1333 G and 0.475 mg/s of Argon.

Chapter 7

Appendix B: Argon I Excited State Population Tables

Wavelength (nm)	A_{qp} (s^{-1})	Quality	n_p (m^{-3})
415.86	1.40E+006	C	2.87E+8
419.07	2.80E+005	C	2.70E+8
419.83	2.57E+006	C	9.10E+7
420.07	9.67E+005	C	4.16E+8
425.94	3.98E+006	C	5.86E+7
427.22	7.97E+005	C	1.61E+8
430.01	3.77E+005	C	3.30E+8
433.36	5.68E+005	C	2.50E+8
451.07	1.18E+006	C	8.80E+7
549.59	1.69E+006	C	1.32E+7
555.87	1.42E+006	C	2.42E+7
560.67	2.20E+006	C	1.62E+7
588.86	1.29E+006	C	1.89E+7
591.21	1.05E+006	C	2.95E+7
603.21	2.46E+006	C	3.39E+7
604.32	1.47E+006	C	2.33E+7
641.63	1.16E+006	C	4.97E+7
667.73	2.36E+005	C	3.09E+8
675.28	1.93E+006	C	8.07E+7
687.13	2.78E+006	C	5.14E+7
693.77	3.08E+006	C	1.88E+7
696.54	6.39E+006	C	3.13E+8

Wavelength (nm)	A_{qp} (s^{-1})	Quality	n_p (m^{-3})
703.03	2.67E+006	C	4.01E+7
706.72	3.80E+006	C	5.68E+8
706.87	2.00E+006	D+	2.85E+7
710.75	4.50E+005	D+	3.81E+7
712.58	6.00E+005	D+	1.79E+7
714.7	6.25E+005	C	4.06E+8
720.7	2.48E+006	C	1.86E+7
727.29	1.83E+006	C	3.29E+8
731.17	1.70E+006	D+	2.12E+7
731.6	9.60E+005	D+	2.45E+7
735.33	9.60E+005	D+	7.18E+7
737.21	1.90E+006	D+	1.05E+8
738.4	8.47E+006	C	5.63E+8
743.54	9.00E+005	D+	4.41E+7
750.39	4.45E+007	C	1.97E+8
751.47	4.02E+007	C	1.39E+8
763.51	2.45E+007	C	4.38E+8
772.38	5.18E+006	C	4.08E+8
772.42	1.17E+007	C	3.14E+8
794.82	1.86E+007	C	2.83E+8
800.62	4.90E+006	C	6.32E+8
801.48	9.28E+006	C	6.13E+8
810.37	2.50E+007	C	3.46E+8
811.53	3.31E+007	C	5.70E+8
826.45	1.53E+007	C	3.11E+8
840.82	2.23E+007	C	5.11E+8
842.46	2.15E+007	C	6.22E+8
852.14	1.39E+007	C	3.84E+8
866.79	2.43E+006	C	4.22E+8

Table 7.1: Measured Population of Upper Level States for Ar I Emission from mHTX Operating at 770 W, 1333 G and 16 sccm. Quality of the Einstein Coefficient is Given with A Signifying Most Accurate as Found in NIST [46]. Length of Plasma Emmission is Taken as 31 cm.

Chapter 8

Appendix C: Argon II Excited State Population Tables

Wavelength (nm)	A_{qp} (s^{-1})	Quality	n_p (m^{-3})
349.15	2.31E+008	B	4.51E+6
355.95	2.88E+008	B	2.88E+6
356.1	4.00E+008	D	1.21E+6
376.53	9.80E+007	D	6.87E+6
404.29	4.06E+007	B	1.59E+7
405.29	6.70E+007	E	2.75E+6
407.2	5.80E+007	B	3.98E+7
410.39	1.20E+008	D	1.59E+7
413.17	8.50E+007	B	9.46E+6
422.82	1.31E+007	A	1.67E+8
423.72	1.12E+007	B	2.06E+7
427.75	8.00E+007	B	1.92E+7
433.12	5.74E+007	A	1.01E+8
437.08	6.60E+007	B	6.64E+7
437.97	1.00E+008	A	5.60E+7
440.1	3.04E+007	B	3.00E+8

Wavelength (nm)	A_{qp} (s^{-1})	Quality	n_p (m^{-3})
443.02	5.69E+007	A	1.06E+8
447.48	2.90E+007	B	8.82E+6
448.18	4.55E+007	B	3.82E+7
454.51	4.71E+007	B	5.74E+7
457.94	8.00E+007	B	3.54E+7
458.99	6.64E+007	A	6.96E+7
465.79	8.92E+007	B	3.63E+7
472.69	5.88E+007	A	6.14E+7
473.59	5.80E+007	A	1.47E+8
476.49	6.40E+007	B	6.54E+7
480.6	7.80E+007	A	1.58E+8
484.78	8.49E+007	B	6.61E+7
487.99	8.23E+007	A	9.29E+7
496.51	3.94E+007	A	5.22E+7
500.93	1.51E+007	B	2.28E+8
501.72	2.07E+007	B	5.42E+7
506.2	2.23E+007	B	1.36E+8
514.18	8.10E+006	A	6.86E+7
514.53	1.06E+007	B	1.13E+8
611.49	2.00E+007	B+	3.64E+7
617.23	2.00E+007	A	2.41E+7
624.31	3.00E+006	B	5.56E+7
648.31	1.06E+007	C+	1.07E+7
663.82	1.37E+007	A	3.26E+7
664.37	1.47E+007	B	1.24E+8
666.64	8.80E+006	B	7.51E+6
668.43	1.07E+007	B+	6.46E+7

Table 8.1: Measured Population of Upper Level States for Ar I Emission from mHTX Operating at 770 W, 1333 G and 16 sccm. Quality of the Einstein Coefficient is Given with A Signifying Most Accurate as Found in NIST [46]. Length of Plasma Emmission is Taken as 31 cm.